



This is to certify that the  
dissertation entitled

INTEGRATION OF A WAVE ROTOR TO AN ULTRA-MICRO  
GAS TURBINE (U $\mu$ GT)

presented by

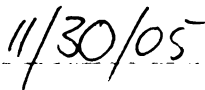
FLORIN IANCU

has been accepted towards fulfillment  
of the requirements for the

Ph.D. degree in MECHANICAL ENGINEERING



Major Professor's Signature



Date



**PLACE IN RETURN BOX** to remove this checkout from your record.  
**TO AVOID FINES** return on or before date due.  
**MAY BE RECALLED** with earlier due date if requested.

DATE DUE	DATE DUE	DATE DUE

**INTEGRATION OF A WAVE ROTOR TO AN  
ULTRA-MICRO GAS TURBINE (U<sub>μ</sub>GT)**

By

Florin Iancu

A DISSERTATION

Submitted to  
Michigan State University  
in partial fulfillment of the requirements  
for the degree of

DOCTOR OF PHILOSOPHY

Department of Mechanical Engineering

2005

## **ABSTRACT**

### **INTEGRATION OF A WAVE ROTOR TO AN ULTRA-MICRO GAS TURBINE ( $U\mu GT$ )**

By

Florin Iancu

Wave rotor technology has shown a significant potential for performance improvement of thermodynamic cycles. The wave rotor is an unsteady flow machine that utilizes shock waves to transfer energy from a high energy fluid to a low energy fluid, increasing both the temperature and the pressure of the low energy fluid. Used initially as a high pressure stage for a gas turbine locomotive engine, the wave rotor was commercialized only as a supercharging device for internal combustion engines, but recently there is a stronger research effort on implementing wave rotors as topping units or pressure gain combustors for gas turbines.

At the same time, Ultra Micro Gas Turbines ( $U\mu GT$ ) are expected to be a next generation of power source for applications from propulsion to power generation, from aerospace industry to electronic industry. Starting in 1995, with the MIT "Micro Gas Turbine" project, the mechanical engineering research world has explored more and more the idea of "Power MEMS". Microfabricated turbomachinery like turbines, compressors, pumps, but also electric generators, heat exchangers, internal combustion engines and rocket engines have been on the focus list of researchers for the past 10 years. The reason is simple: the output power is proportional to the mass flow rate of the working fluid through

the engine, or the cross-sectional area while the mass or volume of the engine is proportional to the cube of the characteristic length, thus the power density tends to increase at small scales ( $Power/Mass=L^{-1}$ ). This is the so-called “cube square law”.

This work investigates the possibilities of incorporating a wave rotor to an U $\mu$ GT and discusses the advantages of wave rotor as topping units for gas turbines, especially at microscale. Based on documented wave rotor efficiencies at larger scale and subsidized by both, a gasdynamic model that includes wall friction, and a CFD model, the wave rotor compression efficiency at microfabrication scale could be estimated at about 70%, which is much higher than the obtained efficiency obtained for centrifugal compressors in a microfabricated gas turbine. This dissertation also proposes several designs of ultra-micro wave rotors, including the novel concept of a radial-flow configuration. It describes a new and simplified design procedure as well as numerical simulations of these wave rotors. Results are obtained using FLUENT, a Computational Fluid Dynamics (CFD) commercial code. The vast information about the unsteady processes occurring during simulation is visualized. Last, two designs for experimental tests have been created, one for a micro shock tube and one for the ultra-micro wave rotor. Theoretical and numerical results encourage the idea that at microscale, compression by shock waves may be more efficient than by conventional centrifugal compressors, thus making the ultra-micro wave rotor (U $\mu$ WR) a feasible idea for enhancing (upgrading) U $\mu$ GT.

*to my father*  
*who has inspired me to pursue a carrier in mechanical engineering*



## **Acknowledgments**

I offer my sincerest appreciation to Dr. Norbert Müller for introducing me to the topic of wave rotors and giving me the opportunity to work on this subject, as well as for his continuous advice and support. His guidance extended to all aspects of my life as a Ph.D. student and was not limited to the research problems. I think of him as a great advisor and a friend.

I also thank Dr. Janusz Piechna for all the support and help he offered during my struggles with research queries. Without some of his great suggestions and ideas, I would not have been able to finish this work.

I was lucky to choose a committee that believed in me and my work and offered continuous and valuable guidance and advice. Dr. Dean Aslam, Dr. André Bénard, Dr. Abraham Engeda and Dr. Luc Fréchette, all contributed significantly to the value of this dissertation.

All my colleagues in the Turbomachinery laboratory have been extremely supportive and helpful. I would like to mention particularly Dr. Pejman Akbari, for helping me tackle the challenging subject of wave rotors, James Bellefeuille and Emmett Dempsey, for helping me untangle some difficult problems. I also appreciate the friendship and help of Nathan Holden and Amir Kharazi. I thank Changgu Lee, Xiangwei Zhu and Yuxing Tang for their help with the experimental part of the dissertation. I am grateful for having such friends

around me for helping me and making my life as a Ph.D. student more enjoyable.

Last but not least, I would like to thank my sister, my parents, and my girlfriend for their encouragement and for tolerating me during the last months of writing this dissertation.

## Preface

The purpose of this research is to combine two development trends in the turbomachinery world (enhancing efficiency by wave rotor topping and increasing power density by miniaturization) by introducing a new concept, the Ultra-Micro Wave Rotor (U $\mu$ WR). This dissertation proposes several designs for integrating the wave rotor to a miniaturized gas turbine as well as shows introductory investigations regarding the feasibility of the ultra-micro wave rotors. The structure of the study is as follows.

*Chapter 1* is a short introduction of MEMS turbomachinery and wave rotors. The history of the micro gas turbine project at MIT (the starting point of present research study), section reviewed by Dr. Stuart Jacobson from the Massachusetts Institute of Technology – Gas Turbine Laboratory. Next, a literature review survey of the wave rotor investigations is presented, starting in 1950 until present, including numerical studies of the gas dynamic process inside the wave rotor channels.

*Chapter 2* describes the initial concepts of ultra-micro wave rotors. Ideas presented here are part of the “Wave Rotors for Ultra-Micro Gas Turbines” permanent patent that was filed in July 2005. The material was partly presented at the Michigan Space Grant Consortium in October 2003.

*Chapter 3* is a theoretical and numerical study of the efficiency of the compression process by shock waves in microchannels. The material was

presented at the 40<sup>th</sup> AIAA Joint Propulsion Conference and Exhibit in July 2004 and was published in Journal of Microfluidics and Nanofluidics in August 2005. This chapter also introduces the optimum design space for the ultra-micro wave rotor, material that will be presented at the PowerMEMS Conference in Tokyo, November 2005.

*Chapter 4* presents preliminary stress investigations of a rotating disc subjected to mechanical and thermal loads. Material presented at the NASA Michigan Space Grant Consortium in October 2004.

*Chapter 5* describes a simple procedure of designing ultra-micro wave rotors. The procedure partially has been presented at the 35<sup>th</sup> AIAA Fluid Dynamic Conference in July 2005.

*Chapter 6* introduces the concept of radial wave rotor as well as the capability of FLUENT to simulate unsteady flow behavior in ultra-micro wave rotors. Two papers covering these subjects have been presented at the 2004 International Mechanical Engineering Conference in November 2004. The radial wave rotor is also the subject of a paper submitted to AIAA Journal that is currently still under review.

*Chapter 7* presents a brief description of the final design of U $\mu$ GT including the integration of the wave rotor.

*Chapter 8* describes the manufacturing procedure for a U $\mu$ WR and a simpler single channel test rig.

*Chapter 9* outlines directions for future work, provides the summary and conclusions.

## TABLE OF CONTENTS

List of Tables.....	xi
List of Figures.....	xii
Key to Symbols and Abbreviations.....	xxiii
Chapter I INTRODUCTION.....	1
I.1    Micro and Ultra-Micro Power Systems.....	1
I.1.1    MIT Micro Gas Turbine Engine Project.....	3
I.1.2    Other Thermo-Mechanical MEMS Devices.....	11
I.2    Wave Rotor Technology and Its Applications.....	19
I.2.1    Wave Rotor Investigations and Products.....	23
I.2.2    Numerical Investigations.....	34
I.3    Wave Rotor Enhanced Ultra Micro Gas Turbines.....	43
Chapter II PROPOSED INITIAL DESIGNS OF A WAVE ROTOR TOPPING AN $U_{\mu}GT$ .....	44
II.1    Axial Wave Rotor Configuration.....	44
II.2    Radial Wave Rotor Configuration.....	47
Chapter III PERFORMANCE CHARACTERISTICS OF ULTRA-MICRO WAVE ROTORS.....	49
III.1    One Dimensional Flow with Friction.....	58
III.2    Flow Across a Moving Shock.....	61
III.3    Numerical Model.....	74
III.4    Comparison of Results.....	79
III.5    Design Space of Wave Rotor Topped Gas Turbines at Microscale.....	81
Chapter IV STRESS INVESTIGATIONS.....	89
IV.1    Materials Used and Properties.....	89
IV.2    Radial and Tangential Stresses with and without Thermal Effects.....	90
IV.2.1    No thermal effects.....	90
IV.2.2    Thermal effects.....	92
IV.2.3    Summary and conclusions.....	93
Chapter V DESIGN OF ULTRA-MICRO WAVE ROTORS ( $U_{\mu}WR$ ).....	96
V.1    Gasdynamics of Compressible Flow.....	97
V.2    Modeling of Unsteady Compressible Flow.....	97
V.2.1    Explicit vs. Implicit.....	97
V.3    Design Methodology.....	100
V.3.1    Through – Flow Solution.....	101
V.3.2    Reverse – Flow Solution.....	117



Chapter VI NUMERICAL SIMULATIONS OF U <sub>μ</sub> WR .....	119
VI.1 Setting up GAMBIT .....	119
VI.2 Setting up FLUENT .....	125
VI.3 Heat Transfer Simulations .....	132
VI.4 Axial U <sub>μ</sub> WR .....	144
VI.5 Radial U <sub>μ</sub> WR .....	156
VI.5.1 Through-Flow Radial Wave Rotor .....	157
VI.5.2 Reverse-Flow Radial Wave Rotor .....	171
VI.5.3 Comparison of Radial Configurations .....	183
Chapter VII FINAL DESIGN OF THE U <sub>μ</sub> WAVE ROTOR.....	191
Chapter VIII EXPERIMENTAL INVESTIGATIONS .....	196
VIII.1 Axial Ultra-Micro Wave Rotor .....	196
VIII.2 Radial Ultra-Micro Wave Rotor .....	200
VIII.2.1 Fabrication of the Radial Wave Rotor Test Rig .....	203
VIII.3 Single Channel Experiment .....	208
VIII.4 End Plates and Ducting .....	216
Chapter IX SUMMARY AND CONCLUSIONS.....	217
IX.1 Summary .....	217
IX.2 Conclusions .....	218
IX.3 Suggestions for Future Work.....	221
IX.3.1 Wave Disc with Curved Channels .....	221
IX.3.2 Optimization of the Thermodynamic Parameters .....	222
IX.3.3 Experimental Testing .....	222
IX.3.4 3D CFD Investigations .....	223
Appendices.....	225
Appendix 1 – Material Properties.....	225
Appendix 2 – U <sub>μ</sub> WR Fabrication Drawings .....	227
Appendix 3 – Microfabrication Details .....	235
References .....	240

## **List of Tables**

Table III.1: Wave rotor compression and expansion efficiency and only compression efficiency. Data found in extant literature .....	52
Table III.2: Entry data for the mathematical model .....	64
Table III.3: Efficiencies of compression process function of shock pressure ratio, entrance temperature and direction of moving shock.....	70
Table IV.1: Radial and tangential stresses in a rotating disc.....	94
Table VI.1: Comparison of numerical results between the three models. ....	137
Table VI.2: Comparison of contour plots between the three models: pressure, temperature, velocity, heat flux and heat transfer coefficient. ....	138
Table VI.3: Thermodynamic parameters of the ultra-micro wave rotor – set one. ....	144
Table VI.4: Thermodynamic parameters of the ultra-micro wave rotor – set two. ....	145
Table VI.5: General thermodynamic parameters of the ultra-micro wave rotor. ....	145
Table VI.6: Details of the full model. ....	145
Table VI.7: Details of the reduced model. ....	146
Table VI.8: Wave rotor operating conditions adjusted for higher pressures in the high-pressure region and lower pressures for the low-pressure region. ....	162
Table VI.9: Wave rotor operating conditions adjusted for higher pressures in the high-pressure region and lower pressures for the low-pressure region. ....	180

## **List of Figures**

Figure I.1: MIT Micro gas turbine generator: cross-section (adapted from (Epstein, Ayón et al. 1997)). .....	4
Figure I.2: Microcompressor and microturbine of the MIT project in the first design stage, (reproduced from (Lin, Ghodssi et al. 1999)). .....	5
Figure I.3: MIT combustor structure (adapted from (Mehra, Zhang et al. 2000)).	6
Figure I.4: MIT Three-wafer structure for microcombustion study (reproduced from (Mehra, Zhang et al. 2000)). .....	7
Figure I.5: MIT H <sub>2</sub> Demo Engine with conduction-cooled turbine constructed from six silicon wafers (adapted from (Epstein, Jacobson et al. 2000)). .....	8
Figure I.6: MIT bearing testing structure (reproduced from (Frechette 2001))....	9
Figure I.7: Single-zone and Dual-zone combustor, part of the MIT micro gas turbine engine (adapted from (Spadaccini, Zhang et al. 2003) – left and (Spadaccini, Mehra et al. 2003) – right). .....	10
Figure I.8: MIT turbocharger test structure (adapted from (Epstein 2003))......	10
Figure I.9: Stanford's micro turbo-compressor with bearing cartridge (reproduced from (Kang, Johnston et al. 2004)). .....	12
Figure I.10: Schematic cross-section of a Rankine steam turbine device (reproduced from (Frechette, Lee et al. 2004)). .....	13
Figure I.11: "Palm top" model of microturbines (reproduced from (Matsuura, Kato et al. 2003)). .....	14
Figure I.12: ONERA alternative to the MIT combustion chamber (reproduced from (Ribaud 2003)). .....	16
Figure I.13: Berkeley's steel piston and combustion chamber for a micro Wankel engine (reproduced from (Walther and Pisano 2003)). .....	17

"Images in this dissertation are presented in color."

Figure I.14: Berkeley's silicon piston chamber for a micro Wankel engine (reproduced from (Walther and Pisano 2003)).	18
Figure I.15: Axial wave rotor drum and end plates.	19
Figure I.16: Comprex® wave rotor drum.	20
Figure I.17: Four-port wave rotor schematic. a) Through-flow configuration; b) Reverse-flow configuration (C – compressor, CC – combustion chamber, WR – wave rotor, T – turbine).	21
Figure I.18: Flow trajectories in a Through-flow axial wave rotor.	22
Figure I.19: Temperature –Entropy Diagram for a gas turbine engine with and without wave rotor topping.	25
Figure I.20: NASA four port wave rotor. Left – the rotor, Right – the test system.	28
Figure I.21: Comparison between the Comprex® supercharged engine (CX) and the turbocharged engine (TC) performances (Heisler 1995).	29
Figure I.22: Comprex® system: 1 - ICE; 2 – HPG port; 3 – HPA port; 4 – LPG port; 5 -LPA port; 6 - rotor; 7 - drive system.	30
Figure I.23: Comprex® rotor and a Mazda 626 supercharging system cut-view.	33
Figure II.1: Conceptual design of U $\mu$ GT – “Classic” design.	45
Figure II.2: Conceptual design of U $\mu$ GT – “Two-layer” design.	46
Figure II.3 Conceptual design of U $\mu$ GT – “External” design.	46
Figure II.4: Conceptual design of U $\mu$ GT – “Radial” design.	47
Figure III.1: Temperature – Entropy diagram for ultra-micro gas turbines, with and without wave rotor.	50
Figure III.2: Efficiency trend of the compression process. Solid line – wave rotor efficiency; Dashed line – compressor efficiency. References: 1 – (Müller and	

Fr chet te 2002), 2 – (Johnston, Kang et al. 2003), 3 – (Okamoto and Nagashima 2003), 4 – (Moritz 1985), 5 – (Akbari and M  ller 2003), 6 – (Mathur 1985), 7 – (Thayer 1985). ..... 54

Figure III.3: 1D model of a microchannel. a) Single channel; b) Shock traveling in direction opposite to the flow; c) Shock traveling in direction of the flow. .... 56

Figure III.4: Pressure and temperature distributions for a single channel model with heat transfer calculations and without. Flow moving from left to right. The results were obtained using FLUENT 6.1. .... 60

Figure III.5: Variation of friction factor with respect to Reynolds number assuming laminar flow: solid line – calculation using classic theory ( $f=64/Re$ ); dotted line – experimental results for microscale flow. .... 64

Figure III.6: Efficiency of compression process as function of position of shock inside the microchannel for different shock strengths, inlet temperature of 1465K, and a shock traveling in direction opposite to the flow. Results obtained using analytical 1D code. .... 66

Figure III.7: Efficiency of compression process function of position of shock inside the microchannel for different shock strengths, inlet temperature of 750K, and a shock traveling in direction opposite to the flow. Results obtained using analytical 1D code. .... 66

Figure III.8: Efficiency of compression process as function of position of shock inside the microchannel for different shock strengths, inlet temperature of 1465 K, and a shock traveling in the direction of the flow. Results obtained using analytical 1D code. .... 67

Figure III.9: Schematic of pressure distribution along the microchannel. a) With shock close to entrance; b) With shock close to exit. Pressure  $p_1$  and ratio  $p_3/p_2$  are the same in both cases. .... 69

Figure III.10: Efficiency of compression process as function of entry temperature for different shock strengths, and for a shock traveling in the direction opposite to the flow. Results obtained using analytical 1D code. .... 72

Figure III.11: Efficiency of compression process function of microchannel length/diameter ratio for different shock strengths, and for a shock traveling in the direction of the flow. .... 73



Figure III.12: Mesh models of a microchannel, inlet and outlet ports.....	76
Figure III.13: Static pressure inside a microchannel at two different time steps. Time =1 is when pressure wave reached the end of the channel. Flow moving from left to right. Results obtained using CFD code FLUENT 6.1. .	77
Figure III.14: Density contours inside a microchannel. Time=1 is when pressure wave reached the end of the channel. Flow moving from left to right. Results have been obtained using CFD code FLUENT 6.1. ....	78
Figure III.15: Wave rotor compression efficiency as function of channel length for constant length/diameter ratio of 6.67. References: 1 – CFD model, 2 – (Zender and Mayer 1984), 3 – (Okamoto and Nagashima 2003), 4 – (Mathur 1985), 5 – (Taussig 1984).....	80
Figure III.16: Optimum points for all performance evaluation parameters function of polytropic compressor efficiency.....	82
Figure III.17: Optimum points for all performance evaluation parameters function of polytropic turbine efficiency. ....	83
Figure III.18: Optimum points for all performance evaluation parameters function of turbine inlet temperature (TIT). ....	84
Figure III.19: Optimum points for specific work for variation of turbine inlet temperature (TIT). ....	85
Figure III.20: Optimum points for specific fuel consumption for variation of turbine inlet temperature (TIT).....	86
Figure III.21: Optimum points for thermal efficiency for variation of turbine inlet temperature (TIT). ....	87
Figure IV.1: Model of a single compressor/turbine disc.....	90
Figure IV.2: Radial and tangential stresses without thermal effects along the radius of the disk (compressor/turbine rotor).....	91
Figure IV.3: Temperature distribution in the three sub-cases: linear, quadratic and logarithmic. ....	93

Figure IV.4: Radial and tangential stresses with thermal effects along the radius of the disk (compressor/turbine rotor).....	94
Figure V.1: Wave pattern for a four port wave rotor (adapted after Resler et al.). .....	100
Figure V.2: NASA wave patterns for the four port wave rotor. Left – through-flow configuration, right – reverse-flow configuration. ....	101
Figure V.3: Wave pattern for a four port through-flow wave rotor.....	102
Figure V.4: Comparison between analytical results and numerical results for an initial port prediction of a through-flow wave rotor (first number is analytically obtained, the second one – numerically). ....	115
Figure V.5: Mass flow rate through the boundaries of a wave rotor channel in through-flow configuration, [kg/s]. ....	116
Figure V.6: Wave pattern for a four port reverse-flow wave rotor.....	117
Figure V.7: Comparison between analytical results and numerical results for an initial port prediction of a reverse-flow wave rotor (first number is analytically obtained, the second one – numerically). ....	118
Figure V.8: Mass flow rate through the boundaries of a wave rotor channel in reverse-flow configuration, [kg/s]. ....	118
Figure VI.1: Axial wave rotor in 2D developed view: a) through-flow configuration; b) reverse-flow configuration (values in $\mu\text{m}$ ).....	120
Figure VI.2: Mesh and interfaces setup for 2D axial wave rotor investigations: a) single port – multiple channel interface, b) single port – multiple channel interface with additional gap, c) multiple port – multiple channel interface with gap. ....	121
Figure VI.3: Radial wave rotor cross-sectional view [dimensions in $\mu\text{m}$ ].....	122
Figure VI.4: Radial wave rotor cross-sectional view – reduced model. ....	123
Figure VI.5: Radial waver rotor in a through flow (TF) configuration: reduced model and zoom in of the mesh.....	124

Figure VI.6: 2D simulation of axial wave rotor: a) pressure distribution, b) temperature distribution. ....	130
Figure VI.7: 2D simulation of axial wave rotor: a) pressure distribution, b) temperature distribution. ....	131
Figure VI.8: Mesh of radial wave rotor with adiabatic walls – zoom-in view.....	134
Figure VI.9: Wall boundary conditions – set up window.....	135
Figure VI.10: Mesh of radial wave rotor with solid walls – zoom-in view. ....	136
Figure VI.11: 3D model of axial wave rotor: a) full model with 12 cycles per revolution, b) reduced model with 1 cycle per revolution. ....	147
Figure VI.12: Pressure distribution for a single channel mode: a) 2 $\mu$ m gap, b) 20 $\mu$ m gap.....	148
Figure VI.13: Pressure distribution for 2D simulation of axial wave rotor: a) TF model, b) RF model, [Pa].....	150
Figure VI.14: Temperature distribution for 2D simulation of axial wave rotor: a) TF model, b) RF model, [K].....	150
Figure VI.15: Low temperature distribution. ....	151
Figure VI.16: Velocity distribution in an axial wave rotor: a) TF – positive direction flow, a) RF – negative direction flow, c) RF – positive direction flow, [m/s].....	152
Figure VI.17: Reynolds number distribution for axial wave rotor. ....	153
Figure VI.18: Flow Mach number distribution for axial wave rotor. ....	154
Figure VI.19: Pressure distribution in the channels of the 3D reduced axial wave rotor model.....	155
Figure VI.20: Through-flow wave disc – porting schematic. ....	157
Figure VI.21: Pressure distribution for the through-flow configuration (first iteration), [Pa]. ....	158

Figure VI.22: Radial velocity distribution for the through-flow configuration (first iteration), [m/s]. .....	159
Figure VI.23: Comparison between initial and updated models. ....	159
Figure VI.24: Through-flow wave disc– static pressure distribution, [Pa], left: full pressure spectrum, right: pressure values form $2.5 \cdot 10^5$ to $3.93 \cdot 10^5$ Pa. .	160
Figure VI.25: Through-flow wave disc – static temperature distribution, [K]. ....	161
Figure VI.26: Through-flow wave disc – static temperature distribution, [K] a) lower port pressures, b) boosted port pressures. ....	162
Figure VI.27: Through-flow wave disc – velocity vectors distribution, [m/s]. ...	163
Figure VI.28: Radial velocity distribution for the through-flow configuration (third iteration), [m/s]. .....	164
Figure VI.29: Comparison of radial and axial flow wave rotors – static temperature distribution, [K]. ....	165
Figure VI.30: Temperature boundary conditions for the external heat transfer investigations, [K]. ....	166
Figure VI.31: Comparison of temperature distributions without and with external heat transfer, [K]. ....	166
Figure VI.32: Comparison of pressure distributions without and with external heat transfer, [Pa]. ....	167
Figure VI.33: Comparison of Nusselt number distributions along the rotor walls without and with external heat transfer. ....	168
Figure VI.34: Schematic of flow entry into a channel. ....	169
Figure VI.35: Reverse-flow wave disc – possible port arrangements. ....	172
Figure VI.36: Reverse-flow wave disc – static pressure distribution, [Pa]. ....	173
Figure VI.37: Reverse-flow wave disc – static temperature distribution, [K]. ..	173

Figure VI.38: Reverse-flow wave disc – density distribution, [kg/m <sup>3</sup> ].	174
Figure VI.39 Reverse-flow wave disc – radial velocity distribution, [m/s].	175
Figure VI.40: Reverse-flow wave disc with air ports on inner diameter – temperature distribution, [K]: a) results after first cycle, b) results after several cycles.	176
Figure VI.41: Reverse-flow wave disc with gas ports on inner diameter – temperature distribution, [K]: a) results after first cycle, b) results after several cycles.	177
Figure VI.42: Reverse-flow wave disc – static pressure distribution: left – air ports located on inner diameter, right – gas ports located on inner diameter, [Pa].	178
Figure VI.43: Reverse-flow wave disc – static pressure distribution: left – air ports located on inner diameter, right – gas ports located on inner diameter, [Pa].	178
Figure VI.44: Reverse-flow wave disc – Mach number distribution: left – air ports located on inner diameter, right – gas ports located on inner diameter.	179
Figure VI.45: Reverse-flow wave disc – Reynolds number distribution: left – air ports located on inner diameter, right – gas ports located on inner diameter.	180
Figure VI.46: Static pressure distribution for the RFAI models, [Pa].	181
Figure VI.47: Static temperature distribution for the RFAI models, [K].	182
Figure VI.48: Mach number distribution for the RFAI models.	183
Figure VI.49: Pressure diagram for inner and outer circumference for the three configurations, [Pa].	184
Figure VI.50: Pressure diagram for inner and outer circumference displayed for one cycle only, [Pa].	185



Figure VI.51: Pressure diagram for high and low pressure gas for the three configurations, [Pa]. .....	186
Figure VI.52: Pressure diagram for high and low pressure air for the three configurations, [Pa]. .....	187
Figure VI.53: Temperature diagram for inner and outer circumference displayed for one cycle only, [K]. .....	188
Figure VI.54: Temperature diagram for high and low pressure gas for the three configurations, [K]. .....	189
Figure VI.55: Temperature diagram for high and low pressure air, [K]. .....	190
Figure VI.56: Mach number diagram for inner and outer circumference. ....	190
Figure VII.1: Full assembly of the wave rotor topped ultra-micro gas turbine. .	192
Figure VII.2: Cross-sectional views of the U $\mu$ GT unit. ....	193
Figure VII.3: Partial assembly views of the U $\mu$ GT, showing different components. ....	194
Figure VII.4: Top and bottom view of the U $\mu$ GT, showing also flow paths. ....	195
Figure VIII.1: Axial ultra-micro wave rotor. ....	196
Figure VIII.2: Axial ultra-micro wave rotor: left – top view; right – cross-section. ....	197
Figure VIII.3: Schematic process flow for microfabrication of axial wave rotor.	198
Figure VIII.4: Positive mask used in step 5 of axial wave rotor fabrication. ....	199
Figure VIII.5: Radial ultra-micro wave rotor: a) 3D view; b) side view; c) top view. ....	200
Figure VIII.6: Radial wave rotor: left – A-A cross-section (from Fig.5); right – B-B cross-section. ....	201

Figure VIII.7: Process flow for radial ultra-micro wave rotor fabrication. ....	202
Figure VIII.8: Radial wave rotor with rounded cross-sectional channels. ....	202
Figure VIII.9: Positive mask used in step 5 of radial wave rotor fabrication. ....	203
Figure VIII.10: Wafers used for rotor fabrication. ....	204
Figure VIII.11: Wafers used for ports and plenums fabrication. ....	205
Figure VIII.12: Cut-view of the rotor wafers' assembly. ....	206
Figure VIII.13: Cut-view of the ports' and plenums' wafer assembly. ....	206
Figure VIII.14: Full wave rotor assembly. ....	207
Figure VIII.15: Alignment marks – example. ....	207
Figure VIII.16: Process flow for microfabrication of single channel test rig. ....	208
Figure VIII.17: Masks used for etching single channels. ....	209
Figure VIII.18: Silicon microchannels: a) array of silicon dies; b) single die – front view; c) single die- back view. ....	210
Figure VIII.19: Different size channels visualized with optical microscope. ....	211
Figure VIII.20: Light reflection interference when visualizing silicon channels with optical microscope. ....	212
Figure VIII.21: Different size channels visualized with SEM: a) 90 $\mu$ m and 180 $\mu$ m wide channels; b) 360 $\mu$ m and 720 $\mu$ m wide channels. ....	212
Figure VIII.22: Details of microfabrication of the silicon channel. ....	213
Figure VIII.23: Bond between silicon and glass wafers. ....	214
Figure VIII.24: Mounting bracket for the silicon chip: a) assembly; b) middle aluminum plate; c) bottom plate with access holes. ....	215

Figure IX.1: Wave disc with curved channels – ports schematic. ....	221
Figure IX.2: Wave disc with curved channels – 3D rendering. ....	222
Figure IX.3: Simplified ultra-micro wave rotor test rig. ....	223
Figure IX.4: Quasi 3D mesh model for 3D CFD investigations. ....	224
Figure A.5: Technical drawing of the ultra-micro wave rotor in a through-flow configuration.....	227
Figure A.6: Technical drawing of the ultra-micro wave rotor in a reverse-flow configuration with air ports placed on the inside region. ....	227
Figure A.7: Mask used for first etch step of rotor wafer 1. ....	230
Figure A.8: Mask used for second etch step of rotor wafer 1.....	230
Figure A.9: Mask used for first etch step of rotor wafer 2. ....	231
Figure A.10: Mask used for second etch step of rotor wafer 2.....	231
Figure A.11: Mask used for first etch step of plenum wafer 1.....	232
Figure A.12: Mask used for second etch step of plenum wafer 1. ....	232
Figure A.13: Mask used for first etch step of plenum wafer 2.....	233
Figure A.14: Mask used for second etch step of plenum wafer 2. ....	233
Figure A.15: Mask used for third etch step of plenum wafer 2. ....	234
Figure A.16: MA6/BA6 Mask Aligner - mask tray. ....	236
Figure A.17: Wafer holder for etching. ....	237
Figure A.18: Wafer dicing saw. ....	239

## Key to Symbols and Abbreviations

$a$	speed of sound [m/s]
$\alpha$	coefficient of thermal expansion [1/K]
$A$	cross-sectional area [m <sup>2</sup> ]
$C_p$	specific heat [J/kg·K]
$D$	diameter [m]
$D_H$	hydraulic diameter [m]
$\delta$	boundary layer thickness [m]
$\delta_T$	thermal boundary layer thickness [m]
$e$	internal energy [J]
$E$	expansion wave; elastic modulus [GPa]
$f$	friction factor
$f_x$	body forces [N]
$g$	gravitational acceleration [m/s <sup>2</sup> ]
$\gamma$	specific heat ratio; specific weight
$h$	coefficient of convective heat transfer [W/m <sup>2</sup> ·K]
$\Delta p$	pressure drop [Pa]
$\eta_p$	polytropic efficiency [%]
$\eta$	isentropic efficiency [%]
$L$	channel length [m]
$L^*$	distance to sonic conditions [m]
$L_E$	velocity entry length [m]
$L_T$	thermal entry length [m]
$\lambda$	mean free path [m]
$\Lambda$	characteristic length [m]
$k$	entrance loss coefficient; coefficient of thermal conductivity [W/m·K]
$Kn$	Knudsen number
$M$	Mach number

$\mu$	kinematic viscosity [St]
$Nu$	Nusselt number
$\nu$	Poisson's ration
$\Pi$	pressure ratio
$p$	pressure [Pa]
$Pr$	Prandtl number
$PR_w$	wave rotor compression ratio
$\dot{q}$	heat flux [W/m <sup>2</sup> ]
$r$	radius [m]
$R$	specific gas constant [J/kg·K], compressor pressure ratio
$\rho$	density [kg/m <sup>3</sup> ]
$Re$	Reynolds number
$S$	shock wave
$St$	Stanton number
$\sigma$	stress [Pa]
$t$	time [s]
$T$	temperature [K]
$u$	flow velocity [m/s]
$u_p$	induced flow velocity behind shock wave [m/s]
$v$	tangential velocity [m/s]
$w$	shock wave velocity [m/s], specific work [kJ/kg]
$x$	coordinate along the x-axis (usually along the channel)

### Subscripts

$0$	inlet port
$1$	entry of the microchannel
$2$	location before shock (relative to fixed reference frame)
$3$	location after shock (relative to fixed reference frame)
$4$	exit of the microchannel

## Chapter I

### INTRODUCTION

#### I.1 Micro and Ultra-Micro Power Systems

The second half of the 20<sup>th</sup> century was dominated by a boom in the electronic industry and the semiconductor manufacturing technology associated with it. As this technology of creating smaller and smaller devices evolved, more and more complicated assemblies were created and also mechanical parts were included. These assemblies grouped together generated systems leading to the concept of *Micro Electrical Mechanical Systems (MEMS)*, which appeared at the end of 20<sup>th</sup> century. Early work includes sensors and actuators; followed by valves; and recently complete fluid microsystems.

As the systems become more complex, the need for a more efficient power source as an alternative to batteries emerged. Scientists have started to investigate the possibility of reducing the scale of high efficiency power sources that are currently used (internal combustion engines, gas turbines, steam turbines) down to millimeter and micrometer dimensions. A new research field was born: *Power MEMS* (Epstein, Ayón et al. 1997).

The most investigated power sources are gas turbines. Since there is a discrepancy between what researchers call a microturbine, which are gas turbines with structures of micrometer size, and what industry calls microturbine, the gas turbines in the

range of about 10-100kW. This work refers to first one - the microscale gas turbines - as *Ultra-Micro Gas Turbine (U $\mu$ GT)*.

Due to their high power density, ultra-micro gas turbines (U $\mu$ GT) are appropriate solutions for powering unmanned air-vehicles (UAV) and the electronically equipment associated with them (sensors, probes, or cameras). A typical size of a microfabricated (on-the-chip) U $\mu$ GT is 10mm $\times$ 10mm $\times$ 3mm with a power output between 1 and 100W. These microfabricated gas turbines are also suitable for high-density, *distributed* power generation onboard larger aircrafts. Applied in batches they yield high redundancy and reduce the vulnerability of the system. The power density of turbomachinery increases while their size decreases because the output power is proportional to the mass flow rate of working fluid through the engine. While this scales with the through-flow area, which is proportional to the square of the characteristic length, the mass or volume of the engine is proportional to the cube of the characteristic length. Thus, the power density, which is Power/Volume will be proportional to the inverse of the characteristic length. This is the so-called "cube square law", which suggests that power density of turbomachinery will increase while the dimensions decrease (Frechette 2000).

Today, the Power MEMS community comprises a few research groups, and some of these and their results are going to be presented in this sub-chapter: Massachusetts Institute of Technology, Stanford University, University of California at Berkeley, Georgia Institute of Technology, Washington State University, Michigan State

University in United States, Sherbrooke University in Canada, ONERA in France, Warsaw University of Technology in Poland, The University of Tokyo, Tokyo Institute of Technology and Kanagawa Institute of Technology in Japan, Katholieke Universiteit Leuven in Belgium, Birmingham University in United Kingdom, and Korea Advanced Institute of Science and Technology in Korea. An “informal survey” was presented by Epstein and Jacobson in 2003 and summarizes some of the results obtained at that time in Power MEMS (Jacobson and Epstein 2003).

The first publication appeared about the Micro Gas Turbine Engine project at MIT (Epstein, Ayón et al. 1997). It appears that there so far the most extensive work has been performed in investigating Power MEMS. Their latest design (Jacobson, Das et al. 2004) provides the basis of the research done and presented in this thesis.

#### I.1.1 MIT Micro Gas Turbine Engine Project

In 1995 MIT initiated a project of miniaturizing gas turbines with the scope of using them for power generation and small aerial vehicle propulsion. It was the beginning of the *Micro Gas Turbine Engine Project*.

In 1997, the first information about the project is released. The baseline engine design consisted of a supersonic radial compressor and turbine connected by a hollow shaft (Figure I.1).



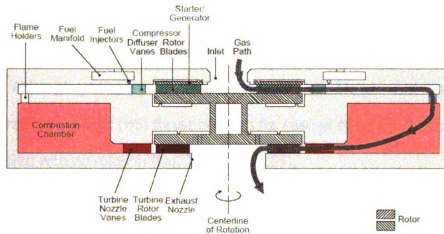


Figure I.1: MIT Micro gas turbine generator: cross-section (adapted from (Epstein, Ayón et al. 1997)).

The combustor wraps the compressor-turbine unit as an annular ring. The material used initially for fabrication was silicon. Extensive information for silicon microfabrication was available; but part of the research process was to develop new techniques for microfabrication, which allows for higher precision and better manufacturing capabilities. Later, silicon carbide was incorporated to strengthen the silicon substrate. This was done by the deposition of a SiC layer into 50  $\mu\text{m}$  deep channels etched into a 100  $\mu\text{m}$  thick Si wafer. At the same time silicon carbide, which can withstand temperature up to 1900K (Keith 2004) without cooling or a more advanced design having cooled Si as material for compressor/turbine unit was introduced. Gas bearings were selected for the rotating parts: journal bearings support the radial load and thrust bearings the axial one. A motor/generator starts the gas turbine and produces electrical power. It has been assumed to produce 20-40W (Epstein, Ayón et al. 1997; Epstein, Senturia et al. 1997).

Initially, journal bearings were designed to be hydrodynamic (HD). But they proved to be unstable at low speeds, creating problems at start-up (Jacobson 1998). Although they proved to be efficient, the design was modified to incorporate hydrostatic (HS) thrust bearings for ease of operation, since they are stable even with no rotation (Liu, Teo et al. 2005).

The first Microturbine/Bearing Rig fabricated was presented, including the manufacturing process and initial test results, in the paper presented at the 13<sup>th</sup> IEEE International MEMS Conference (Lin, Ghodssi et al. 1999). Initial tests focused on the stability of the rotor and the potential of the hydrostatic bearings. Results were shown after continuous operation up to 60,000rpm, but it was noticed that the bearings were not constructed in the design parameters. The compressor and turbine are displayed in Figure I.2.

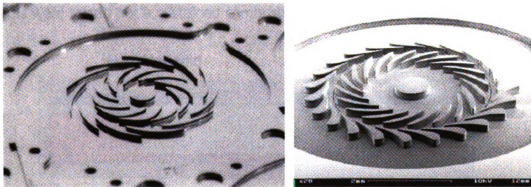


Figure I.2: Microcompressor and microturbine of the MIT project in the first design stage, (reproduced from (Lin, Ghodssi et al. 1999)).

The microscale combustion process was studied in more detailed by creating a three-wafer static structure that incorporated an annular combustion chamber. Figure I.3 is a schematic of the structure, while Figure I.4 shows an SEM

photography of the structure's cross-section. Preliminary hydrogen-air combustion tests proved the resistance of the system to temperatures up to 1725K without degradation after continuous operation for 6 hours (Mehra, Waitz et al. 1999). The structure was further advanced with compressor and turbine airfoils, flame holders, and a recirculation jacket, all designed in a six-wafer structure. The jacket aimed to recover the lost energy of the combustion chamber to pre-heat the incoming reactants, while allowing the compressor discharge air to cool the hot walls of the chamber. The flame holders were incorporated for increasing combustion stability by creating some reservoirs for hot products to serve as igniters for fresh reactants (Mehra, Zhang et al. 2000). The tests showed a combustion efficiency ranging from 90–98% for a fuel-air equivalence ratio of 0.6–0.4 and a mass flow rate of 0.04–0.06g/s. Hydrocarbon fuels were tested but a sustained combustion reaction was not obtained.

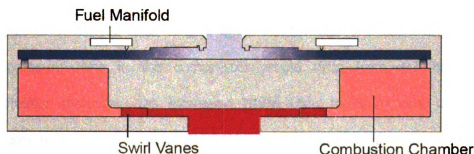


Figure I.3: MIT combustor structure (adapted from (Mehra, Zhang et al. 2000)).

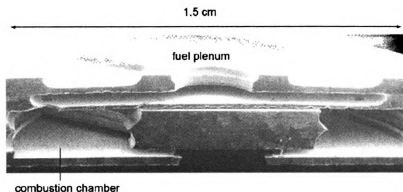


Figure I.4: MIT Three-wafer structure for microcombustion study (reproduced from (Mehra, Zhang et al. 2000)).

A new design for the micro gas turbine engine was proposed in 2000, called the *H<sub>2</sub> Demo Engine*. (Epstein, Jacobson et al. 2000). The main change was to structurally connect the compressor directly to the turbine back to back without a shaft connecting them. The turbine is then cooled by conduction to the compressor, thus keeping the overall temperature lower than the maximum admissible temperature of the material. This way, the air coming to the compressor would be used to cool down the turbine. The disadvantage is that the pressure ratio in the compressor would drop from 4:1 to 2:1. The compressor diameter was increased from 4mm to 8mm, and the turbine diameter to 6 mm. The airfoils were heightened from 200 $\mu$ m to 400 $\mu$ m; thus, the mass flow rate increased to 0.36g/s. The cross-sectional diagram of the H<sub>2</sub> Demo Engine is presented in Figure I.5.

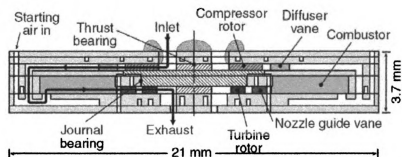


Figure I.5: MIT H<sub>2</sub> Demo Engine with conduction-cooled turbine constructed from six silicon wafers (adapted from (Epstein, Jacobson et al. 2000)).

More work was done on enhancing the gas bearing system. Since the project's main part is a rotating disk, the problem of free rotation is crucial. A microsystem (Figure I.6) was developed to study the performance of a turbine and compressor unit supported by gas lubricated bearings (Frechette, Jacobson et al. 2000; Frechette, Jacobson et al. 2005; Liu, Teo et al. 2005). The device was tested to rotational speeds above 1 million RPM, which would convert into a tip speed of 300m/s, similar to the ones obtained in conventional scale turbomachinery.

The igniters for the combustion chamber were investigated next (Zhang, Mehra et al. 2002; Zhang, Mehra et al. 2003). The MIT research group concluded that thin-film polysilicon resistive elements should be used as igniters for the microengine combustor, showing that it is possible to locally heat an isolated element up to 600K and ignite the hydrogen-air mixture used as combustible.

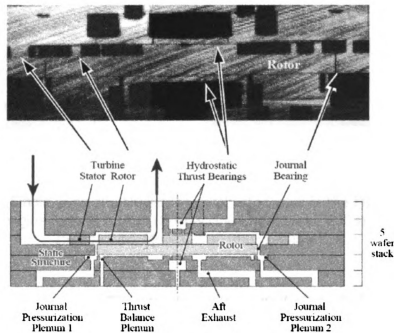


Figure I.6: MIT bearing testing structure (reproduced from (Frechette 2001)).

The research efforts were once again focused on the combustion system of the micro gas turbine engine. An intermediate step in developing the final concept of combustion chamber was to fit platinum-coated nickel foam inserts and use them as on initial catalytic combustor test-bed. Thus hydrocarbon fuels could be ignited and burned with a sustained rate at efficiencies of about 40% (Spadaccini, Zhang et al. 2003). A new approach was taken for the combustion system: to have a dual-zone combustor, basically delivering fuel-air mixture to the combustion chamber by two paths (Spadaccini, Lee et al. 2002; Spadaccini, Mehra et al. 2003). This allowed hydrogen fuel to burn with efficiencies above 90% and hydrocarbon fuels at 60%. The difference between the older design and the new one is illustrated in Figure I.7.

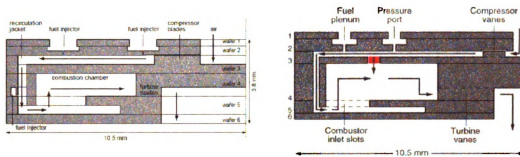


Figure I.7: Single-zone and Dual-zone combustor, part of the MIT micro gas turbine engine (adapted from (Spadaccini, Zhang et al. 2003) – left and (Spadaccini, Mehra et al. 2003) – right).

In 2003 the design was modified by reintroducing the shaft between the compressor and the turbine. This was possible by strengthening the turbine disc with silicon carbide (Epstein 2003). The new generation turbocharger (shown in Figure I.8) was tested to rotational speeds of 480,000RPM. The turbocharger had a compressor and turbine and was basically the H<sub>2</sub> Demo Engine with the compressor exhaust disconnected from the turbine inlet. The pressure ratio measured across the compressor was 1.21 (Jacobson, Das et al. 2004).

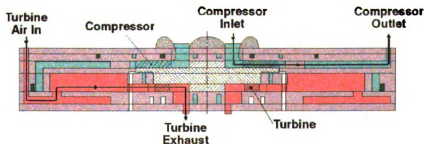


Figure I.8: MIT turbocharger test structure (adapted from (Epstein 2003)).

Although many of the initial problems and challenges were overcome in the past 10 years and the micro gas turbine engine project is closer to reality than in 1995, a problem is still to be solved: the efficiency of the overall process is low, making the system unfeasible. This is due to physical effects that have more influence on the process at microscale compared to regular scale fluid dynamics: wall shear stresses and friction, viscous forces, usable strength of materials, and chemical reaction times. Also, the manufacturing processes are still constraining the design to an approximate 2D layered design, which is restricting the flow and affecting the mass flow rate.

The low efficiency (below 50%) of the turbo compression system (Müller and Fréchette 2002) has been isolated as a major problem for the feasible design space of the project. In this thesis, a solution is proposed which will increase the efficiency of the compressor and/or increase the pressure boost of fresh air delivered to the combustion chamber, thus increasing the efficiency of combustion.

### I.1.2 Other Thermo-Mechanical MEMS Devices

#### *I.1.2.1 Stanford University*

The Rapid Prototyping Laboratory at Stanford University built a micro compressor impeller and tested it at rotational speeds up to 420,000RPM. The impeller was molded from silicon nitride using a Mold Shape Deposition Manufacturing (SDM)



process. In the same time a numerical model was developed using an in-house made Computational Fluid Dynamics (CFD) code. The results from experiments were compared to the CFD results, and good matching has been obtained. The adiabatic efficiency of the compressor was calculated as 70% at 400,000RPM with numerical and experimental values, and predicted 65% at 800,000RPM which would convert to 500m/s tangential tip velocity (Kang 2001; Johnston, Kang et al. 2003; Kang, Johnston et al. 2004). Figure I.9 presents the micro compressor-turbine unit.

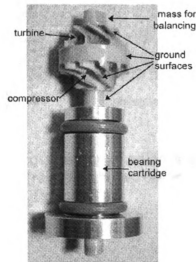


Figure I.9: Stanford's micro turbo-compressor with bearing cartridge (reproduced from (Kang, Johnston et al. 2004)).

#### *1.1.2.2 Sherbrooke University*

Efforts for developing a Rankine Cycle Microturbine are underway in Canada. The research group led by Dr. Luc Fr  chette proposes the concept of a miniaturized complete micro Rankine power source, consisting of a heat source (burner with fuel tank or waste heat), a cooling mechanism (cooling fan or other heat removal

approach), the MEMS-based micro Rankine device and power electronics. The Rankine device itself consists of a steam-driven turbine that entrains a liquid pump and an integrated generator, along with a compact evaporator and a condenser (Frechette, Lee et al. 2004). A schematic cross-section of this device is shown in Figure I.10.

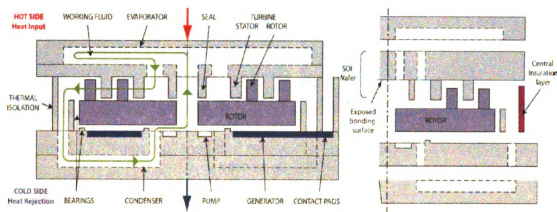


Figure I.10: Schematic cross-section of a Rankine steam turbine device (reproduced from (Frechette, Lee et al. 2004)).

### *1.1.2.3 University of Tokyo*

The University of Tokyo has been investigating a device similar to the MIT one, having initially built a “palm top” model with an outer diameter of 180mm and length of 335mm, which will generate 2-3kW at 235,000RPM. Also a microscale model is proposed, the “finger top” gas turbine with a diameter of 23mm and length of 32mm producing tens of Watts at 1,170,000RPM. The predicted thermal efficiency of the micro gas turbine would be 7% for a simple cycle and 15% in a regenerative cycle (Matsuo, Yoshiki et al. 2003). Several other models

of 2D and 3D radial microturbines were designed and fabricated, efficiencies of the 2D ones being reported as 15% lower than the ones of 3D for the same generic dimensions (Matsuura, Kato et al. 2003).

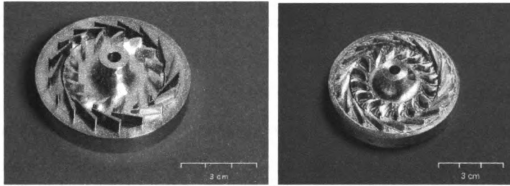


Figure I.11: "Palm top" model of microturbines (reproduced from (Matsuura, Kato et al. 2003)).

#### *I.1.2.4 Tokyo Institute of Technology*

The design of a recuperator is proposed by the Tokyo Institute of Technology for microturbines similar to the ones designed at the University of Tokyo: one with an output of nearly 3kW and another with 15W output. In the case of 3kW class turbine an offset-strip-fin recuperator was employed. For the smaller size turbine a microchannel recuperator was designed. Although the effectiveness of microchannel recuperator is larger than that of offset-strip-fin recuperator, it suffers from a deterioration of effectiveness due to the axial heat conduction of the wall. The reported thermal efficiencies of the cycles topped at 35% (Nagasaki, Tokue et al. 2003).

#### *I.1.2.5 The French Aeronautics and Space Research Center (ONERA)*

Ribaud and his team at ONERA have extensively investigated the heat transfer phenomena in a ultra-micro gas turbine (Dessornes, Dumand et al. 2003; Ribaud 2003). Based on theoretical and numerical models developed, several conclusions were stated: a non adiabatic operation of the turbomachines leads to a strong penalty in performances, doubling the size of the microturbine allows the recovery of a suitable power, so is heat insulation. The use of a low conductivity material for the stator would improve performances by a large amount. The external radiation heat losses are estimated to 10% of the nominal power for the 20mm diameter microturbine. A thermal shield of 2mm thickness is a good way to enhance the performances and is certainly a necessity for integration. Starting from the MIT micro gas turbine engine, an alternative combustion chamber was designed (Figure I.12).

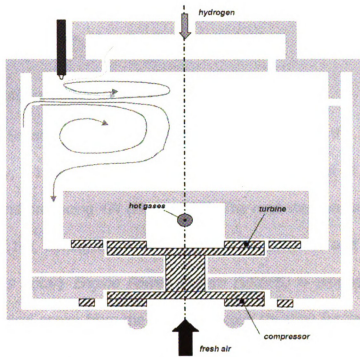


Figure I.12: ONERA alternative to the MIT combustion chamber (reproduced from (Ribaud 2003)).

#### *I.1.2.6 Catholic University of Leuven*

Peirs, Reynaerts, and Verplaetsen have developed a single-stage axial microturbine generator with a rotor diameter of 10 mm (Peirs, Reynaerts et al. 2004; Peirs, Verplaetsen et al. 2004). This turbine is a first step in the development of a microgenerator that produces electrical energy from fuel. The turbine, made of stainless steel, was manufactured using die-sinking electro-discharge machining (EDM). The turbomachinery is connected by a shaft that is supported by ball bearings. It has been tested to speeds up to 160,000rpm and generates a maximum mechanical power of 28W with an efficiency of 18%.

When coupled to a small generator, it generates 16W of electrical power, which corresponds to 10.5% efficiency for the total system.

#### *1.1.2.7 University of California at Berkeley*

The Berkeley Sensor and Actuator Center has developed the micro *Wankel Engine*. Initially, a 12.9mm rotor engine was manufactured out of steel, spinning at 9,300RPM and producing 4W (Figure I.13). The next step was a 2.4mm silicon rotor (Figure I.14), aiming to produce up to 0.1W (Walther and Pisano 2003). Also, a *Viscous Rotary Engine Power System (VREPS)* is proposed, which will extract mechanical power from the surface viscous shearing forces developed by a pressure driven flow present between a rotating disk or annulus and a stationary housing (Cauley, Rosario-Rosario et al. 2004).

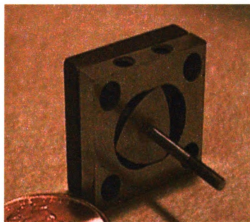


Figure I.13: Berkeley's steel piston and combustion chamber for a micro Wankel engine (reproduced from (Walther and Pisano 2003)).

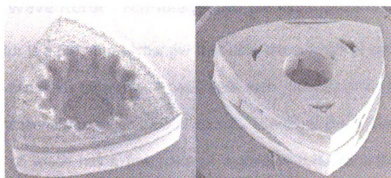


Figure I.14: Berkeley's silicon piston chamber for a micro Wankel engine (reproduced from (Walther and Pisano 2003)).

## I.2 Wave Rotor Technology and Its Applications

The wave rotor is a pressure exchanger that uses the concept of direct pressure transfer between fluids by waves. A basic wave rotor consists of a rotating drum with straight channels arranged around its axis. The drum lies between two end plates, each of which has a few ports or manifolds controlling the fluid flow through the channels. Figure I.15 presents a schematic axial wave rotor drum and its end plates.

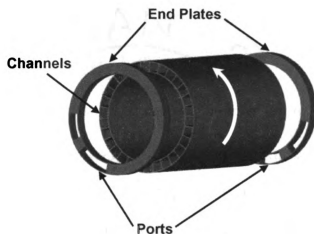


Figure I.15: Axial wave rotor drum and end plates.

Figure I.16 presents a wave rotor drum from a Comprex®. The number of ports and their positions vary for different applications. Through rotation, the channel ends are periodically exposed to the ports located on the stationary end plates initiating compression and expansion waves within the wave rotor channels. Therefore, unlike a steady-flow turbomachine, which either compresses or



expands the gas, both compression and expansion are accomplished within a single component.

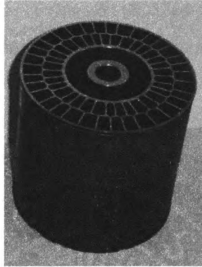


Figure I.16: Comrex® wave rotor drum.

The gap between the end plates and the channel assembly has to be relatively small to minimize leakage losses. This may be ensured by a passive or active gap control or by contacting surfaces that are made of an appropriate sealing material. While in most applications the channel assembly rotates and the end plates are stationary, the opposite configuration has been suggested in which the channels are stationary and the end plates with port openings rotate, ensuring the same flow control mechanism. Such a configuration has more than one rotating part and usually doubles the number of interfaces that need to be sealed between rotating and stationary parts. However, it may be preferred for laboratory investigations because it easily enables flow measurement in the stationary channels where the important dynamic interactions take place.

Two four-port wave rotor schematics for gas turbine topping are presented in Figure I.17: In a through flow (TF) configuration all flows travel in the same direction. In a reverse flow configuration (RF), each flow (gas or air) exits the same side at which it enters. For the TF wave rotor, the channels of the wave rotor are initially filled with air coming from the compressor ("fresh air"), through the low pressure air port (LPA/1). When they come in contact with the gases coming from the combustion chamber, which have high pressure and temperature (HPG/3), a shock wave is formed, which compresses the fresh air. This high pressure air (HPA/2) is then evacuated to the combustion chamber, while the remaining gases, which now have a lower pressure than at the entrance are scavenged towards the turbine. They are called pre-expanded gases or low pressure gases (LPG/4).

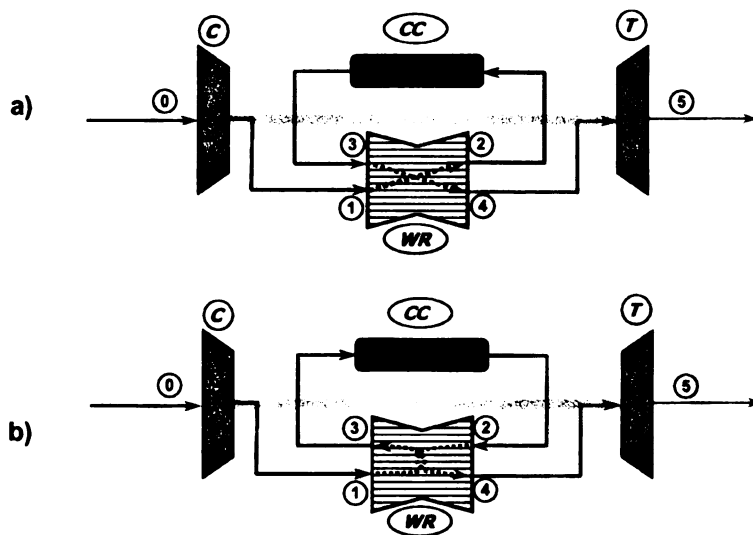


Figure I.17: Four-port wave rotor schematic. a) Through-flow configuration; b) Reverse-flow configuration (C – compressor, CC – combustion chamber, WR – wave rotor, T – turbine).

The active components of an axial wave rotor in a through-flow configuration as well as the trajectories of the flow are displayed in Figure I.18.

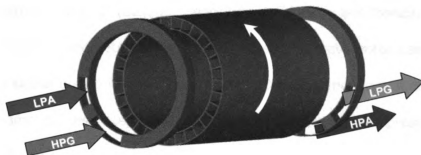


Figure I.18: Flow trajectories in a Through-flow axial wave rotor.

The rotating parts may be gear or belt driven or preferably direct driven by an electric motor. The power required to keep them at correctly designed speed is negligible. It only needs to overcome rotor windage and friction in the bearings and contact sealing if used. Alternatively, rotors can be made self-driving. This configuration, known as the “free-running rotor”, can drive itself by using the momentum of the flow to rotate the rotor.

The periodic exposure of the channels to both fluids between which the pressure is exchanged, assures a channel wall temperature between the temperatures of both fluids, which gives the wave rotor an inherently self-cooling feature. Further, the velocity of the working fluid in the channels is about one-third of values within turbomachines. Therefore, the rotor channels are less prone to erosion damage than the blades of turbomachines and viscous losses are less severe.

From the manufacturing point of view, adding a wave rotor is much easier at microscale than at macroscale. The fabrication processes at microscale are mainly two-dimensional (etching, deposition, oxidation, and bonding), heavily constraining the geometry of the components. The wave rotor can easily be etched in silicon due to its common extruded 2D shape; moreover it can be done in the same process step with creating the turbine or compressor blades. Additionally, in a regenerative way the wave rotor allows to harvest some of the heat conducted away from the combustor through the structure, which is a severe problem for microfabricated gas turbines and also reduces the efficiency of the spool compressor.

#### I.2.1 Wave Rotor Investigations and Products

A very useful and well documented review of the wave rotor technology is offered by Akbari, Nalim, and Müller (Akbari, Nalim et al. 2004). The most important applications and research results in the field are presented next.

As a combined expansion and compression device, the wave rotor can be used as a supercharging device for IC engines, a topping component for gas turbines, or in refrigeration cycles. In advanced configurations, the high energy fluid may be generated by combustion occurring internally in the wave rotor channels allowing extremely short residence times at high temperature, hence potentially reducing emissions. A condensing wave rotor may be viewed as a similarly advanced configuration that enhances the performance of refrigeration cycles.

Recently, wave rotor technology has been envisioned to enhance the performance of ultra-micro gas turbines manufactured using today's and future microfabrication technologies (Okamoto, Nagashima et al. 2003; Iancu, Akbari et al. 2004).

### *Gas Turbine Applications*

For gas turbine applications, in a conventional arrangement, a wave rotor is embedded between the compressor and turbine "parallel" to the combustion chamber. Figure I.17 illustrates how a four-port wave rotor is used to top a gas turbine cycle. In the wave rotor channels, the hot gas leaving the combustion chamber compresses the air coming out of the compressor. After the additional compression of the air in the wave rotor, it is discharged into the combustion chamber. The burned gas expands during the compression of the air and is afterwards scavenged toward the turbine. The channels are then re-connected to the compressor outlet, allowing fresh pre-compressed air to flow into the wave rotor channels; and the cycle starts again. Due to the pre-expansion in the wave rotor, the burned gas enters the turbine with a temperature less than the combustor exit temperature. However, the gas pressure is higher than the compressor exit pressure by the pressure gain obtained in the wave rotor. This is in contrast to the untopped engine, where the turbine inlet pressure is always less than the compressor discharge pressure due to the pressure loss occurring in the combustion chamber.

The general advantage of using a wave rotor becomes obvious when comparing the thermodynamic cycles of baseline and wave-rotor-enhanced engines. Since the wave rotor application was first envisioned and tried for gas turbines (Meyer 1947), this is demonstrated in a schematic temperature-entropy diagram for a gas turbine baseline engine (dashed line) and the corresponding wave-rotor-topped engine (solid line) in Figure I.19.

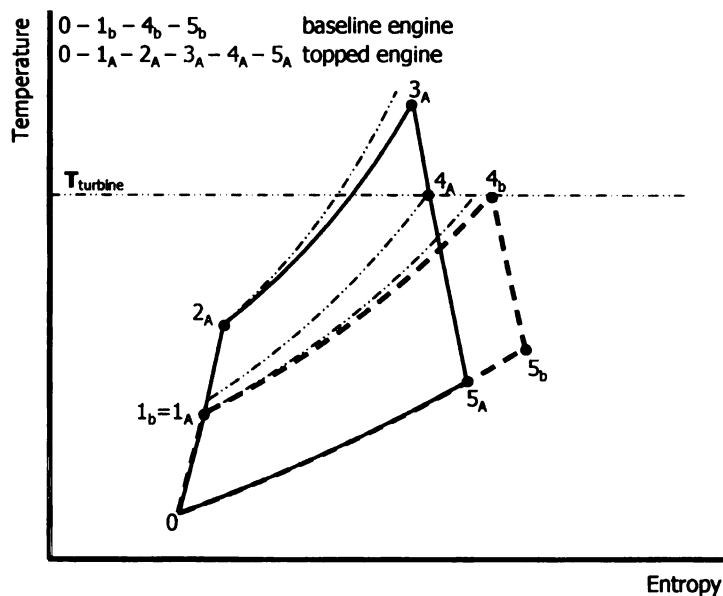


Figure I.19: Temperature –Entropy Diagram for a gas turbine engine with and without wave rotor topping.

While many other advantageous implementation cases of the wave rotor into a given baseline engine are possible (Akbari and Müller 2003; Akbari and Müller 2003). The diagram shows that both the baseline and the enhanced cycle gas turbine are operating with the same turbine inlet temperature and compressor

pressure ratio. However, the output work of the topped engine is higher than that of the baseline engine due to the pressure gain across the wave rotor. In the shown case the amount of heat addition is the same for both cycles. Therefore, the thermal efficiency for the topped engine is higher than that of the baseline engine, which is indicated by the lower entropy production in the wave-rotor- enhanced cycle.

Wave rotors as topping devices for gas turbine cycles have been studied extensively. Since the early 1960s, General Electric Company (GE), General Power Corporation (GPC), and Rolls Royce have been involved in the development of wave rotor prototypes for propulsion applications (Taussig and Hertzberg 1984; Shreeve and Mathur 1985). Mathematical Science Northwest (MSNW) also studied various aspects of wave energy exchange and proposed a wave rotor design for an aircraft turbofan engine (Taussig and Hertzberg 1984). In the 1980s, different US agencies like Defense Advanced Research Program Projects Agency (DARPA) and the US Navy expressed interest and sponsored programs to develop an understanding of wave rotor science and technology. Many developments were presented in the 1985 ONR/NAVAIR Wave Rotor Research and Technology Workshop (Shreeve and Mathur 1985).

Since the late 1980s, A large research program at NASA Glenn Research Center (GRC) collaborated by the US Army Research Laboratory (ARL) and Rolls-Royce Allison has aimed to develop and demonstrate the benefits of wave rotor technology for future aircraft propulsion systems (Paxson 1992; Paxson 1996;

Wilson and Paxson 1996; Welch 1997; Welch 1997; Welch, Jones et al. 1997; Welch 2000). Experimental studies at NASA on four-port (Wilson 1997) and three-port (Wilson and Fronek 1993; Wilson 1997; Wilson 1998) wave rotors enabled the estimation of loss budgets (Paxson 1993; Paxson 1995) and simulation code validation (Paxson and Wilson 1995). The experimental work consisted of two phases. Initially, a simple three-port flow divider wave rotor was built and tested to evaluate loss mechanisms and calibrate the simulation code. Next, a four-port pressure exchanger was built and was tested to evaluate the pressure-gain performance for application to a small gas turbine (Allison 250). However, a study by Rolls-Royce Allison indicated that thermal loads on the rotor and ducting predicted for the NASA wave rotor cycle in real engine conditions may be difficult to manage. The rotor used in testing, as well as the test stand for a four port configuration are displayed in Figure I.20. In response, Nalim and Paxson (Nalim and Paxson 1999; Paxson and Nalim 1999) proposed an alternative cycle with a combustor bypass significantly lowering thermal loads. Sealing and mechanical design issues are being addressed in current NASA tests.

NASA's wave rotor research was later extended to the concept of internal combustion wave rotors (Nalim 1995; Nalim and Paxson 1997; Nalim and Paxson 1997; Nalim 1999) in which both pressure exchange and combustion take place within the wave channels, and further to pulse detonation engines (PDE) taking advantage of constant-volume combustion for higher performance and better



efficiency (Paxson 2001; Schauer, Stutrud et al. 2001; Shimo, Meyer et al. 2002; Wilson and Paxson 2002).

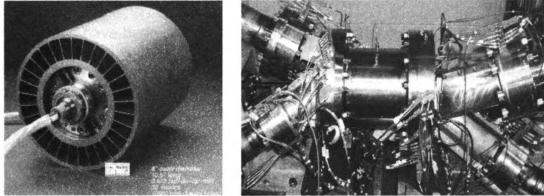


Figure I.20: NASA four port wave rotor. Left – the rotor, Right – the test system.

In a recent study, Akbari and Mueller have performed a thermodynamic analysis to calculate the thermal efficiency and specific work of two unrecuperated microturbines (30 and 60kW) topped with a four-port wave rotor. The engines manufactured by Capstone Turbine Corporation have been widely used recently, and efforts are currently being instituted to increase their performance considerably. The results have predicted overall thermal efficiency and specific work enhancement up to 34% for the smaller engine and 25% for the larger engine, using a four-port wave rotor with a compression ratio of 1.8 (Akbari and Müller 2003). The general performance maps obtained by the authors clearly have demonstrated the considerable performance enhancements of small gas turbines through the use of wave rotors. A similar approach has predicted an improvement up to 15% of overall efficiency and specific thrust in a turbojet

engine using the wave-rotor-topping cycle of the 30kW microturbine flying at an altitude of 10,000m at Mach 0.8 (Akbari and Müller 2003).

### *Car Engine Supercharging*

Wave rotors have been commercially used for internal combustion engines (ICE) as a replacement for conventional superchargers or turbochargers. Compared to the turbocharger, the wave rotor has the advantage of a better response time to engine acceleration (no turbo-lag), and its efficiency does not decrease with the size reduction of the device. These characteristics make the wave rotor more suitable for small displacement engines than the TC, as it can be seen in Figure II.21. The wave rotor has also self-cooling capability, due to the continuous circulation of the air through the rotor.

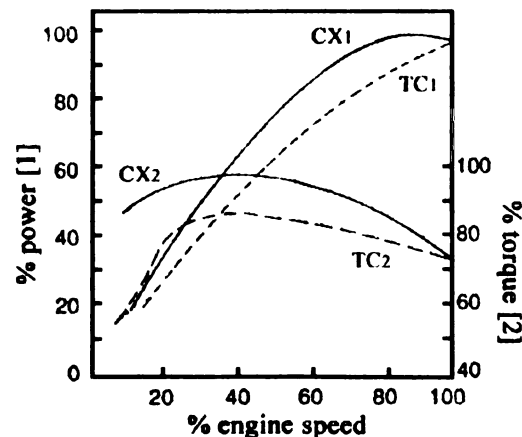


Figure II.21: Comparison between the Compresx<sup>®</sup> supercharged engine (CX) and the turbocharged engine (TC) performances (Heisler 1995).

Figure II.22 displays the main components of the ICE-wave rotor system. The channels are placed axially at the periphery of a cylindrical rotor. In the Compresx<sup>®</sup> case, it is a RF wave rotor, which determines the rotor to have a "hot" side and a

"cold" one. The hot side contains the engine exhaust gases ports, while the air ports are placed on the cold side, as well as the rotor bearings. The engine crankshaft drives the rotor via a belt drive (Doerfler 1975). The wave rotor does not use mechanical work from the engine to compress the air like a mechanical supercharger. Instead, the rotor is driven in order to match the wave phenomena with the load and speed requirements of the engine.

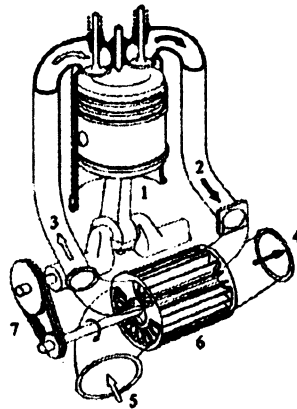


Figure I.22: Compresx<sup>®</sup> system: 1 - ICE; 2 – HPG port; 3 – HPA port; 4 – LPG port; 5 -LPA port; 6 - rotor; 7 - drive system.

The wave rotor is more suitable for a steady-state function, but the ICE works on a wide range of speeds and loads; so there are mismatched working conditions between the two systems. In order to smooth out these problems, so called "pockets" were built inside the stator casing. There are two pockets on the cold side of the stator, the Compression Pocket (CP) and the Expansion Pocket (EP) and a Gas Pocket (GP) on the stator's hot side. The CP deals with the unmatched processes when the engine works at low revs, and the EP and GP help the exhaust gas rotor scavenging process on all loads and speeds range of the engine (Gyarmathy 1983).

The exhaust gas scavenging of the rotor is very problematic, such being the case at low engine loads, like start-up or idling. For these specific conditions, the wave rotor has a starting-valve, which blocks the exhaust gas from entering into the engine cylinders. When the wave rotor is cut-off from the inlet manifolds, the ICE works in a natural-aspired mode. For a better control of the boost-pressure, the Comprex® incorporates a “wastegate valve”, similar to that used on modern turbochargers.

The wave rotor can be driven by a belt drive system or by the exhaust gas, like the turbocharger. This type of Comprex® is called the “free-running” Comprex®. In this case, the speed of the rotor does not have the same importance like it has for the turbocharger because the compression process is not influenced by it. The speed of the wave rotor has only a distribution role, so even if there is a turbo lag, it has little effect on the performance of the free-running Comprex®. This type of wave rotor has a ceramic rotor in order to reduce the inertia and to improve the overall efficiency, unlike the original Comprex®, which had a metal rotor (Zehnder, Mayer et al. 1989).

Brown Boveri Company (BBC), later Asea Brown Boveri (ABB) and now Alston, in Switzerland has a long history in wave rotor technology. As reported by Meyer (Meyer 1947), the first successful wave rotor was tested in the beginning of 1940s as a topping stage for a locomotive gas turbine engine based on patents by Claude Seippel (Seippel 1940; Seippel 1942; Seippel 1946; Seippel 1949). The first wave rotor was not used commercially, mainly because of its inefficient

design and crude integration (Azoury 1992). Later, BBC decided to concentrate on the development of pressure wave superchargers for diesel engines, due to their greater payoff compared to other applications (Taussig and Hertzberg 1984). By 1987, the first wide application of the Comprex® in passenger cars occurred in the Mazda 626 Capella (Mayer, Oda et al. 1989; Zehnder, Mayer et al. 1989). The Comprex rotor and a cut-view of the supercharging system from a Mazda 626 is presented in Figure I.23. Since then, ABB's Comprex® pressure wave supercharger has been commercialized for several passenger cars and heavy diesel engines. The Comprex® has also tested successfully on vehicles such as Mercedes-Benz diesel car (Hiereth 1989), Peugeot, and Ferrari (Taussig and Hertzberg 1984). The main advantage of the Comprex® compared to a conventional turbocharger is its rapid response to changes in engine operating conditions. Furthermore, as the efficiency of the Comprex® is independent of scale, its light weight and compact size make this device attractive for supercharging small engines (below about 75kW or 100HP) (Azoury 1965; Guzzella, Wenger et al. 2000).

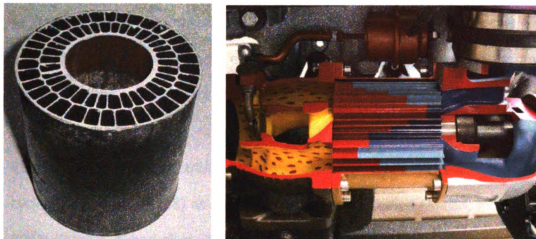


Figure I.23: Comprex® rotor and a Mazda 626 supercharging system cut-view.

Another interesting approach in the wave rotor for ICE area was made in the late 90s by the Swiss Federal Institute of Technology Zurich, Switzerland in collaboration with Swisssauto Wenko AG. Their version of Comprex®, called the Hyprex®, is driven by an electrical motor, which is controlled by the engine's Electronic Control Unit (ECU). The Hyprex® does not have pockets in its stator and rely on a Gas Pocket Valve (GPV) to regulate the boost-pressure and the rotor's scavenging process. The GPV is also controlled by the ECU and has a very important role because the Hyprex® is designed to work on small gasoline engines, where the boost pressure and the EGR rate have a major influence on the energetic and pollution performances of the SI engine (Weber 2001).

### *Refrigeration Applications*

Wave rotors also have been used for air-cycle refrigeration systems (Azoury 1992; Kentfield 1993; Kentfield 1998). Power Jets Ltd in the U.K. utilized wave rotor technology in the design and development of two prototype air-cycle

refrigerators used for environmental cooling purposes. The prototypes were installed and employed in gold mines in India and South Africa and performed the same duty as equivalent vapor-cycle machines but with lower weight and bulk.

Recently, a unique and cutting-edge application of wave rotors in refrigeration cycles using water (R718) as a refrigerant has been studied (Akbari, Müller et al. 2003; Kharazi, Akbari et al. 2004; Kharazi, Akbari et al. 2004; Kharazi, Akbari et al. 2004). In fact, the wave rotor implementation can increase efficiency and reduce the size and cost of R718 units. A three-port wave rotor has been introduced as a condensing wave rotor that employs pressurized water to pressurize, desuperheat, and condense the refrigerant vapor - all in one dynamic process. Besides, giving the possibility of an additional rise of the vapor pressure, the condensing wave rotor eliminates the need of a bulky condenser because full condensation occurs inside the rotor channels. Furthermore, adding a condensing wave rotor to a water refrigeration cycle allows for a lower pressure ratio of the compressor, which is crucial for the R718 chiller technology.

### I.2.2 Numerical Investigations

Among the processes taking place inside the wave rotor cells the main one is the development of compression and expansion waves between gases having different pressures and temperatures. This will constitute the primary energy exchange that takes place inside the cells. Other forms of energy exchanges are:

heat transfer between fluids traveling through the channels and walls and friction losses due to the high viscous aspect of the flow at microscale.

Some assumptions are taken into consideration when writing the governing equations of the flow inside the wave rotor channels. Since the ratio of cell length over the cell width or height is greater than 10, this problem is accepted as being one-dimensional and will be treated as such. The gases involved in the process are considered to be ideal and compressible. Since the perfect gas constant and specific heat ratio are almost equal for air and exhaust gas, it will be assumed in this chapter that all gases have the same properties:  $R=287$  J/kg·K and  $\gamma=1.4$ .

Considering all the presented assumptions, unsteady flow of compressible gas in a one dimensional process is described by the following equations (Shapiro 1953; Anderson 2003).

*Continuity equation*

$$\frac{\partial \rho}{\partial t} + \frac{\partial(\rho u)}{\partial x} = 0 \quad (I.1)$$

*Navier-Stokes equation*

$$\frac{\partial(\rho u)}{\partial t} + u \frac{\partial(\rho u^2)}{\partial x} + \frac{\partial p}{\partial x} - \nu \frac{\partial^2 u}{\partial x^2} - \rho f_x = 0 \quad (I.2)$$

where  $f_x$  are the body forces and  $\nu$  is the kinematic viscosity.

For frictionless flow, the Navier-Stokes equation is reduced to Euler equation.



### *Energy equation*

$$\frac{\partial}{\partial t} \left( \rho \left( e + \frac{u^2}{2} \right) \right) + \frac{\partial}{\partial x} \left( \rho u \left( e + \frac{u^2}{2} \right) \right) + \frac{\partial(\rho u)}{\partial x} - \rho \dot{q} - \rho f_x u = 0 \quad (I.3)$$

where  $\dot{q}$  is the heat flux between fluid and walls.

Several variations of these equations are found in the wave rotor literature since each paper deals with certain aspects of the flow investigations.

Spalding at Imperial College in the United Kingdom is one of the pioneers using a 1D method to investigate unsteady flows inside wave rotors in the early 1970s. He formulated a numerical procedure for wave rotors considering the effects of heat transfer and friction. It utilized novel features to ensure solutions free from instabilities and physical improbabilities, as reported by Azoury (Azoury 1992). Based on this numerical model, a computer program was developed by Jonsson (Jonsson, Matthews et al. 1973), and it was successfully applied to pressure exchangers (Matthews 1969; Azim 1974; Azoury and Hai 1975).

In 1981, Turbopropulsion Laboratory (TPL) at the Naval Postgraduate School (NPS), directed by Shreeve, started an extensive numerical and analytical wave rotor program to evaluate the wave rotor concept and its potential application in propulsion systems (Shreeve, Mathur et al. 1982). For numerical simulations, two different approaches to the solution of the unsteady Euler equations were examined in the overall program. First, Eidelman developed a 2D code based on the Godunov Method to analyze the flow in wave rotor channels (Eidelman 1984; Eidelman, Mathur et al. 1984; Eidelman 1985; Eidelman 1986). Unlike

contemporary one-dimensional approaches (Mathur, Shreeve et al. 1984), the 2D code showed the effect of gradual opening of the channels. The main conclusion of these studies is that if the channels are straight, the flow remains nearly 1D, which in turn leads to minimal mixing losses caused by rotational flow in the channels (Eidelman 1996). However, when the channel of the wave rotor is curved, even an instantaneous opening of the channel does not lead to the development of a 1D flow pattern with small losses. Computation time of such a 2D code has been reported to be quite long. Therefore, interest was given to development of a 1D code introduced by Mathur based on the Random Choice Method solving the Euler equations (Mathur 1985; Mathur and Shreeve 1987). The code which is called WRCOMP (wave rotor component) is first-order accurate in time and it was unconditionally stable. WRCOMP calculated the unsteady process inside the wave rotor, inlet and outlet opening times, and other useful design parameters required for a preliminary design. The outputs from WRCOMP are used in a second program, called ENGINE, performing a performance calculation for a turbofan jet engine (Mathur 1986; Mathur 1986; Roberts 1990). The results have also confirmed the significant performance improvement that could be expected integrating a wave rotor into a turbofan engine. Work was planned toward incorporating the effects of friction and heat transfer into WRCOMP and also including other engine configurations in ENGINE code. Some modifications to WRCOMP code was later started (Salacka 1985;

Johnston 1987), but further development was not pursued after the wave rotor research at TPL-NPS was terminated around 1986.

During 1990s, a few numerical investigations of pressure wave superchargers are reported. Eldin and his associates in Germany developed a fast and accurate numerical method for predicting unsteady flow field in pressure wave machines, using the theory of characteristics (Eldin, Oberhem et al. 1987; Oberhem and Eldin 1990; Oberhem and Eldin 1991; Eldin and Oberhem 1993; Makarious, Eldin et al. 1995; Oberhem and Eldin 1995; Makarious, Eldin et al. 1997). Piechna and his research group at Warsaw University of Technology in Poland have developed experimentally validated 1D and 2D numerical codes to analyze the flow field inside the Comprex<sup>®</sup> (Piechna 1998; Piechna 1998; Piechna 1998; Piechna and Lisewski 1998; Elloye and Piechna 1999; Piechna 1999; Selerowicz and Piechna 1999). Piechna has also proposed a hybrid of the pressure exchanger with internal combustion wave rotor presenting the idea of the autonomous pressure wave compressor (Piechna 2003).

By initiating wave rotor research at NASA Lewis Research Center (now Glenn Research Center) in the late 1980s, Paxson developed a quasi-one-dimensional gasdynamic model by analogy with a shock tube to calculate design geometry and off-design wave rotor performance (Paxson 1992; Paxson and Wilson 1993). The code uses an explicit, second-order, Lax-Wendroff type TVD scheme based on the method of Roe to solve the unsteady flow field in an axial passage for time-varying inlet and outlet port conditions. It employs simplified models to

account for losses due to gradual passage opening and closing, viscous and heat transfer effects, leakage, flow incidence mismatch, and non-uniform port flow field mixing. Recent improvement and validations have completed it as a preliminary and general design tool (Paxson 1995; Paxson 1995; Paxson and Wilson 1995; Paxson 1996; Paxson 1997; Paxson and Lindau 1997; Paxson 1998; Welch, Paxson et al. 1999). Welch has also established 1D and 2D analysis models to estimate the performance enhancements of wave rotors (Welch 1993; Welch and Chima 1993; Welch 1997). Larosiliere has also established a multi-dimensional code to investigate the effect of gradual opening and losses (Larosiliere 1993; Larosiliere 1995; Larosiliere and Mawid 1995).

In 1995, Weber published a book about designing a shock wave engine (Weber 1995). His preliminary design procedures include solving the Riemann problem for a 1D, gasdynamic process. His method is adapted from Shapiro and Rudinger (Shapiro 1953; Rudinger 1969).

Lear at the University of Florida started investigating different configurations of wave rotors by means of analytical and numerical methods. His team developed an unsteady, two-dimensional, numerical code using a direct boundary value method for the Euler equations to analyze the flow in wave rotors and their adjoining ducts, treating the straight or curved channel walls as constraints imposed via a body force term (Lear and Candler 1993). The code was later used to simulate the flow field of the three-port NASA (Wilson and Fronek 1993; Wilson 1997; Wilson 1998) wave rotor A parametric study of gradual opening

effects on wave rotor compression processes is reported, too (Hoxie, Lear et al. 1998).

Fatsis and Ribaud at the French National Aerospace Research Establishment (ONERA) have also developed a 1D, numerical code based on an approximate Riemann solver taking into account viscous, thermal, and leakage losses (Fatsis and Ribaud 1997; Fatsis and Ribaud 1998). The code has been applied to three-port, through-flow, and reverse-flow configurations.

Nagashima, at the University of Tokyo, has developed 1D (Okamoto and Nagashima 2003) and 2D (Okamoto, Nagashima et al. 2001) CFD codes to simulate the flow fields inside through-flow four port wave rotors, including the effects of passage-to-passage leakage. The codes have been validated with experimental data obtained by a single-channel wave rotor experiment.

A simple but very descriptive set of equations is provided by Piechna in this book, *Wave Machines, Models and Numerical Simulation* (Piechna 2005). He takes into consideration wall friction, leakage between rotor and ports, heat transfer, and variation of cross-sectional area and ignores body forces.

#### *Continuity equation*

$$\frac{\partial \rho}{\partial t} + \frac{\partial(\rho u)}{\partial x} + \rho u \frac{d(\ln A)}{dx} \pm \frac{\dot{m}}{A} = 0 \quad (\text{I.4})$$

#### *Momentum equation*

$$\frac{\partial(\rho u)}{\partial t} + u \frac{\partial(\rho u^2)}{\partial x} + \frac{\partial p}{\partial x} + \rho u^2 \frac{d(\ln A)}{dx} + f_p \frac{u|u|}{2D} \pm u \frac{\dot{m}}{A} = 0 \quad (\text{I.5})$$

### *Energy equation*

$$\frac{\partial(\rho e)}{\partial t} + \frac{\partial(\rho u^2)}{\partial x} + \frac{\partial(\rho u p)}{\partial x} + u(\rho e + p) \frac{d(\ln A)}{dx} - \frac{\dot{q}}{A} \pm e \frac{\dot{m}}{A} = 0 \quad (\text{I.6})$$

where

- $A$ : channel local cross-sectional area
- $\dot{q}$ : heat flux to cell walls
- $\dot{m}$ : mass flow rate of leaks
- $\frac{d(\ln A)}{dx}$ : variation of cross-sectional area along the length of channel
- $e = \frac{u^2}{2} + \frac{1}{\gamma - 1} \frac{p}{\rho}$ : internal energy of the flow

### *Wave Rotor Simulations with Commercial CFD Packages*

Some attempts at simulating pressure wave superchargers with the help of commercial codes already have been undertaken. One such code is GT-POWER in which pipe elements have been divided into a series of objects for which the conservation equations have been solved. By dividing variables into primary (density, total internal energy) and secondary variables (pressure, temperature) a staggered grid has been the result of discretization. Sets of elementary elements can be connected into one net, controlling the flow between them. The pipe elements can also include wall friction and heat transfer. Proper modules can represent local changes of pipe cross-section or valve system. An interesting

description of techniques for optimization of timing, shaping, and control of pressure wave changers using GT-POWER has been described by Podhorelsky et al. (Podhorelsky, Macek et al. 2004).

For the preliminary tests results generated here the commonly available CFD software FLUENT has been used. The present work shows 2D results of simulating complete operation of a novel radial wave rotor (wave disc) with straight channels and curved channels. Details of the operation of an aerodynamic speed control and the oblique opening of curved channels are described as well. Furthermore, 3D results of a complete conventional axial wave rotor are presented proving the capability of this software. For most of the results investigated here, no experimental data exist for possible verification. The only concept for which data are available is the conventional axial wave rotor. It seems that such types of models are useful for the final tests of devices for which the geometry has been already optimized by the use of specialized, but much simpler, 1D codes. The presented results shall not be interpreted as a proposition of a particular geometry for practical applications. While they can be a base for further investigations, they rather present some illustrations of physical phenomena generated in different configurations and phases of operation and showing the capability of the code.

### **I.3 Wave Rotor Enhanced Ultra Micro Gas Turbines**

The concept of adding a wave rotor to an ultra-micro gas turbine was addressed by several research groups from all over the world. With great experience gathered in the wave rotor field, Ribaud at ONERA was attracted by this idea and at begin studying the possibilities of incorporating a wave rotor to an ultra-micro gas turbine. A more extensive work was done by the University of Tokyo research group directed by Nagashima. An initial test stand with a single stationary channel was built. The length of the channel was 180mm. The results were compared with 2D CFD simulations (Okamoto, Nagashima et al. 2003). Further, a numerical model was designed for a wave rotor with channel length of 6.9mm (Okamoto and Nagashima 2003).

Recently, Michigan State University in collaboration with the Warsaw University of Technology is intensively searching for a feasible method of topping an ultra-micro gas turbine with a wave rotor. The new proposed design of wave rotors, which have the channels placed radial instead of axial with respect to the axis of rotation, appears to be the solution to the problem (Piechna, Akbari et al. 2004). Several proposed designs of *Ultra – Micro Wave Rotors (U $\mu$ GT)* are presented next.



## **Chapter II**

### **PROPOSED INITIAL DESIGNS OF A WAVE ROTOR**

#### **TOPPING AN U $\mu$ GT**

##### **II.1 Axial Wave Rotor Configuration**

Starting from a baseline engine similar to the one developed by the MIT research group, several wave rotor topped, ultra-micro gas turbine configurations are proposed (Iancu, Akbari et al. 2004). The wave rotor works on a four-port configuration, namely each cycle is completed once the wave rotor channels make contact at one end or the other with all four ports. The overall aspect of the wave rotor may include a larger number of ports depending on the number of cycles per revolution.

Figure II.1 shows a wave rotor added at the outer diameter of the disk formed by compressor/turbine unit. The end plates with the ports at either side of the wave rotor can be etched in the same wafer as the stationary guide vanes. The second possible design implies using additional wafers allowing a multi-layer rotor, as shown in Figure II.2. The major challenge with this design is the perfect axial alignment of the compressor/turbine unit with the wave rotor (may be achieved with the common laser aligning method). The flow connection from the compressor to the wave rotor may be viewed as a challenge in respect to keeping the pressure loss small. However, the equivalent diameter of this

connection may be designed sufficiently large. Further, this may aid in isolating the compressor case from the combustor heat, especially with the counter flow of the compressed air, where a regenerative effect is seen again. The third design concept introduces a new idea in respect of having free spinning wave rotors located circumferentially around the compressor/turbine unit, as shown in Figure II.3. Similar to the first classic design, this design requires less wavers than the second design, which translates into lower fabrication cost. The challenge associated with this design is driving the wave rotors at the appropriate speed, which may be achieved by arranging the wave rotor ports in proper angles so that the impulse of the fluid streams can be utilized.

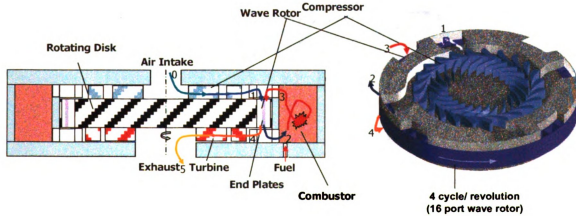


Figure II.1: Conceptual design of UμGT – "Classic" design.

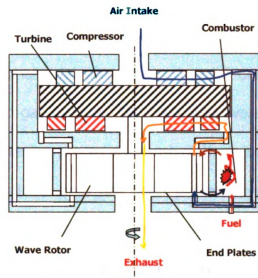


Figure II.2: Conceptual design of U $\mu$ GT – "Two-layer" design.

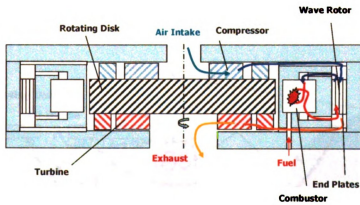


Figure II.3 Conceptual design of U $\mu$ GT – "External" design.

## I.1 Radial Wave Rotor Configuration

A new and innovative design is proposed next (Piechna, Akbari et al. 2004). Instead of the traditional axial wave rotor, a radial one seems to be far more suitable for ultra-micro gas turbines. Its shape and overall surface to height ratio is ideal for microfabrication processes, most of them being 2D processes. Plus, the variable cross-sectional area has been proven to provide a more efficient shock wave compression (Pfeifer and Garlich 1990). The radial wave rotor (wave disc) will be incorporated, as the axial one, in parallel with the combustor; schematics are shown in Figure II.4. Unlike the axial configurations, the channel shape along its length can be tailored in width and angle.

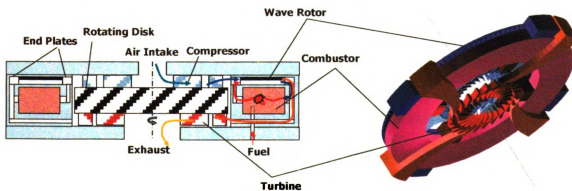


Figure II.4: Conceptual design of U $\mu$ GT – "Radial" design.

For most thermodynamic applications, axial-flow wave rotors have mostly been used and investigated. Pure scavenging is a challenging task in the axial-flow configurations. In gas turbine applications, through-flow configurations

recirculate a fraction (30 to 50%) of combustor products to the combustion chamber (Welch, Jones et al. 1997). Even though reverse-flow configurations can deliver pure compressed air to the combustion chamber, a buffer layer can remain in the channels. This residuum can remain permanently in the channels. Repeated compression waves increase the temperature of this buffer layer. This leads to high wall temperatures in the center of the channels (Nalim and Paxson 1999). It is possible to achieve a full scavenging process for both through and reverse-flow configurations using bypassing or bleeding of certain mass flows (Zauner, Chyou et al. 1993; Nalim and Paxson 1999; Paxson and Nalim 1999). However, all of this leads to more complex configurations.

Jenny and Bulaty (Jenny and Bulaty 1973) have introduced a conical wave rotor with oblique channels in which a radial component is added to the axial flow. However, the flow still enters and leaves at the front and rear end respectively and predominantly in axial direction. They have noticed the positive influence of centrifugal forces on the scavenging process. The idea was not pursued further due to restrictions in computational power. These extensive calculations of unsteady flow with the effect of centrifugal forces proved to be impossible.

The radial-flow wave (wave disc) concept employs the flow in radial and circumferential directions. This can substantially improve the scavenging process by using centrifugal forces. Figure II.4 shows schematically a simple radial-flow wave rotor with straight channels and a rectangular cross-sectional area.

# **Chapter III**

## **PERFORMANCE CHARACTERISTICS OF**

### **ULTRA-MICRO WAVE ROTORS<sup>1</sup>**

The way in which the wave-rotor topping enhances the cycle at micro scale often differs from that at larger scales. At a large scale, the goal is mostly either to increase the cycle overall pressure ratio or to substitute the wave rotor for costly high pressure turbomachinery stages. The most significant performance gain has been found for engines with low compressor pressure ratio and high turbine inlet temperature (Wilson and Paxson 1993; Fatsis and Ribaud 1999). At the ultra-micro scale, the optimum cycle pressure ratio is very small, e.g. around 2, due to the low component efficiencies (Müller and Fréchette 2002). Thus, a single-stage centrifugal compressor can easily generate the low optimum overall pressure ratio, and a further increase with the same efficiency actually decreases the desired performance. Therefore, the wave rotor integration is most effective if its compression and expansion efficiencies are greater than those of the turbomachinery components of the baseline engine. This enhances not only the overall compression and expansion efficiencies, but it also increases the optimum cycle pressure ratio to a greater value, allowing for additional performance improvements. In such a case where the wave rotor compression efficiency is higher than that of the spool compressor, a wave rotor can enhance the

---

<sup>1</sup> Part of the material presented in this chapter was published in the Journal of Microfluidics and Nanofluidics (Iancu and Müller 2005)

performance of an U $\mu$ GT that was already designed for an optimum pressure ratio. Then while the optimum overall compression ratio increases with the wave rotor integration, the pressure ratio of the spool compressor can be usually decreased. This can additionally enhance the isentropic efficiency of the spool compressor, provided its polytropic efficiency (aerodynamic quality) stays the same. These effects are schematically shown in Figure III.1.

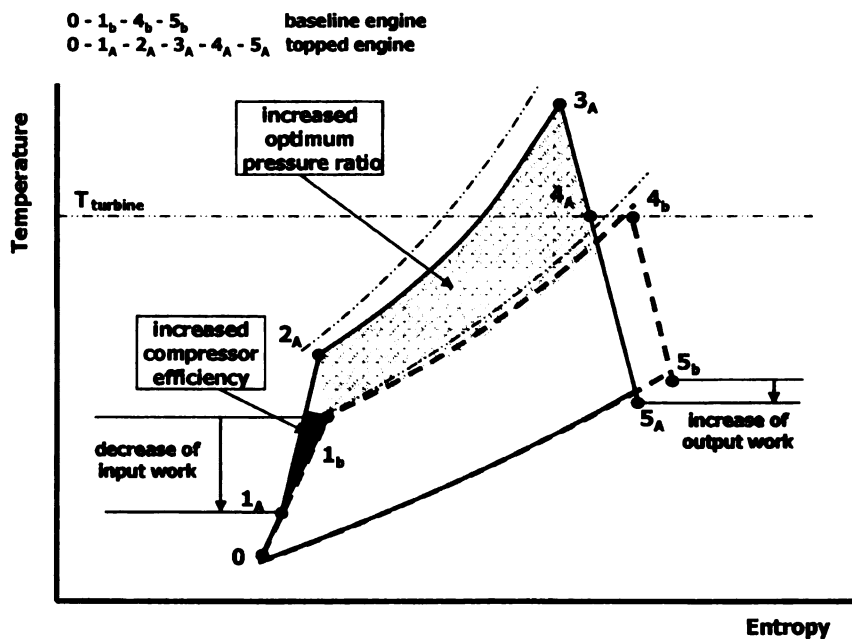


Figure III.1: Temperature – Entropy diagram for ultra-micro gas turbines, with and without wave rotor.

The turbine inlet temperature may stay the same while the combustion takes place at a higher temperature. Alternately, the turbine inlet temperature may be lowered. An additional pressure gain to that provided by the compressor is also obtained by the wave rotor. Therefore, the performance enhancement is

achieved by increasing both the overall efficiency and specific power, hence reducing the specific fuel consumption considerably.

An initial study on the efficiency of the compression process in a wave rotor channel has shown that values around 70% can be achieved at microscale (Iancu, Akbari et al. 2004). For large scale wave rotors the value of 83% is consistent throughout the literature.

While the wave rotor efficiency is based on the efficiency of the shock wave compression inside each channel, the influence of external losses can be at a minimum since the wave rotor itself is the only moving part. External losses are leakage, windage, and friction in the bearings of the rotor. At micro scale losses due to sharp bends in the flow path to the rotor since rounded corners are very difficult to obtain in the etching direction. All these losses also occur in turbomachinery, but in a wave rotor they can be lower, since the compression process is only controlled but not accomplished by the rotational speed of the rotor. Therefore, high efficiency can be obtained even at relatively low rotational speed, which implies less friction.

As explained above, the implementation of a wave rotor at ultra-micro scale appears most effective if its compression efficiency is greater than that of the baseline spool compressor. Whereas the latter ranges low around 50% at ultra-micro scale compared to about 70 – 90% at large scale, the compression efficiency of wave rotors ( $\eta_{wc}$ ) has been found to be in the range of 70 – 86%, assuming that the wave rotor expansion efficiency is equal to its compression



efficiency ( $\eta_{WT} = \eta_{WC}$ ). This may be considered as matching the efficiency of large scale compressors or turbines and almost double of that achieved with ultra-micro scale compressors. The favorable wave rotor efficiencies are subsidized by the following.

Table III.1: Wave rotor compression and expansion efficiency and only compression efficiency. Data found in extant literature

Source	$\eta_{WT} \cdot \eta_{WC}$	$\eta_{WC}$
Taussig (Taussig 1984)	0.70 – 0.74	<i>0.83 – 0.86</i>
Rolls-Royce, Moritz (Moritz 1985)	0.6	<i>0.77</i>
Kollbrunner (Kollbrunner 1981)	<i>0.36 – 0.46</i>	0.60 – 0.68
Wilson and Paxson (Wilson and Paxson 1993)	<i>0.69</i>	0.83
Fatsis and Ribaud (Fatsis and Ribaud 1999)	<i>0.64 – 0.70</i>	0.80 – 0.86

(Italic figures are calculated assuming  $\eta_{WC} = \eta_{WT}$ )

Thus, it appears that  $\eta_{WC} = \eta_{WT} = 0.83$  is a reasonable assumption for a large scale wave rotor with a cell length of about 100-300mm (Zehnder and Mayer 1984). For the smallest documented wave rotor with a channel length of 69mm (Okamoto, Nagashima et al. 2003), using the wave-rotor characteristic equation (Eq. III.1 below) introduced by Wilson and Paxson (Wilson and Paxson 1993) and  $\eta_{WC} \cdot \eta_{WT}$ , the authors calculated an isentropic compression efficiency of about 79%.

$$\frac{P_{t4}}{P_{t1}} = \Pi_{comb} PR_W \left\{ 1 - \frac{\frac{c_{pair}}{c_{pgas}} \frac{1}{\eta_{WT} \cdot \eta_{WC}} \frac{T_{t1}}{T_{t4}} \left[ PR_W^{\frac{\gamma_{air}-1}{\gamma_{air}}} - 1 \right]}{1 + \frac{c_{pair}}{c_{pgas}} \frac{1}{\eta_{WC}} \frac{T_{t1}}{T_{t4}} \left[ PR_W^{\frac{\gamma_{air}-1}{\gamma_{air}}} - 1 \right]} \right\}^{\frac{\gamma_{gas}}{\gamma_{gas}-1}} \quad (III.1)$$

Exploring the application of even smaller wave rotors suitable for ultra-micro gas turbines, the question arises if such wave rotor efficiencies can be maintained at ultra-micro scale. No values are available at this scale. However, the above results show no or only a small decrease in efficiency with reduced size, which encourages investigations at the ultra-micro scale.

Using the available wave rotor efficiencies above versus the corresponding wave rotor channel length, a trend can be generated as shown as a solid green line in Figure III.2. The simple linear extrapolation predicts wave rotor efficiency at ultra-micro scale (about 1mm channel length) that is greater than 70%. Such a compression efficiency of a microfabricated wave rotor is much better than the obtained efficiencies of around 50% for microfabricated compressors (Müller and Fréchette 2002). Furthermore, efficiency values of compressors suitable for or corresponding to the reported wave rotor topped cycle are shown red in Figure III.2. This allows showing the red broken trend line for the compressor efficiency corresponding to the wave rotor length. Both trends for the wave rotor efficiency and for the compressor efficiency coincide at larger scale. However, towards smaller wave rotor size for  $U_{\mu GT}$ , the compressor efficiency trend falls far below the wave rotor efficiency trend. This clearly suggests an advantage of using a wave rotor for  $U_{\mu GT}$ .

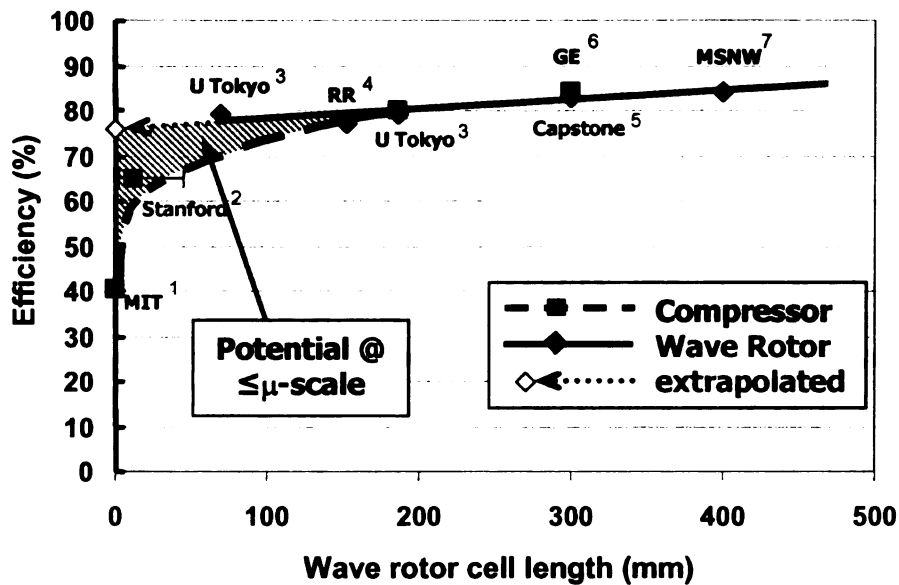
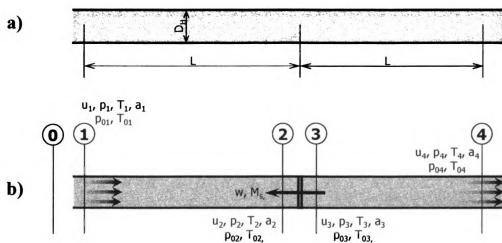


Figure III.2: Efficiency trend of the compression process. Solid line – wave rotor efficiency; Dashed line – compressor efficiency. References: 1 – (Müller and Fréchette 2002), 2 – (Johnston, Kang et al. 2003), 3 – (Okamoto and Nagashima 2003), 4 – (Moritz 1985), 5 – (Akbari and Müller 2003), 6 – (Mathur 1985), 7 – (Thayer 1985).

The trend line in Figure III.2 suggests a wave rotor compression-efficiency of about 75% at micro scale. To investigate the practical relevance of this simply extrapolated trend line of the wave rotor compression-efficiency a mathematical model was created based on a physical background. The model considers the entropy production by a single normal shock that runs through the wave rotor channel and the wall friction generated by the gas flowing through the channel. Entry losses due to ducting are also taken into consideration. The only effects neglected were those of heat transfer.

Focusing on the phenomenon occurring inside a single channel, the one-dimensional mathematical model is based on the gas dynamics of normal shock waves for one-dimensional flow as described by Anderson (Anderson 2003). The

model assumes air as a working fluid that is modeled as an ideal gas, and a friction coefficient along the channel to be a variable function of gasdynamic conditions. The wave rotor channel is simulated as a tube with an equivalent hydraulic diameter  $D_H$  as shown in Figure II.2-a. The model relates the efficiency of the compression process to the velocity, pressure, and temperature of the gas at the entrance of the channel (station 1:  $u_1, p_1, T_1$ ), the pressure ratio across the shock  $\Pi_S$ , the friction coefficient  $f$ , and tube dimensions  $2L$  and  $D_H$ . In Figure II.2-b, a shock wave is shown that moves in the opposite direction of the flow that is positioned in the middle of the channel. Later, it will be proved that a snap shot evaluation at the mid position is a good representation of the overall results and does not affect the accuracy of the model. Friction is considered along the lengths  $L$  before and after the shock.



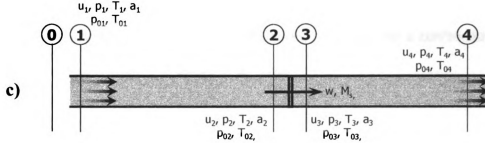


Figure II.2: 1D model of a microchannel. a) Single channel; b) Shock traveling in direction opposite to the flow; c) Shock traveling in direction of the flow.

From the equations of a one-dimensional, compressible flow with friction, starting with the conditions at station 1 we can deduce the conditions at station 2, just before the arrival of the shock wave. The frictional effect is modeled as shear stress at the wall acting on a fluid with uniform properties over the cross section. Although the wave rotor channels have a rectangular or trapezoidal shape, the calculations are performed using the equivalent hydraulic diameter  $D_H$

$$D_H = 4 \frac{A}{P} \quad (\text{III.2})$$

In the case of a one-dimensional model, the flow is studied based on the infinite parallel plates case, where

$$D_H = 2D \quad (\text{III.3})$$

Since the port will have a dimension larger than that of the channel, the entry losses are treated as losses due to variation of diameter in a pipe. The pressure drop is

$$\Delta p = k \cdot \rho \cdot \frac{u^2}{2} \quad (\text{III.4})$$

Where the entry loss coefficient,  $k$  is considered to be 0.5 for a contraction with sharp 90 degree corners (Sabersky et al. 1998).

### III.1 One Dimensional Flow with Friction

Knowing the temperature and velocity at station 1, we can compute the speed of sound using Eq. III.5 and in turn the Mach number with Eq. III.6.

$$a = \sqrt{\gamma \cdot R \cdot T} \quad (\text{III.5})$$

$$M = \frac{u}{a} \quad (\text{III.6})$$

In order to find the Mach number at station 2, we use the sonic condition as it develops due to friction, through station 2, from the flow in station 1. The virtual distance from station 1 that is needed for the flow to reach sonic conditions is denoted with  $L_1^*$  and can be calculated using Eq. III.7, which is derived from the momentum equation, expressing the shear stress in terms of friction coefficient and integrating between station 1 and the point where  $M=1$  (Anderson 2003).

$$L_1^* = \frac{D}{4 \cdot f} \left[ \frac{1 - M_1^2}{\gamma \cdot M_1^2} + \frac{\gamma + 1}{2 \cdot \gamma} \cdot \ln \left( \frac{(\gamma + 1) \cdot M_1^2}{2 + (\gamma - 1) \cdot M_1^2} \right) \right] \quad (\text{III.7})$$

The classical theory of laminar flow relates the friction coefficient to be proportional to the Reynolds number.

$$f = \frac{64}{Re} \quad (\text{III.8})$$

But the Reynolds number is dependent on density, viscosity, velocity, and hydraulic diameter (Eq. III.9). The first two are related to the temperature, one by ideal gas law, the second by Sutherland law (Eq. III.10).

$$Re = \frac{\rho \cdot u \cdot D_H}{\mu} \quad (\text{III.9})$$

$$\mu = \mu_{ref} \left( \frac{T}{T_0} \right)^{1.5} \frac{T_{ref} + S}{T + S} \quad (\text{III.10})$$

where  $\mu_{ref} = 1.789 \cdot 10^{-5}$  kg/ms is the reference viscosity,  $T_{ref} = 273.11$  K is the reference temperature, and  $S = 110.56$  K is the effective temperature in the three coefficients Sutherland law (Sutherland 1893).

Since the same sonic condition develops from the flow in station 1 and 2, the difference between the two virtual distances to sonic condition is the distance between stations  $L$ .

$$L = L_1^* - L_2^* \quad (\text{III.11})$$

By applying Eq. III.7 to the station 2 and substituting  $L_2^*$  from the Eq. III.11 we can solve Eq. III.7 for the Mach number  $M_2$ . Knowing the Mach number at station 2 and all the conditions at station 1, and applying the continuity equation in adiabatic conditions, the pressure and temperature at station 2 can be calculated with Eqs. III.12 and III.13:

$$p_2 = p_1 \cdot \frac{M_1}{M_2} \cdot \sqrt{\frac{2 + (\gamma - 1) \cdot M_1^2}{2 + (\gamma - 1) \cdot M_2^2}} \quad (\text{III.12})$$



$$T_2 = T_1 \cdot \frac{2 + (\gamma - 1) \cdot M_1^2}{2 + (\gamma - 1) \cdot M_2^2} \quad (\text{III.13})$$

Adiabatic conditions were assumed for the analytical one-dimensional model, justified by numerical results obtained for relevant cases as shown further below. Using a CFD code, a 2D model was investigated with and without adiabatic walls. Comparing the pressure and temperature distributions revealed errors below 1%, as displayed in Figure III.4. The set-up conditions for the model are described in the following section.

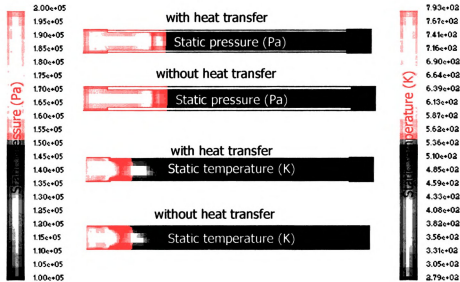


Figure III.4: Pressure and temperature distributions for a single channel model with heat transfer calculations and without. Flow moving from left to right. The results were obtained using FLUENT 6.1.

### III.2 Flow Across a Moving Shock

Knowing  $T_2$ , the speed of sound  $a_2$ , can be calculated with Eq. III.5 and then the velocity of the flow  $u_2$ . Assuming that the distance between stations 2 and 3 is negligible and knowing the pressure ratio across the shock,  $\Pi_s = p_3/p_2$ , conditions at 3 can be obtained employing the normal shock relations (Eqs. III.14 and III.15).

$$T_3 = T_2 \cdot \Pi_s \cdot \left( \frac{\frac{\gamma+1}{\gamma-1} + \Pi_s}{1 + \frac{\gamma+1}{\gamma-1} \cdot \Pi_s} \right) \quad (\text{III.14})$$

From the three basic Euler equations, the Mach number of the shock wave,  $M_s$ , can be evaluated as follows:

$$M_s = \sqrt{\frac{\gamma+1}{2\gamma} \cdot (\Pi_s - 1) + 1} \quad (\text{III.15})$$

Knowing that  $M_s = w/a_2$ , it results that the velocity of the shock wave,  $w$  is

$$w = a_2 \sqrt{\frac{\gamma+1}{2\gamma} \cdot (\Pi_s - 1) + 1} \quad (\text{III.16})$$

and the induced velocity of the flow behind the wave  $u_p$  is

$$u_p = \frac{a_2}{\gamma} \cdot (\Pi_s - 1) \cdot \sqrt{\frac{\frac{2\gamma}{\gamma+1}}{\frac{\gamma-1}{\gamma+1} + \Pi_s}} \quad (\text{III.1})$$

The velocity of the flow at station 3 is a vector sum of the initial velocity of the flow and the velocity induced by the moving shock wave.

$$\vec{u}_3 = \vec{u}_2 + \vec{u}_p \quad (\text{III.2})$$

From station 3 to station 4, the same algorithm is applied as for the flow traveling from 1 to 2.

Since this is an unsteady process the total properties behind the shock at station 3 are different from the ones in front of the shock (station 2). The total pressure is calculated using the known properties of the induced mass motion instead of being directly calculated from the equation of state (Anderson 2003).

The isentropic efficiency of the compression process is defined as the temperature difference for an isentropic process versus a real process (Dixon 1998):

$$\eta_c = \frac{\Delta T_s}{\Delta T} \quad (\text{III.3})$$

For the model presented here it can be calculated by

$$\eta_c = \frac{\left(\frac{p_4}{p_1}\right)^{\frac{\gamma_{air}-1}{\gamma_{air}}} - 1}{\frac{T_4}{T_1} - 1} \quad (\text{III.4})$$

The model described in this dissertation is applied to compressible air flow with Reynolds numbers in the range of 500 to 1500. These values were obtained using Eq. III.9, which is also valid for shock wave propagation in a narrow channel (Sun, Ogawa et al. 2001). Further, based on the analysis of gas flow characteristics in silicon microchannels by Ying-Tao and his research group (Ying-Tao, Zhao-Hui et al. 2002), the friction coefficient  $f$  has been found to be approximately 0.04 for a Reynolds number of 500, while for Reynolds numbers greater than 1000, the friction coefficient becomes less than 0.005. In the paper, Ying-Tao and his group concluded that the discrepancy between the theoretical friction factor and the experimentally found one is due to the gas compressibility effect. They describe the analysis that leads to the conclusion that the density in the streamwise direction is not constant, since the relation between pressure ratio and mass flow rate is not constant. Next, the friction coefficient is plotted with respect to the Reynolds number for the theoretical calculations and experimental values (Figure III.5).

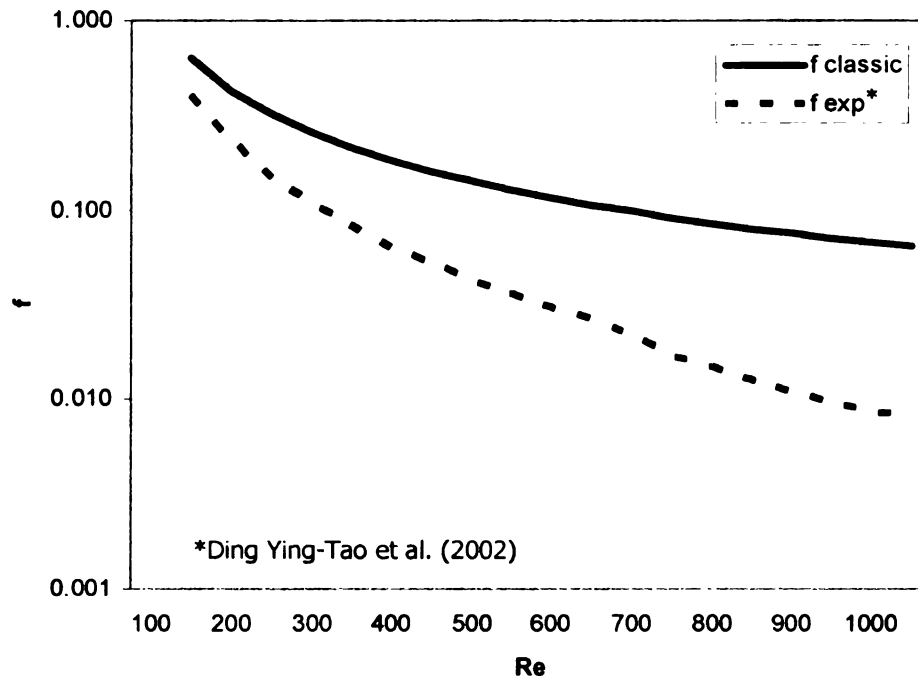


Figure III.5: Variation of friction factor with respect to Reynolds number assuming laminar flow: solid line – calculation using classic theory ( $f=64/Re$ ); dotted line – experimental results for microscale flow.

Table III.2: Entry data for the mathematical model

Property	Value
Static inlet pressure, $p_0$	$2.57 \cdot 10^5$ Pa
Static inlet temperature, $T_0$	1465 K
Inlet velocity, $u_0$	350 m/s
air specific heat ratio, $\gamma_{air}$	1.4
air specific gas constant, $R_{air}$	287 J/kg·K
channel length, $L$	$10^{-3}$ m
channel diameter, $D$	$76 \cdot 10^{-6}$ m

The entry data for the model have been introduced based on preliminary thermodynamic calculations of a wave rotor suitable for an ultra-micro gas turbine (Iancu, Akbari et al. 2004) and initial thermodynamic parameters used by

the MIT Micro Gas Turbine group (Kang 2001; Epstein 2004; Fréchette, Jacobson et al. 2005), as well as micro turbomachinery design space calculations of Müller and Fréchette (Müller and Fréchette 2002) . The data are found in Table III.2.

Since the shock is moving through the channel, the calculations were made on discrete time steps (snapshots), at which the shock was found in discrete positions with respect to the channel length.

Finding afterwards, average values of compression efficiency by integrating the values of efficiency obtained at the discrete time steps with respect to channel length, it was found that these integral efficiencies are well represented by the discrete efficiency value calculated for the moment (snapshot) when the shock wave moves through the center position of the tube. The error introduced by this approximation is in the range of 0 to 5% and considered negligible. This is due to an almost linear dependence of the discrete efficiencies of the compression process on the momentary position of the moving shock in the channel. This is shown in Figures III.6 and III.7 for different pressure ratios across the shock. The efficiency values averaged over the channel length are shown by horizontal lines for each shock pressure ratio. It is seen that the average values for each pressure ratio correspond very well to the respective discrete efficiency values found at the half channel length position, which justifies the use of the snapshot value at the half channel position as a representative value for the entire compression process during which the shock wave moves through the full length of the channel.

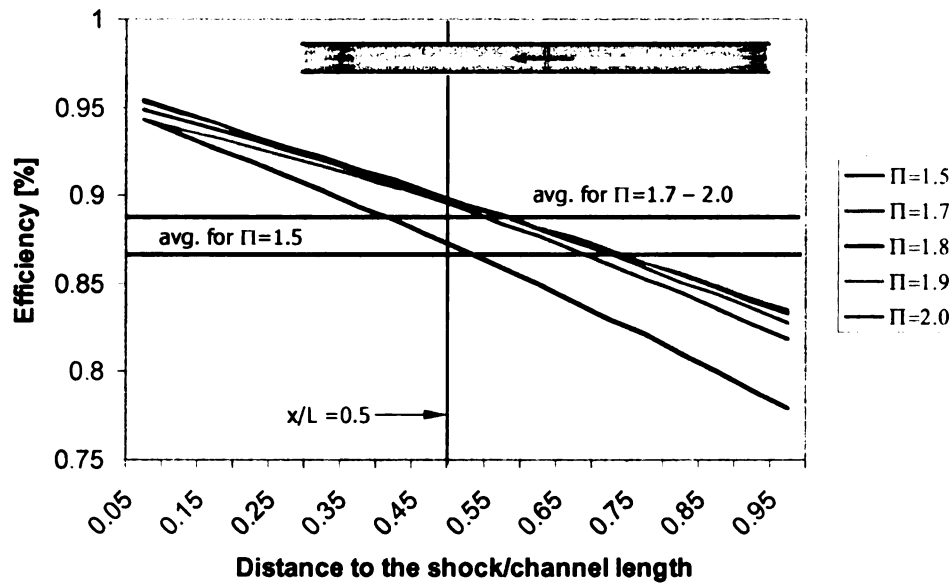


Figure III.6: Efficiency of compression process as function of position of shock inside the microchannel for different shock strengths, inlet temperature of 1465K, and a shock traveling in direction opposite to the flow. Results obtained using analytical 1D code.

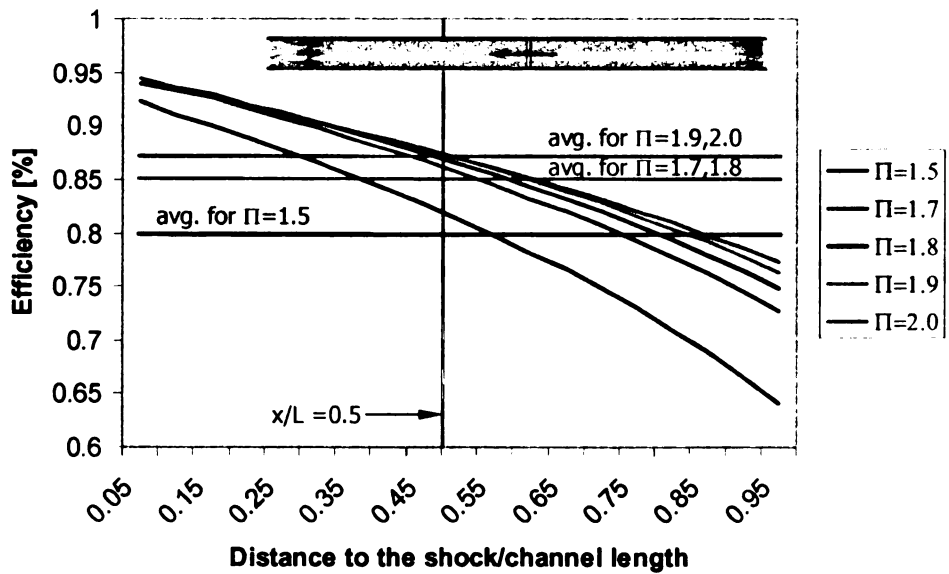


Figure III.7: Efficiency of compression process function of position of shock inside the microchannel for different shock strengths, inlet temperature of 750K, and a shock traveling in direction opposite to the flow. Results obtained using analytical 1D code.

Results in Figure III.6 have been obtained for an entry temperature of 1465K, while for Figure III.7 a temperature of 750K has been used. Figure III.8 presents the results for a shock traveling in the direction of the flow for an entrance temperature of 1465K.

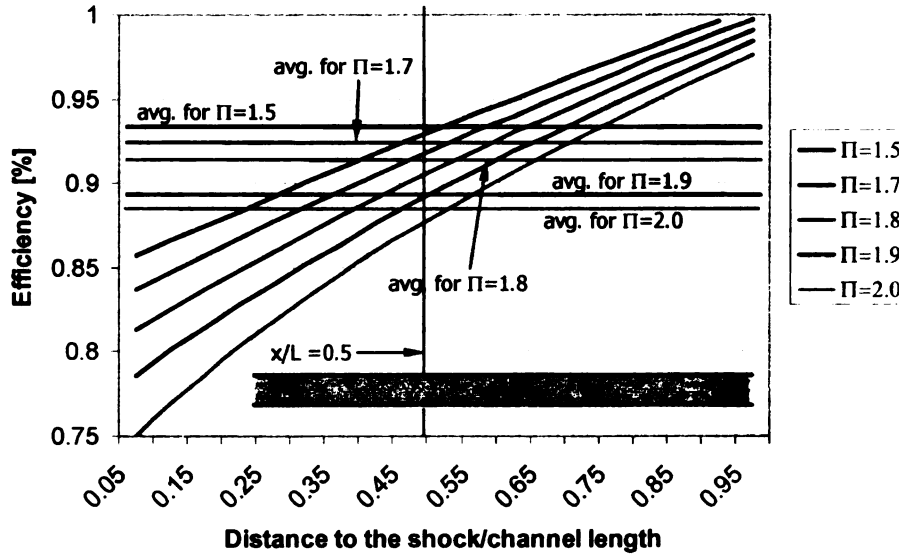


Figure III.8: Efficiency of compression process as function of position of shock inside the microchannel for different shock strengths, inlet temperature of 1465 K, and a shock traveling in the direction of the flow. Results obtained using analytical 1D code.

Comparing results of efficiency for both directions of the shock wave, a small difference between the averaged values of both cases is noticed. When the flow travels along the tube, its pressure drops due to the friction losses (Eqs. III.7 to III.13). Assuming the flow moves from station 1 to station 4 and there is a constant pressure ratio across the shock, the following scenarios can be seen.

If the flow meets the shock close to station 1, the pressure loss from 1 to 2 is very small due to the short length traveled. Then, the shock increases the pressure to a high  $p_3$ , while it afterwards gradually reduces to  $p_4$ , resulting in a



relative high average pressure throughout the tube. Therefore, the average density is relatively high, the average flow velocity relative low, and the losses are relative small. If the flow meets the shock close to station 4, the pressure in front of the shock  $p_2$  is already considerably lower than in the previous case due to the pressure loss incurred by now traveling the much longer distance between station 1 and 2. The shock brings then the pressure up to  $p_3$  that is only a little more than  $p_4$ , since there is only a small pressure loss from 3 to 4 due to the short distance. The pressure behind the shock will be much less than in the previous case, even though the pressure ratio is the same in both cases. Consequently, the average pressure throughout the tube is relatively low; and, therefore, the average density is relatively low too, requiring high average flow velocity that causes greater frictional losses reducing the efficiency of the compression process as seen in Figures III.6 and III.8. A schematic of this process with snapshots for both cases is presented in Figure III.9.

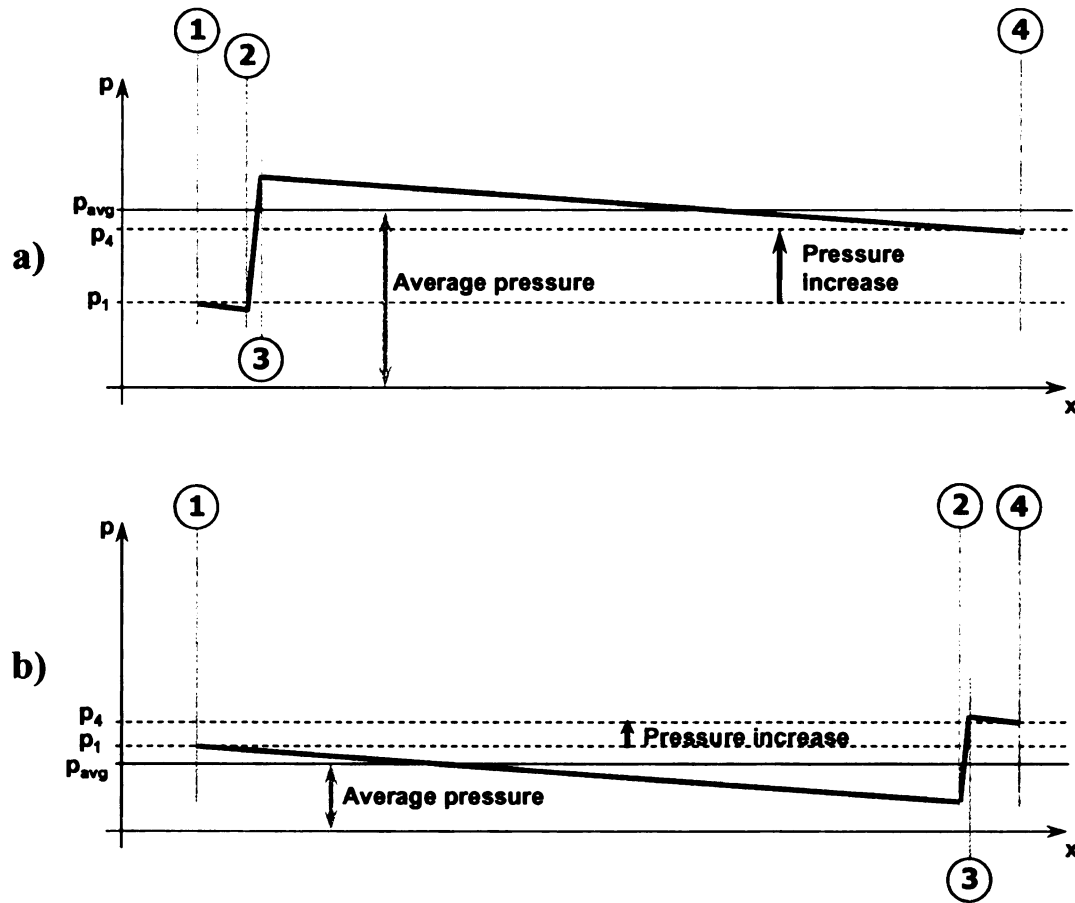


Figure III.9: Schematic of pressure distribution along the microchannel. a) With shock close to entrance; b) With shock close to exit. Pressure  $p_1$  and ratio  $p_3/p_2$  are the same in both cases.

The effect is reversed when the shock wave is moving in the same direction as the flow since the higher pressure is behind the shock and the highest pressure is at the entrance of the flow and not at the exit. The efficiency is higher if the shock is closer to station 4, as Figure III.9 shows. Also, if the shock wave and flow have the same direction, it is seen that the efficiency increases with decreasing pressure ratio.

Thus, for obtaining a maximum efficiency, for a primary shock wave that travels in the same direction a lower pressure ratio would be preferred and a higher

pressure ratio for a reflected shock wave traveling in opposite direction. But since the reflected shock cannot be stronger than the primary one, a compromise has to be made in order to choose the optimum pair of pressure ratios for both shocks. The results presented above are summarized in Table III.3. The table reveals a maximum efficiency for the opposite direction of flow and shock wave. Such a maximum is not found for same direction of flow and shock wave, since pressure ratios lower than 1.5 are too small to compensate the friction losses.

Table III.3: Efficiencies of compression process function of shock pressure ratio, entrance temperature and direction of moving shock

	$\Pi_s = 1.5$	$\Pi_s = 1.7$	$\Pi_s = 1.8$	$\Pi_s = 1.9$	$\Pi_s = 2.0$	$\Pi_s = 2.1$
$T_0=1465K$						
same direction	<i>0.929</i>	0.921	0.908	0.893	0.877	0.855
$T_0=1465K$						
reverse direction	0.865	0.890	0.893	<i>0.894</i>	0.892	0.890
$T_0=750K$						
reverse direction	0.801	0.849	0.858	0.863	<i>0.865</i>	0.864

For further investigations, the following justified approximation will be employed: discrete efficiencies values obtained for the moving shock at the half channel length position approximate an average value for the entire shock wave compression. The variation of the efficiency with the inlet temperature is presented next.

A variable friction coefficient is introduced for these simulations. The friction coefficient is dependent on the Reynolds number and indirectly on viscosity and

temperature. Using Eq. III.20, the efficiency results for various entry temperatures and shock strengths were calculated. Since according to Ying-Tao (Ying-Tao, Zhao-Hui et al. 2002), for a laminar flow at microscale, the friction coefficient does not depend linearly on the Reynolds number, therefore a second set of efficiencies for the same range of inlet temperatures were generated using their experimentally obtained dependence of the friction coefficient on the Reynolds number. These two sets of efficiency are presented in Figure III.10. As noticed, the efficiencies obtained with the experimentally determined friction coefficient are about 10% higher than the ones obtained using the theoretical friction coefficient. For each pressure ratio across the shock, an optimum entry temperature can be found, which will lead to highest efficiency. Another observation that can be made is that the values of efficiency vary only a little with entry temperature, justifying the use of a constant friction coefficient determined for the inlet temperature. This effect is caused by the dual influence of the temperature: higher temperature leads to a lower Mach number for the same inlet velocity but lower Reynolds number, thus higher friction coefficient. The effect of lower Mach number and higher friction coefficient are opposite when calculating the characteristic length in Eq. III.7.

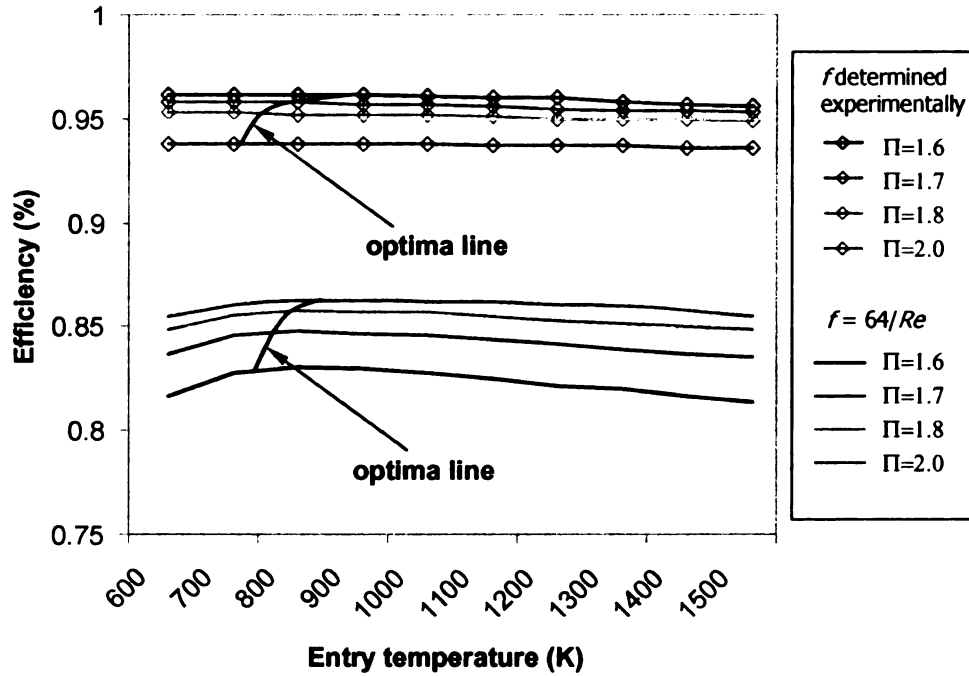


Figure III.10: Efficiency of compression process as function of entry temperature for different shock strengths, and for a shock traveling in the direction opposite to the flow. Results obtained using analytical 1D code.

An important parameter in wave rotor design as well as shock tube design is the length/diameter ratio. In the relevant case of an ultra-micro wave rotor, the ratio was chosen to be 6.67, due to microfabrication constraints. But a variation of this parameter over a wider range showed that the efficiency does not vary significantly, variation being more considerable for lower pressure ratios. For a shock strength,  $\Pi_s = 1.8$  the variation is only 3.3% for a diameter from  $D_H = 30\mu\text{m}$  up to  $100\mu\text{m}$  and a 1mm channel length. According to the above findings in these calculations the friction coefficient is based on the inlet temperature and the experimental graph shown in Figure III.5. Efficiency results are plotted in Figure III.11. The left graphs present the results versus length/diameter ratio with shock pressure ratio as parameter, while the graph on the right side is like a

side view with the length/diameter ratio as parameter. On the right side the solid line connects the optimum pressure ratios for maximum efficiency for each length/diameter ratio.

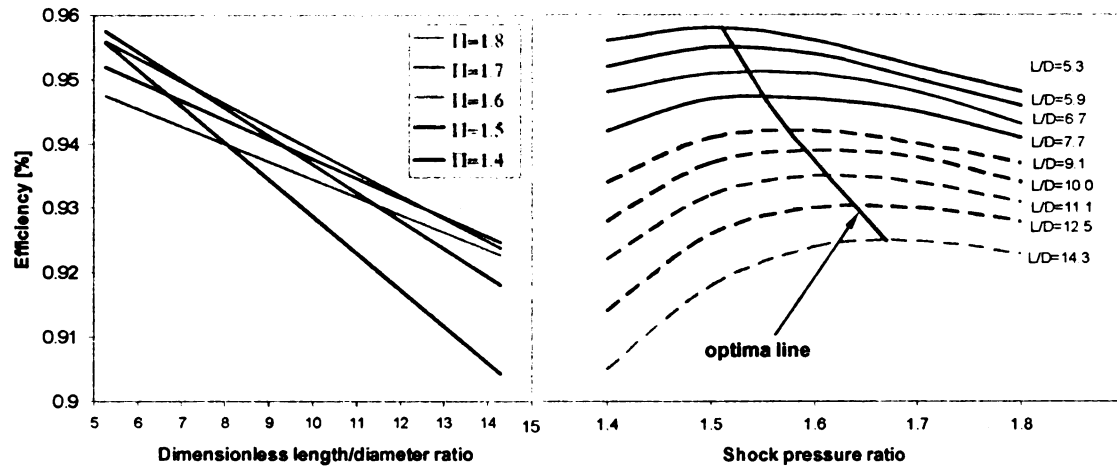


Figure III.11: Efficiency of compression process function of microchannel length/diameter ratio for different shock strengths, and for a shock traveling in the direction of the flow.

### **III.3 Numerical Model**

Several researchers have investigated compressible flow in microchannels. Some have focused on recovering the characteristics of the flow (Xue and Chen 2003), others studied the behavior of compressible flow at microscale and the differences in relation to large scale (Papautsky, Ameen et al. 2001). In the present work a numerical model was created to validate the analytical model described in section 3 and to explore the flow behavior at microscale.

A 2D numerical model was designed to simulate the best possible the real life conditions in a wave rotor channel. The channel modeled is 1mm long and 76 $\mu$ m wide and has a larger inlet duct (port) and opens into a larger outlet port (Figure III.12). GAMBIT 2.0 was used to create the mesh and set up the interface, initial conditions, and boundary zones for the given geometry. The mesh size in channels and inlet and outlet ports was carefully selected to provide accurate and fast solutions. Tetrahedral mesh was used with a 2 $\mu$ m cell size for the channel and a paved 10 $\mu$ m cells for the inflow and outflow ports. Tests showed that finer meshes would not provide more accurate results but only cause additional computational time. For the mesh, standard quad elements were used in a map and pave type distribution. The pave distribution was used to connect the finer mesh of the channel with the coarser mesh of the ports. Once the grid was generated in GAMBIT, the mesh was imported into FLUENT 6.1. Boundary conditions, solving method, working fluids type, convergence criterion, and several other functions (parameters) were defined prior to the simulation.

The fluid material used in modeling the flow was air, treated as a compressible ideal gas. The specific heat and thermal conductivity were kept constant, while the viscosity varies with temperature, according to Sutherland's law.

For the model including heat transfer, the solid walls were modeled out of silicon, assuming constant density and specific heat, and thermal conductivity modeled as temperature dependent. Values of the material's constants can be found in the Appendix 1.

An implicit solver model of FLUENT was used, coupling the conservation and momentum equations with the energy equation and the flow was treated as laminar, viscous and unsteady (Iancu, Piechna et al. 2005).

Boundary conditions at inlet and outlet ports play important roles in flow field simulations, since a specific pressure jump across the shock cannot be defined. A pressure inlet was set up on the left edge (side) of the inlet duct, and similarly a pressure outlet was set up at the far right side of the outlet duct. The channel and the duct (ports) were initially assumed to be filled with fluid at constant pressure and temperature. A high pressure, high temperature fluid was supplied through the pressure inlet zone. To the entire fluid region, an axial motion was induced with the velocity  $u_z$ . These boundary conditions (pressures, temperatures and velocities) are presented in Table III.2. The meshed model is presented in Figure III.12. The conditions were specified via "patch" option for the left side reservoir similar with conditions in the table III.2. The rest of surfaces (channel and right side reservoir) were initialized at ambient conditions.



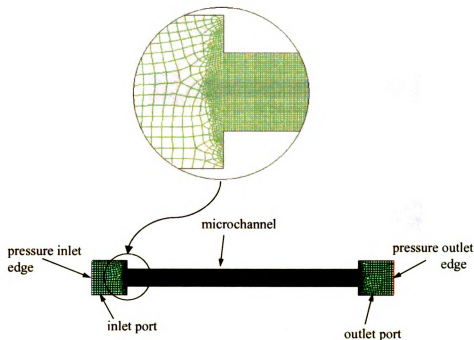


Figure III.12: Mesh models of a microchannel, inlet and outlet ports.

Using the results obtained with the CFD model described above, efficiency values can be established for the compression process, based on the values of pressure and temperature across the shock and using Eq. III.20. This is simplified by the fact that the properties in front of the shock (right side) are constant up to the end of the channel. Further, it can be seen in the CFD results that for the initial part of the process, the pressure drop is confined over a short distance (between stations 2 and 3 in Figure III.13 above. As the shock wave travels further from the left to the right, the pressure gradient dissipates more and more continuously over a longer range. Instead of a well defined shock wave, it then can be seen as a set of compression waves distributed over more than a half of the length of the channel (Figure III.13 below).

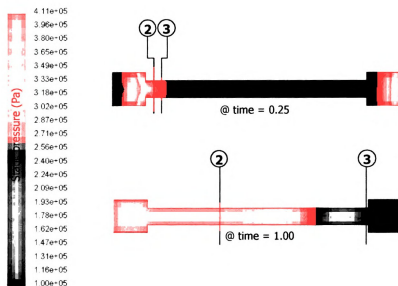


Figure III.13: Static pressure inside a microchannel at two different time steps. Time =1 is when pressure wave reached the end of the channel. Flow moving from left to right. Results obtained using CFD code FLUENT 6.1.

This effect has already been noted by Brouillette in his experiments with microscale shock tubes (Brouillette 2003), and it originates from the stronger influence of the viscous forces at low Reynolds numbers. In the density contour plot (Figure III.14), the existence of the boundary layer can be seen clearly, behind the shock wave as soon as it has traveled about 20% of the channel length.

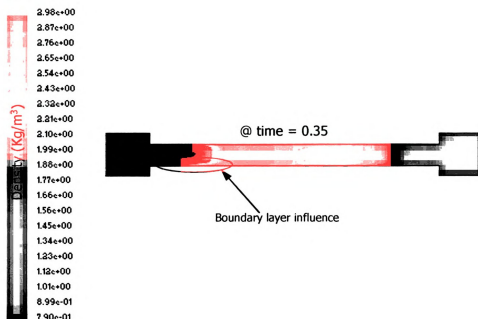


Figure II.1: Density contours inside a microchannel. Time=1 is when pressure wave reached the end of the channel. Flow moving from left to right. Results have been obtained using CFD code FLUENT 6.1.

### III.4 Comparison of Results

Keeping a constant  $L/D_H$  ratio of 6.67, a scale influence on the efficiency of the shock wave compression process was investigated. The upper continuous line in Figure III.15 presents this effect based on the presented analytical one-dimensional model. Two sets of data points are shown along with this graph. Using the CFD model, the efficiencies of compression process for two cell lengths were calculated (for 1mm and 2mm). At the same time the literature results initially presented in Figure III.2 are placed on the graph. It is observed that the analytical 1D model over predicts the efficiency of the compression process mainly because it represents only the gasdynamic process inside the wave rotor cells, while the literature results present the efficiencies of wave rotor systems as a whole. It can be concluded that the analytical model over predicts the efficiency by approximately 10% to 15%. This difference is attributed to additional losses not considered in the presented model. These are mainly due to leakage between the channel ends and the end plates, but also some due to heat transfer and slight off-design operation. Accounting for these losses additionally to the results of the analytical model, a real compression efficiency of 65 – 70% can be predicted for microscale ultra-micro wave rotors with channel lengths in the order of 1mm. The results have been obtained using Eq. III.20, the formula of the isentropic compression efficiency.

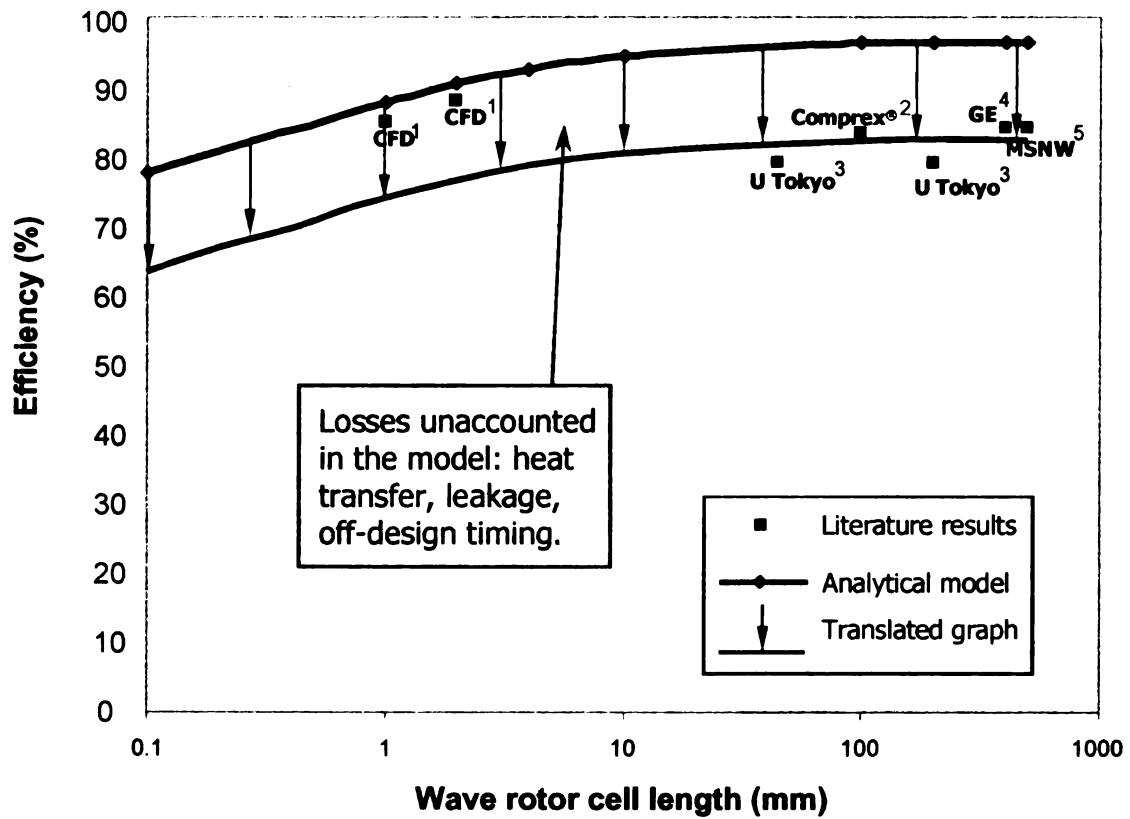


Figure III.15: Wave rotor compression efficiency as function of channel length for constant length/diameter ratio of 6.67. References: 1 – CFD model, 2 – (Zender and Mayer 1984), 3 – (Okamoto and Nagashima 2003), 4 – (Mathur 1985), 5 – (Taussig 1984).

### **III.5 Design Space of Wave Rotor Topped Gas Turbines at Microscale<sup>2</sup>**

The following graphs try to identify optimum design points from the point of view of Specific Fuel Consumption (SFC), specific work or thermal efficiency. Several parameters are taken into consideration as variables, one by one, while the rest are kept constant for finding these optimum points of wave rotor enhanced gas turbines, from which initial operating conditions can be determined in the initial phase of the design process (Akbari 2004; Dempsey, Akbari et al. 2005).

The performance maps below are generated using for the first the first time variable wave rotor efficiency as described in the sections III.1 to III.4. This way the efficiency of the compression due to shock waves, thus the inner wave rotor gasdynamic process, is linked to the overall thermodynamic turbomachinery cycle.

The design points used for input to the CFD simulations in this work may not be found in the above shown optimum design maps, since these were not available until very recently. However they represent viable design solutions to the integration of a wave rotor to an ultra-micro gas turbine. The focus of the present work in terms of optimization is on the geometry and port timing of the wave rotor, not to the overall turbomachinery cycle as it has been in the cited works of Akbari and Dempsey. The recommendations for future work will include updating the U<sub>μ</sub>WR design for the new optimum design points.

---

<sup>2</sup> The results presented in this section were obtained with the indispensable help of Emmett Dempsey, MS student at MSU – Turbomachinery Laboratory.

Figure III.16 presents the optimum points found for a range of polytropic compressor efficiency of 0.41 to 0.81. The procedure uses fixed  $\eta_{PC}$  and  $\Pi_{WR}$  and variable  $R$  for finding one optimum point, then  $\eta_{PC}$  is incremented to the next value. It was observed that as  $\eta_{PC}$  increases, thermal efficiency ( $\eta_{th}$ ), specific work ( $w$ ) and baseline compressor pressure ratio ( $R$ ) increase, while SFC decreases. Optimum thermal efficiency lines are shown as bold light green lines, specific work lines of are shown as bold blue lines and SFC lines in red. All lines of constant  $\Pi_{WR}$  are shown as thin dashed orange lines.

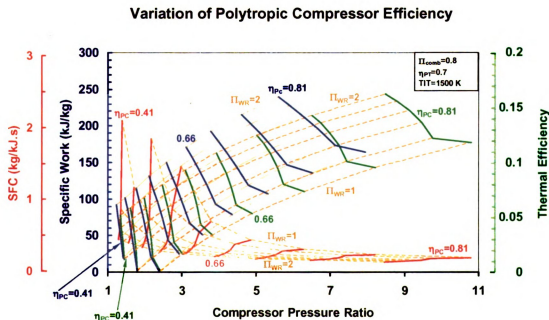


Figure III.16: Optimum points for all performance evaluation parameters function of polytropic compressor efficiency.

Next, the optimum points for polytropic turbine efficiency variation are presented in Figure III.17.  $\eta_{PT}$  took values in the range 0.6 to 0.95. The constant parameters for both variations of turbine and compressor polytropic efficiencies were  $TIT=1500$  K and  $\Pi_{comb}=0.8$ . For variation of turbine polytropic efficiency,  $\eta_{PC}$  was kept constant at 0.46, while  $\eta_{PT}=0.9$  for variation of compressor polytropic efficiency. These values were the optimum values generated by Müller and Fréchette in their study on micro gas turbines (Müller and Fréchette 2002). The same conclusions as for variation of compressor polytropic efficiency can be drawn in the case of variable turbine polytropic efficiency. As  $\eta_{PT}$  increases, thermal efficiency ( $\eta_{th}$ ), specific work ( $w$ ) and baseline compressor pressure ratio ( $R$ ) increase, while SFC decreases.

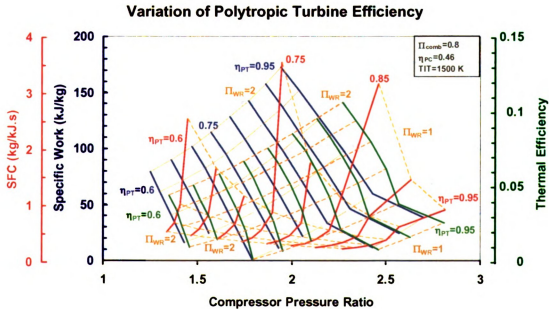


Figure III.17: Optimum points for all performance evaluation parameters function of polytropic turbine efficiency.



Probably the most important parameter in construction the wave rotor for  $U_{\mu}GT$  design space is the Turbine Inlet Temperature. Several graphs present optimum points for SFC, specific work and thermal efficiency, based on variable TIT. Figure III.18 shows a comparison of all the performance measuring parameters and their response to the increase of TIT from 1300K to 2000K.

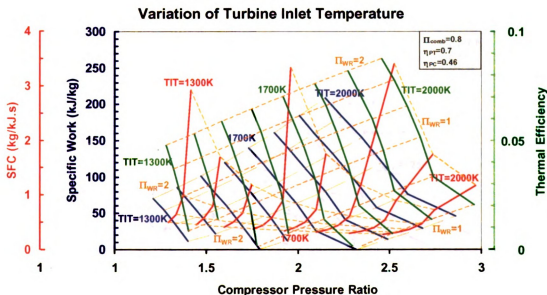


Figure III.18: Optimum points for all performance evaluation parameters function of turbine inlet temperature (TIT).

The expected response is observed, for both untopped ( $\Pi_{WR}=1$ ) and topped ( $\Pi_{WR}>1$ ) engines, as TIT increases, also  $\eta_{th}$ ,  $w$ , and  $R$  increases, while SFC decreases.

The following three graphs (Figures III.19, III.20, III.21) present the same results as Figure III.18, but taking each performance evaluation parameter ( $\eta_{th}$ ,  $w$  or SFC) separately. Using the approach stated above, TIT and  $\Pi_{WR}$  were fixed

while  $R$  was varied to locate one optimum point, then increment  $TIT$  and  $\Pi_{WR}$  to the next fixed value to find the next optimum point. Some extra lines are shown on the graphs. Compressor exit temperature lines ( $T_c$ ) are displayed as vertical dashed lines, turbine inlet pressure ratio ( $p_4/p_0$ ) in dashed brown lines and overall pressure ratio lines ( $\Pi_O$ ) in dark dotted lines. The same constants  $\Pi_{comb}=0.8$ ,  $\eta_{PC}=0.46$  and  $\eta_{PT}=0.9$  were used in this case.

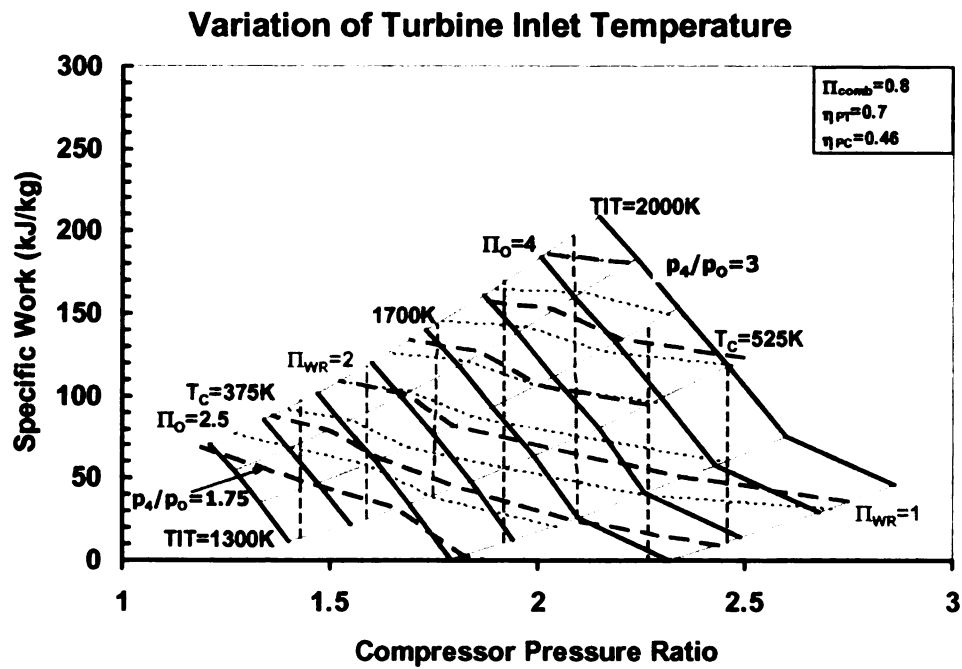


Figure III.19: Optimum points for specific work for variation of turbine inlet temperature (TIT).

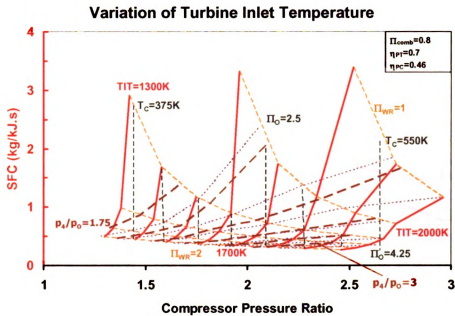


Figure III.20: Optimum points for specific fuel consumption for variation of turbine inlet temperature (TIT).

It can be seen that from the thermal efficiency point of view, for a fixed wave rotor compression pressure ratio of 2 (like the one used for all the numerical simulations so far), and a fixed turbine inlet temperature of 1500K, the optimum point would be for a baseline compressor pressure ratio of 1.6 (Figure. III.21).

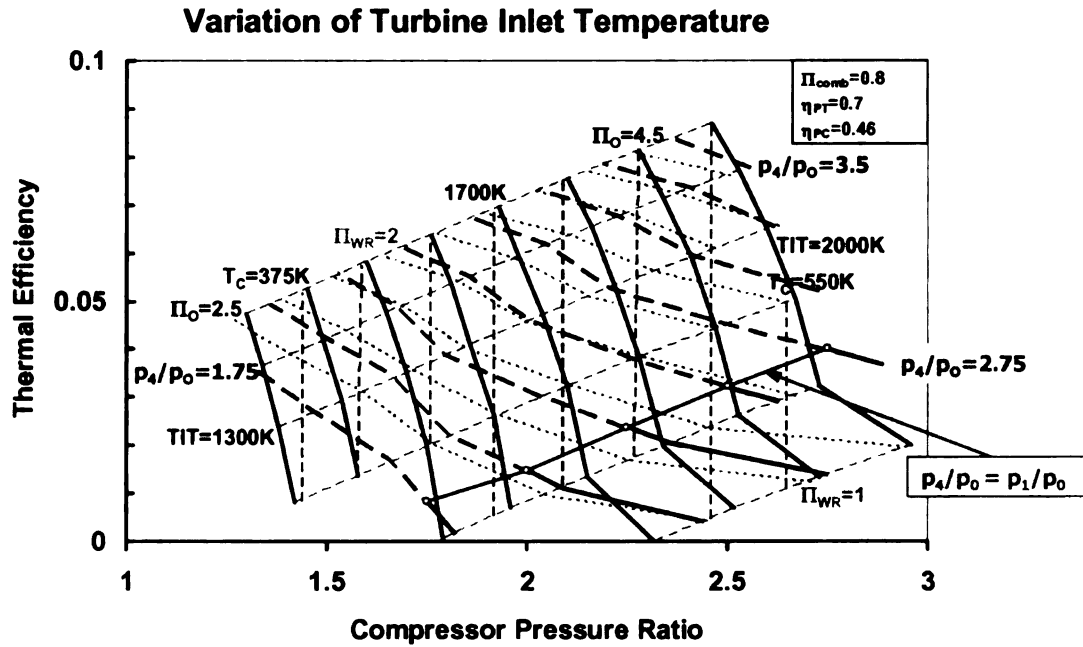


Figure III.21: Optimum points for thermal efficiency for variation of turbine inlet temperature (TIT).

Also, on the thermal efficiency graphs a new line was highlighted (solid orange line) denominated  $p_4/p_0 = p_1/p_0$  which represents the optimum points where the pressure at the turbine inlet is the same as the pressure at the compressor exit. Or, in wave rotor terms, the LPA pressure is equal to the LPG pressure. The red lines at the right of the equal pressures line represent points in the design space where the pressure at the turbine inlet is lower than the pressure at the compressor exit. During the previous analysis of the wave rotor input data, in section V.3, the point of LPA=1.95 bar and LPG=1.62 was used. Although this configuration with the turbine inlet pressure lower than the combustor exit one has not been documented before, the design space analysis performed here shows that such a phenomenon occurs even for thermodynamically optimized design point. The explanation of this fact lays in the high of the combustor

pressure loss ratio at microscale. With the same baseline engine (compressor, combustor and turbine) but without wave rotor, this thermodynamic cycle would not be self-sustained. Although the cycle does not show a pressure gain from compressor to turbine, the wave rotor introduces a gain by reducing the effective pressure drop from compressor to turbine through the combustion chamber and only its use enables a positive work output of the thermodynamic cycle.

## **Chapter IV**

### **STRESS INVESTIGATIONS**

#### **IV.1      Materials Used and Properties**

The proposed materials for fabrication are silicon (Si), polycrystalline silicon (Poly-Si), silicon carbide (SiC), and silicon nitride (Si<sub>3</sub>N<sub>4</sub>). Polycrystalline diamond (Poly-C) can be used for microfabrication of a test rig. This test rig can be used only for compressibility measurements, using compressed air as working fluid, since the maximum sustainable temperature of Poly-C is 500K.

*Silicon* is the most common material used in MEMS fabrication. It offers a sum of advantages: great structural characteristics, commercial availability, and extensive knowledge of fabrication technology. Table A.1 in Appendix 1 presents the main characteristics of Si.

*Silicon carbide* and *Silicon Nitride* can be used to create a hybrid, reinforced structure, by etching channels in silicon and depositing SiC. Properties of these two materials are listed in Appendix 1, Tables A.2 and A.3.

## IV.2 Radial and Tangential Stresses with and without Thermal Effects

The compressor/turbine unit was analyzed as a solid disk with constant thickness ( $t$ ). The schematic of this assembly is presented in Figure IV.1.

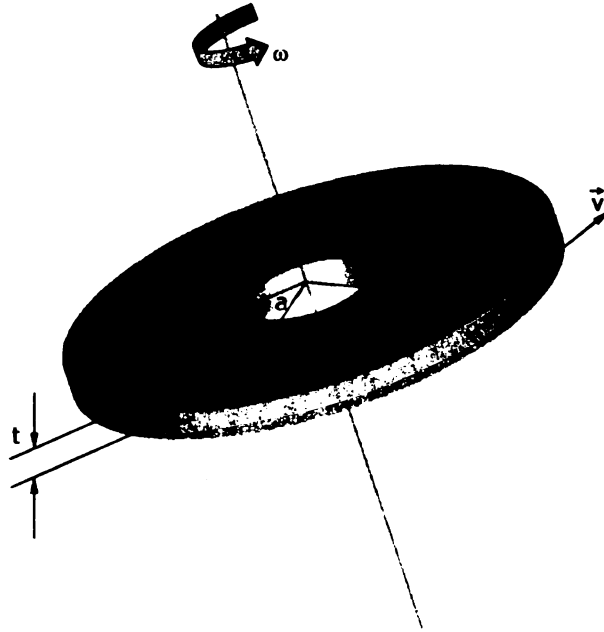


Figure IV.1: Model of a single compressor/turbine disc.

### IV.2.1 No thermal effects

Two cases were analyzed. One is the stress state without the thermal effects, radial and tangential stresses being generated only by centrifugal force, due to high speed of rotation (Ugural and Fenster 1995).

$$\sigma_r(r) = \frac{\gamma v^2}{g} \frac{3+\nu}{8} \left( 1 - \frac{r^2}{b^2} \right) \quad (\text{V.1})$$

$$\sigma_t(r) = \frac{\gamma v^2}{g} \frac{3+\nu}{8} \left( 1 - \frac{3+3\nu}{3+\nu} \frac{r^2}{b^2} \right) \quad (\text{V.2})$$

where:

$a = 0\text{m}$  (inner radius of the disk)

$b = 8 \cdot 10^{-3}\text{m}$  (outer radius of the disk)

$v = 388\text{ m/s}$  (tangential velocity)

$g = 9.81\text{ m/s}^2$  (gravitational acceleration)

$\rho = 2320\text{ kg/m}^3$  (density)

$\gamma = \rho \cdot g$  (specific weight)

$\alpha = 4.2 \cdot 10^{-6}\text{ 1/}^\circ\text{C}$  (thermal expansion coefficient)

$E = 160\text{ GPa}$  (elastic modulus)

$\nu = 0.28$  (Poisson's ratio)

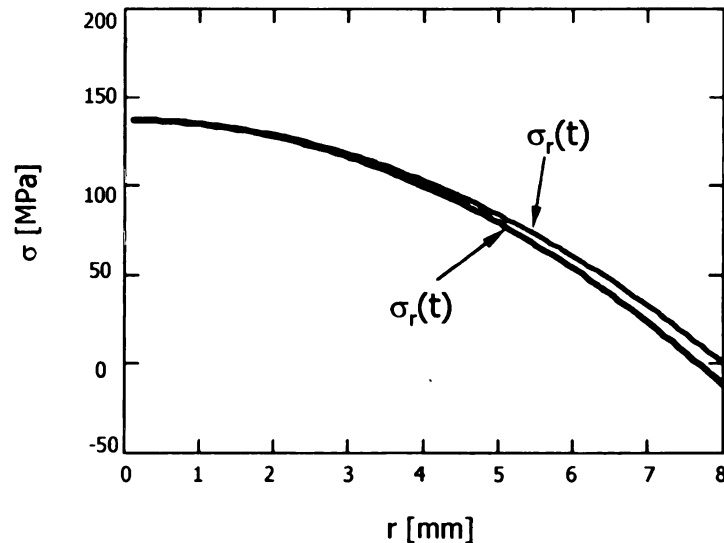


Figure IV.2: Radial and tangential stresses without thermal effects along the radius of the disk (compressor/turbine rotor).

The results show that radial and tangential stresses have almost identical patterns and values. Although the maximum stress is noticed at the center of the disc, its value is influenced by the radius of the disc and its velocity.



#### IV.2.2 Thermal effects

The equations for the radial and tangential stresses with thermal effect are the following (Timoshenko 1956).

Radial stress:

$$\sigma_r(r) = \frac{\alpha E}{1-\nu} \left( -\frac{1}{r^2} \int_a^r T(r) r dr + \frac{r^2 - a^2}{r^2(b^2 - a^2)} \int_a^b T(r) r dr \right) \quad (V.3)$$

Tangential stress:

$$\sigma_\theta(r) = \frac{\alpha E}{1-\nu} \left( \frac{1}{r^2} \int_a^r T(r) r dr + \frac{r^2 + a^2}{r^2(b^2 - a^2)} \int_a^b T(r) r dr - T(r) \right) \quad (V.4)$$

For temperature distribution, three cases were analyzed:

- linear
- quadratic
- logarithmic

A linear distribution of the temperature on the radial direction was assumed for the calculations. Maximum temperature, which is the turbine inlet temperature (TIT) occurs on the outer radius. At the center of the disk, atmospheric conditions were assumed.

$$T_1(r) = (T_{max} - T_{init}) \frac{r}{b} + T_{init} \quad (V.5)$$

$$T_{min} = 300 \text{ K}$$

$$T_{max} = 1465 \text{ K}$$

If a quadratic distribution of the temperature along the radial direction is considered

$$T_2(r) = \frac{1881 - 3T_{max}}{2b^2} r^2 \left( \frac{5T_{max}}{2b} - \frac{967.5}{b} \right) r + T_{init} \quad (V.6)$$

The disk can be considered as a short cylinder with inner radius zero. In this case, conduction is the process through which the heat is transferred through the thickness of the cylinder (Incropera and DeWitt 1990).

The temperature distribution in this case has a logarithmic profile:

$$T_3(r) = \frac{T_{init} - T_{max}}{\ln\left(\frac{a}{b}\right)} \ln\left(\frac{r}{b}\right) + T_{max} \quad (V.7)$$

#### IV.2.3 Summary and conclusions

One case without thermal effects, three temperature distributions for the case with thermal effects:

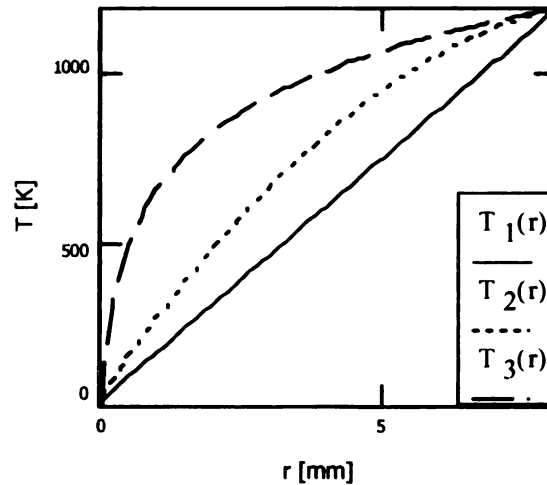
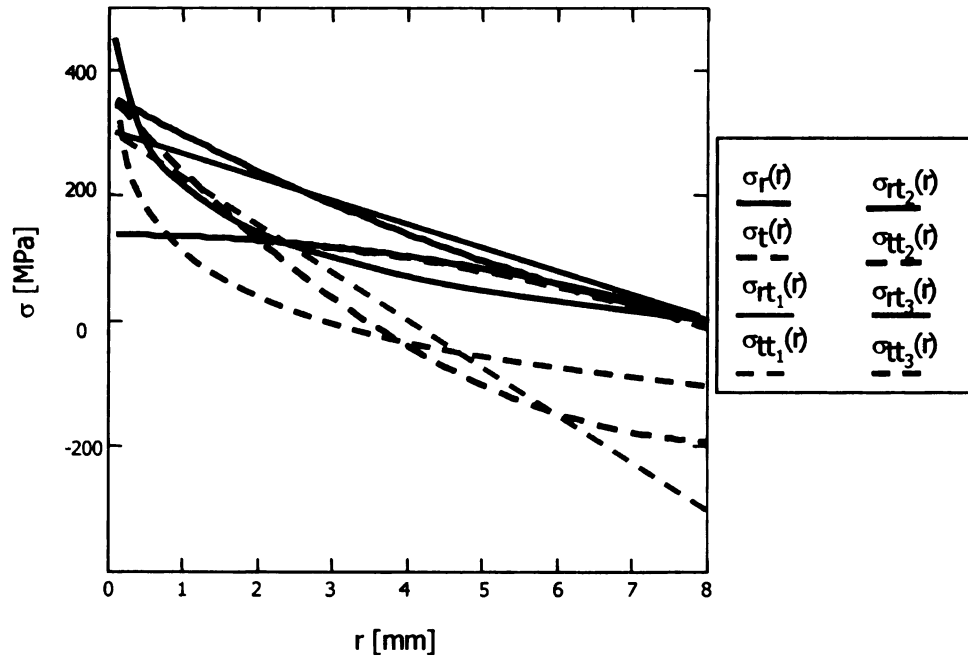


Figure IV.3: Temperature distribution in the three sub-cases: linear, quadratic and logarithmic.

The resultant stresses were compared with the adiabatic case and results plotted in Figure IV.4. The values of maximum stresses are displayed in Table IV.1.



**Figure IV.4:** Radial and tangential stresses with thermal effects along the radius of the disk (compressor/turbine rotor).

**Table IV.1:** Radial and tangential stresses in a rotating disc.

Stresses*	w/o temp.	with temp.		
		linear	quadratic	logarithmic
$\sigma_r(0)$	137.1	299.6	352.1	455.2
$\sigma_r(r)$	0	0	0	0
$\sigma_t(0)$	137.1	295.9	345.6	351.3
$\sigma_t(r)$	-12.2	-303.4	-193.1	-103.9

\* all results are displayed in MPa

The failure stress for silicon is  $\sigma_f \approx 7000$  MPa.

As noted for the adiabatic case, in the temperature influenced case the maximum stress is located at the center of the spinning disc. Maximum values are calculated for a logarithmic temperature distribution.

Thermal effect has an important impact over the stress state; but still for the considered loading conditions, the highest stress is less than 10% of the admissible stress for silicon.

The differences between the three temperature distributions are seen mostly for tangential stress at outer radius.

## **Chapter V**

### **DESIGN OF ULTRA-MICRO WAVE ROTORS ( $U_{\mu}WR$ )**

When trying to do MEMS experimental investigation, the first problem that arises is cost. Fabrication costs are high, and this is one of the reasons the research is progressing with a slow pace. Another reason is that diagnostics and measurement at microscale are difficult and often destructive. An alternate and viable solution to experiment is numerical investigation. Either using specialized in-house codes or the newly developed CFD commercial codes, the research process time is tremendously decreased. Numerical analyses are faster and more affordable than experimental ones, the later ones being necessary only after the numerical model has been thoroughly verified. In the field of shock waves simulated by available commercial codes, the literature is not too vast. Although the wave rotor is based on a relatively simple engineering idea, its simulation is rather difficult to achieve. Shock waves behave differently at microscale than at macro scale. For a given Mach number the resulting particle velocity is lower, but the pressure is higher (Brouillette 2003). The diffusive transport phenomena can no longer be neglected at micro scale, and viscous stresses at the boundaries tend to deform the shock wave front. Also, the heat conduction to the wall prevents the flow from remaining adiabatic. At a small scale the pressure rise across the shock increases with the decrease in the  $Re \cdot D/4L$  factor for a constant Mach number.

## **V.1 Gasdynamics of Compressible Flow**

As a first step in analyzing a wave rotor and its components, it is necessary to present some basic notions about a one-dimensional fluid flow; the gasdynamics and thermodynamics of it together with some knowledge on modeling a compressible fluid flow traveling through a channel. The next subchapter will describe some details of the simulation process, while the following subchapter will present the mathematical modeling of compressible flow.

## **V.2 Modeling of Unsteady Compressible Flow**

In subchapter I.2.2, some basic thermodynamic relations used in modeling unsteady compressible flows were presented. First, the numerical method used was the visual method of characteristics in the 1960s. Advances in computer technology brought a fresh start to numerical methods, so the Euler equations (Eqs. I.1 to I.3) were solved by different explicit and implicit codes, some written specifically for these applications (in-house codes), other created as software packages for solving any kind of fluid dynamics problem (Computational Fluid Dynamics commercial packages).

### **V.2.1 Explicit vs. Implicit**

Always, a first issue that comes in solving a fluid dynamics problem is what solver to use. The debate centered on explicit vs. implicit solutions has dated from the beginnings of numerical simulations, and it is still going on. There is no

clear criterion to decide which solution should be used for each problem; in fact some problems may provide similar results regardless of the solver used.

In general, explicit methods compute the next time step solution directly based on the known current time information. It is therefore necessary to keep the time step within the limit of physics in order to obtain accurate sequential solution in time. The implicit methods evaluate the solutions at two or more time space. In this way, one can improve the accuracy of the solution, in principle. There are many examples in the integration of an ordinary differential equation by using multi-steps.

The main problems that arise from using one or the other solution are numerical stability and numerical accuracy. For stability, the implicit solution method, which is more complex, allows for a larger time step than the explicit solution. But, since it is more complex, it requires more computational effort so even if the time step is larger, the computational time is also higher. For the explicit solution, it can be proved that the condition of accuracy is strong related to the stability condition. For the implicit solution, a factor of relaxation (damping) is introduced, which will make the solution more stable, thus making possible the increase in time step, but in the same time the results will be less accurate.

As an example, for a wave propagating through a tube, the implicit solution with high damping will capture only the steady-state results, while an explicit one permits the investigation of transient processes. To be able to use the implicit method in this case, a very small time step has to be used.

For non-viscous flows, where solution is conditionally stable, the explicit method works best.

As stated previously, the debate between an implicit and explicit solution has not been solved; and for the case of unsteady waves traveling through a channel/tube both methods have been used. Horrocks (Horrocks, Reizes et al. 1998), Pekkan (Pekkan and Nalim 2002) and Lee (Lee, Arslan et al. 2004), DeCourtye (DeCourtye, Sen et al. 1998) have used implicit methods; Welch (Welch and Chima 1993; Welch 1996; Welch 1997), Piechna (Piechna 1998; Piechna and Lisewski 1998; Piechna 1999), Larosiliere (Larosiliere and Mawid 1995), Eidemann (Eidemann, Grossmann et al. 1991) and Paxson (Paxson 1992; Paxson 1995) have used explicit, while Greendyke (Greendyke, Paxson et al. 2000) has used a combination of explicit and implicit model.



### V.3 Design Methodology

The first step in the calculation of the port timing is to decide on a corresponding wave pattern which, in turn, will generate a wave diagram. In the literature so far, there are several types of wave patterns for a four port wave rotor. Among these, two of them are presented next. The first one (Figure V.1), developed initially for a five port wave rotor by Cornell University was adapted to a four port wave rotor (Resler, Mocsari et al. 1993).

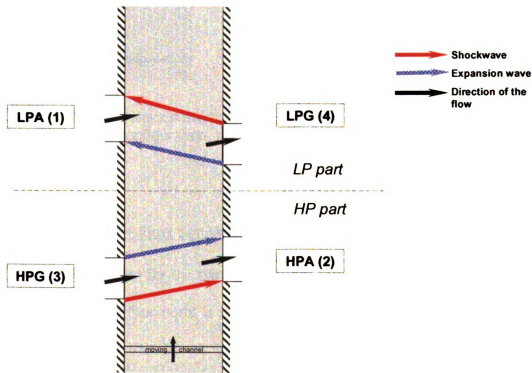


Figure V.1: Wave pattern for a four port wave rotor (adapted after Resler et al.).

NASA presented in 1997 (Welch, Jones et al. 1997) the wave patterns for a through-flow and a reverse-flow wave rotors (see Figure V.2)

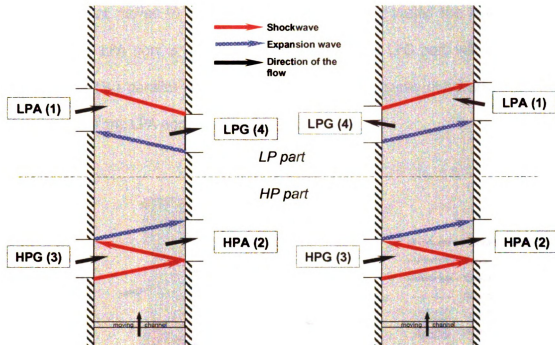


Figure V.2: NASA wave patterns for the four port wave rotor. Left – through-flow configuration, right – reverse-flow configuration.

### V.3.1 Through – Flow Solution

The solution chosen for the ultra-micro wave rotor, based on the thermodynamic conditions in the four ports is the following. The HPG port opens, generating a shock wave ( $S_1$ ) that travels to the end of the channel and reflects as shock wave  $S_2$  (Figure V.3). Immediately after  $S_1$  reaches the end of the channel, the HPA port opens. When  $S_2$  has traveled the channel lengths and reaches the HPG port, the port closes, generating an expansion wave ( $E_1$ ). When the head of  $E_1$  arrives to the HPA port, the port closes, and on the arrival of the tail of  $E_1$  to the right side, the LPG port opens. The opening of the LPG generates an expansion

wave ( $E_2$ ) that moves to the left side. When  $E_2$  has traveled the length of the channel, the LPA port is opening. The closing of the LPG port will generate a shock wave ( $S_3$ ) parallel with  $E_2$  and traveling in the same direction regulating the closure of the LPA port.

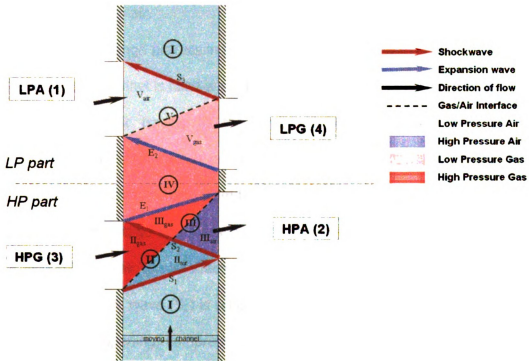


Figure V.3: Wave pattern for a four port through-flow wave rotor.

The horizontal axis represents the axis of the channel, while the vertical axis is the time (although this t-x diagram is more representative for an axial wave rotor, it can be applied for a preliminary design of a radial one – ignoring centrifugal forces effects, which will be discussed later). The presented wave pattern deals with an ideal situation, in which exhaust gases are fully scavenged to the turbine, while compressed air flows entirely to the combustion chamber.

The air/gas interface is just a temperature interface, since no pressure waves are crossing this interface; pressure is assumed to be constant all over a zone. Also, in generating the initial timing of the wave rotor, all fluids are assumed to be air and are treated as ideal gas. For convenience, initial high pressure, high temperature fluid will be referred to as gas, while initial low pressure, low temperature fluid as air.

The pressure exchange process in Figure V.3 is described as follows:

- zone I: the channel is filled with air coming from the compressor (fresh air)
- shock wave  $S_1$  travels to the right, realizing the first stage of the compression of the fresh air while expanding the high pressure, high temperature gases coming from the combustion chamber
- zone II: first stage compressed air and first stage expanded gas; zone is divided by the air/gas interface
- a second shock wave ( $S_2$ ) is reflected by the right end plate, just before the HPA port is opening, compressing the air further up the desired pressure in the combustion chamber
- zone III: end of air compression, the zone is connected to the HPA port; zone is divided by the air/gas interface
- expansion wave  $E_1$  further lowers the gases pressure and reducing the flow velocity in the channels to zero
- zone IV: the channels are fully expanded combustion gases

- expansion wave  $E_2$  which will fully reduce the gases pressure to the inlet pressure of the turbine
- zone V: a mixture of low pressure gases and low pressure air entering the channels; the air/gas interface is present throughout the zone
- a weak shock wave  $S_3$  generated by the closure of LPG port, which will return the channels to initial conditions and zone I

The gasdynamic cycle that allows for a prediction on the port timing uses the following background relations (Weber 1992; Anderson 2003):

- *shock wave relations:*

$$\Pi_s = \frac{p_2}{p_1} \quad (\text{VI.1})$$

$$\frac{T_2}{T_1} = \Pi_s \left( \frac{\frac{\gamma+1}{\gamma-1} + \Pi_s}{1 + \frac{\gamma+1}{\gamma-1} \cdot \Pi_s} \right) \quad (\text{VI.2})$$

$$w = a_1 \sqrt{\frac{\gamma+1}{2\gamma} (\Pi_s - 1) + 1} \quad (\text{VI.3})$$

$$u_p = \frac{a_1}{\gamma} (\Pi_s - 1) \sqrt{\frac{\frac{2\gamma}{\gamma+1}}{\Pi_s + \frac{\gamma-1}{\gamma+1}}} \quad (\text{VI.4})$$

where: 1 – conditions in front of the shock, 2 – conditions behind the shock,  $w$  – induced velocity of the flow in front of the shock,  $u_p$  – induced velocity of the flow behind the wave.

- *expansion wave relations.*

$$\frac{a_2}{a_1} = 1 \pm \frac{\gamma - 1}{2} \frac{u_2 - u_1}{a_1} \quad (\text{VI.5})$$

$$\frac{T_2}{T_1} = \left( \frac{a_2}{a_1} \right)^2 \quad (\text{VI.6})$$

$$\frac{p_2}{p_1} = \left( \frac{a_2}{a_1} \right)^{\frac{2\gamma}{\gamma-1}} \quad (\text{VI.7})$$

$$\begin{cases} u_{head} = a_1 \pm u_1 \\ u_{tail} = a_2 \pm u_2 \end{cases} \quad (\text{VI.8})$$

where: 1 – conditions in front of the wave, 2 – conditions behind the wave,  $u_{head}$  – velocity of the head of the wave,  $u_{tail}$  – velocity of the tail of the wave and the  $\pm$  sign represents the direction of the flow with respect to the direction of the wave.

- *general equations.*

$$a = \sqrt{\gamma R T} \quad (\text{VI.9})$$

- *total to static equations.*

$$\frac{T_0}{T} = 1 + \frac{\gamma - 1}{2} M^2 \quad (\text{VI.10})$$

$$\frac{p_0}{p} = \left( 1 + \frac{\gamma - 1}{2} M^2 \right)^{\frac{\gamma}{\gamma-1}} \quad (\text{VI.11})$$

The procedure assumed the stagnation properties in all ports are known. Since air is considered the only working gas in the model, in zones II, III and V, the

air/gas interface is differentiating only in temperature the two gases. The pressures of air and exhaust gas are the same as no pressure wave comes between the two fluids.

*I – II*

Assumptions:  $u_I = 0$ ,  $p_I = p_1 = p_{01}$ ,  $T_I = T_1 = T_{01}$ ,  $u_{II} = u_3 = 0$ ,  $p_{II} = p_3 = p_{03}$ ,

$$T_{II} = T_3 = T_{03}$$

From relation VI.1, setting  $p_2 = p_3$  and  $p_1 = p_I$  it results

$$\Pi_{s1} = \frac{p_3}{p_1} \quad (\text{VI.12})$$

The velocity of the shock is defined as the velocity of the flow in front of the shock, if the flow was initially at rest.

$$w_{s1} = a_1 \sqrt{\frac{\gamma+1}{2\gamma} (\Pi_{s1} - 1) + 1} \quad (\text{VI.13})$$

where  $a_1$  is the speed of sound in region 1 (LPA port) and defined by Eq. VI.9.

The time it takes the wave to travel the length of the channel is equal to

$$t_{s1} = \frac{L}{w_{s1}} \quad (\text{VI.14})$$

The time  $t_{s1}$  will define the opening of the HPA port and will call  $t_{HPAopen}$ .  $L$  is the length of the channel.

The induced velocity of the flow behind the shock is the velocity of the flow in zone II.

$$u_{II} = u_{p1} - \frac{a_1}{\gamma} (\Pi_{s1} - 1) \sqrt{\frac{\frac{2\gamma}{\gamma+1}}{\Pi_{s1} + \frac{\gamma-1}{\gamma+1}}} \quad (VI.15)$$

The air temperature in zone II can be calculated using Eq. VI.2.

$$T_{IIair} = T_I \Pi_{s1} \frac{\frac{\gamma+1}{\gamma-1} + \Pi_{s1}}{1 + \frac{\gamma+1}{\gamma-1} \Pi_{s1}} \quad (VI.16)$$

While the gas total temperature in zone II is equal to the gas total temperature in HPG port.

$$T_{0IIgas} = T_{03} \quad (VI.17)$$

The Mach number of zone II<sub>gas</sub> is defined as

$$M_{IIgas} = \frac{u_{II}}{a_{IIgas}} = \frac{u_{II}}{\sqrt{\gamma R T_{IIgas}}} \quad (VI.18)$$

Applying Eqs. VI.18 and VI.10 for zone II<sub>gas</sub> the value of the static temperature can be obtained

$$T_{IIgas} = T_{0IIgas} - \frac{\gamma-1}{2} \frac{u_{II}^2}{\gamma R} \quad (VI.19)$$

Using the definition of Mach number and speed of sound at zone II<sub>air</sub> the rest of the properties of the air can be calculated.

$$T_{0IIair} = T_{IIair} \left( 1 + \frac{\gamma-1}{2} M_{IIair}^2 \right) \quad (VI.20)$$

$$\rho_{IIair} = \rho_{0IIair} \left( 1 + \frac{\gamma-1}{2} M_{IIair}^2 \right)^{\frac{\gamma-1}{\gamma}} \quad (VI.21)$$



## II – III

Assumption:  $p_{0III} = p_{02}$ .

Reflection of the primary shock wave will increase the pressure of the fresh air further, since it is known that one shock cannot raise the pressure of the driven gas higher than the pressure of the driving gas. As seen in previous paragraph these two shock waves are regulating the opening and closing of the HPA and HPG ports.

From relation VI.1, setting  $p_1 = p_3$  it results the pressure ratio across the second shock wave.

$$\Pi_{s2} = \frac{p_2}{p_3} \quad (\text{VI.22})$$

To find the static pressure of HPA port ( $p_2$ ), the following system of equation needs to be solved:

$$\begin{cases} \frac{p_{02}}{p_2} = \left(1 + \frac{\gamma-1}{2} M_2^2\right)^{\frac{\gamma}{\gamma-1}} \\ \frac{T_{02}}{T_2} = 1 + \frac{\gamma-1}{2} M_2^2 \\ M_2 = \frac{u_2}{a_2} = \frac{u_2}{\sqrt{\gamma R T_2}} \end{cases} \quad (\text{VI.23})$$

Simplifying the previous system of equations using also Eqs. VI.4, VI.9, VI.22 the following result is obtained:

$$\sqrt{\gamma R T_{02} \frac{2}{\gamma-1} \frac{A-1}{A}} = u_{p1} - \sqrt{\frac{2R T_3 p_3}{p_{02}(\gamma+1)A^{\frac{\gamma-1}{\gamma}} + (\gamma-1)p_3}} \left( \frac{p_{02} A^{\frac{\gamma-1}{\gamma}}}{p_3} - 1 \right) \quad (\text{VI.24})$$

where the unknown is  $A = 1 + \frac{\gamma-1}{2} M_2^2$ .

Equation VI.24 is best solved numerically. Calculation of  $M_2$  yields to solutions for the other unknowns ( $p_2$ ,  $T_2$ ,  $u_2$ ,  $u_{p2}$ ).

The velocity of the second shock wave as defined by Eq. VI.3 is

$$w_{s2} = a_3 \sqrt{\frac{\gamma+1}{2\gamma} (\Pi_{s2} - 1) + 1} \quad (\text{VI.25})$$

The time necessary for the second shock to travel to the left side of the wave rotor is called  $t_{s2}$  and is defined by the definition of velocity.

$$t_{s2} = \frac{L}{w_{s2}} \quad (\text{VI.26})$$

Time  $t_{s2}$  is the delay between the opening of HPA port and closing of HPG port.

The opening of HPG is set to be 0s ( $t_{HPGopen} = 0$ ) and the closing is

$$t_{HPGclose} = t_{s1} + t_{s2} \quad (\text{VI.27})$$

The time while the a port is open is defined as follows.

$$t_{<port>} = t_{<port>close} - t_{<port>open} \quad (\text{VI.28})$$

Both air and gas temperatures in zone III are defined by Eq. VI.2.

$$T_{IIIair} = T_{IIair} \Pi_{s2} \left( \frac{\frac{\gamma+1}{\gamma-1} + \Pi_{s2}}{1 + \frac{\gamma+1}{\gamma-1} \Pi_{s2}} \right) \quad (\text{VI.29})$$

$$T_{IIIgas} = T_{IIgas} \Pi_{S2} \left( \frac{\frac{\gamma+1}{\gamma-1} + \Pi_{S2}}{1 + \frac{\gamma+1}{\gamma-1} \Pi_{S2}} \right) \quad (VI.30)$$

Pressure in the zone III is the same for air and gas.

The velocity of the flow induced by the shock wave  $S_2$  is  $u_{p2}$  and is computed with Eq. VI.4 and is oriented in the direction of the shock travel.

$$u_{p2} = \frac{a_3}{\gamma} (\Pi_{S2} - 1) \sqrt{\frac{\frac{2\gamma}{\gamma+1}}{\Pi_{S2} + \frac{\gamma-1}{\gamma+1}}} \quad (VI.31)$$

The velocity at the exit of the channel to the HPA port  $u_2$  is given by the sum of velocity in zone II (from Eq. VI.15) and induced velocity from second shock wave,  $u_{p2}$ .

$$u_2 = u_{p1} - u_{p2} \quad (VI.32)$$

### III – IV

Assumptions:  $u_{IV} = 0$ ,  $u_{III} = u_2$ .

Velocity of the expansion wave  $E_1$  is defined by the velocities of the head and tail of the expansion wave (Eq. VI.8). Since high pressure is needed in the HPA port and the pressure is lower towards moving to the tail of the shock wave, the head of the shock reaching the right side of the wave rotor will regulate the closing of the HPA port. To avoid the reflection of the expansion wave and lowering the

pressure in the channels even further, the tail of the expansion wave will determine the opening of the LPG port.

From Eq. VI.8,

$$\begin{cases} u_{head1} = a_{III} + u_{III} \\ u_{tail1} = a_{IV} + u_{IV} \end{cases} \quad (VI.33)$$

$a_{IV}$  can be found out using Eq. VI.5.

$$\frac{a_{IV}}{a_{III}} = 1 + \frac{\gamma - 1}{2} \frac{u_{IV} - u_{III}}{a_{III}} \quad (VI.34)$$

The times required by the expansion wave's head and tail to reach the other end of the channel are

$$\begin{cases} t_{head1} = \frac{L}{u_{head1}} \\ t_{tail1} = \frac{L}{u_{tail1}} \end{cases} \quad (VI.35)$$

The closing of HPA port is defined as

$$t_{HPAclose} = t_{HPGclose} + t_{head1} \quad (VI.36)$$

While the opening of LPG port is

$$t_{LPGopen} = t_{HPGclose} + t_{tail1} \quad (VI.37)$$

The pressure in zone IV is according to Eq. VI.7.

$$\frac{p_{IV}}{p_{III}} = \left( \frac{a_{IV}}{a_{III}} \right)^{\frac{2\gamma}{\gamma-1}} \quad (VI.38)$$

*IV – V*

The traveling of the second expansion ( $E_2$ ) wave will influence the opening of LPA port. Since the lowest pressure in the channel is needed for maximum inflow

of fresh air, the arrival of the tail of the second expansion wave will determine the opening of the LPA port.

Applying Eq. VI.5 for  $a_{IV}$  and  $a_V$  will result in finding the value of  $a_V$ .

$$\frac{a_{Vgas}}{a_{IV}} = 1 + \frac{\gamma - 1}{2} \frac{u_{IV} - u_{Vgas}}{a_{IV}} \quad (VI.39)$$

To find  $a_{Vgas}$  the value of  $T_{Vgas}$  is needed. It is assumed that  $T_{Vgas} = T_4$  and

$T_{0Vgas} = T_{04}$ . Applying Eq. VI.10

$$\frac{T_{0Vgas}}{T_{Vgas}} = 1 + \frac{\gamma - 1}{2} M_{Vgas}^2 = 1 + \frac{\gamma - 1}{2} \frac{u_{Vgas}^2}{\gamma R T_{Vgas}} \quad (VI.40)$$

From Eqs. VI.39 and VI.40,

$$T_{Vgas} = \frac{\gamma R T_{0Vgas} (\gamma - 1) + 2a_{IV}^2}{\gamma R (\gamma + 1)} - \frac{4a_{IV}^2 (\gamma - 1)}{\gamma R (\gamma + 1)^2} + \frac{2\sqrt{2\gamma R (\gamma - 1)(2\gamma^3 R^2 T_{0Vgas} + 2\gamma^2 R^2 T_{0Vgas} - 4\gamma R a_{IV}^2)}}{\gamma^2 R^2 (\gamma + 1)^2} \quad (VI.41)$$

thus

$$u_{Vgas} = \sqrt{\frac{2\gamma R}{\gamma - 1} (T_{0Vgas} - T_{Vgas})} \quad (VI.42)$$

From Eq. VI.8,  $u_{head2}$  and  $u_{tail2}$  are

$$\begin{cases} u_{head2} = a_{IV} - u_{IV} \\ u_{tail2} = a_{Vgas} - u_{Vgas} \end{cases} \quad (VI.43)$$

both of them traveling in the opposite direction of the flow.

The corresponding durations the waves travel are

$$\begin{cases} t_{head2} = \frac{L}{U_{head2}} \\ t_{tail2} = \frac{L}{U_{tail2}} \end{cases} \quad (VI.44)$$

Opening time of LPA port is the sum of opening time of LPG port and  $t_{tail2}$ .

$$t_{LPAopen} = t_{LPGopen} + t_{tail2} \quad (VI.45)$$

*V – I*

Shock wave  $S_3$  is generated by the closing of the LPG port and its arrival at the low pressure air side will determine the closing of LPA port. From Eq. VI.1, setting  $p_2 = p_1$  and  $p_1 = p_4$  it results

$$\Pi_{S3} = \frac{p_1}{p_4} \quad (VI.46)$$

The velocity of the shock is defined by Eq. VI.3

$$w_{S3} = a_{Vair} \sqrt{\frac{\gamma+1}{2\gamma} (\Pi_{S3} - 1) + 1} \quad (VI.47)$$

where  $a_{Vair}$  is the speed of sound in region 1 (LPA port) and defined by Eq. (VI.9).

The time it takes the wave to travel the length of the channel is equal to

$$t_{S3} = \frac{L}{w_{S3}} \quad (VI.48)$$

It results that

$$t_{LPAclose} = t_{LPGclose} + t_{S3} \quad (VI.49)$$

The missing information, closing time of LPG port ( $t_{LPGclose}$ ) can be revealed by an overall mass balance over the entire port system.

Taking the velocities in the absolute values, thus considering flows in HPG and LPA ports as inflows, while HPA and LPG ports providing outflows, the following relation can be written.

$$\dot{m}_{HPG} + \dot{m}_{LPA} = \dot{m}_{HPA} + \dot{m}_{LPG} \quad (VI.50)$$

Knowing

$$\dot{m} = \rho u A \quad (VI.51)$$

where  $A$  is the cross-sectional area, defined as

$$A = H W = H t v \quad (VI.52)$$

$H$  is the height of the port,  $W$  is the width of the port, which can be computed as the time while the port is open,  $t$ , multiplied by the tangential velocity of the rotor,  $v$ .

Also, from the equation of state of an ideal gas (Moran and Shapiro 2004)

$$\rho = \frac{p}{R T} \quad (VI.53)$$

From Eqs. VI.50-VI.53

$$\frac{p_{HPG}}{T_{HPG}} u_{HPG} t_{HPG} + \frac{p_{LPA}}{T_{LPA}} u_{LPA} t_{LPA} = \frac{p_{HPA}}{T_{HPA}} u_{HPA} t_{HPA} + \frac{p_{LPG}}{T_{LPG}} u_{LPG} t_{LPG} \quad (VI.54)$$

The velocities in the LPA and LPG ports are assumed to be the same. Applying Eq. VI.28 for LPA and LPG ports and Eqs. VI.45 and VI.49, the time while LPA is open,  $t_{LPA}$ , can be deduced as function as  $t_{LPG}$ .

$$t_{LPA} = t_{LPG} + t_{S3} - t_{tail/2} \quad (VI.55)$$

Introducing Eq. VI.55 into Eq. VI.54, only one value remains unknown,  $t_{LPG}$ . Once this equation is solved, all the times of port opening and closing are known, so a preliminary porting solution is generated.

The results generated by the previous analysis were compared with the numerical ones obtained using the 1D code. Results are presented in a graphic format in Figure V.4.

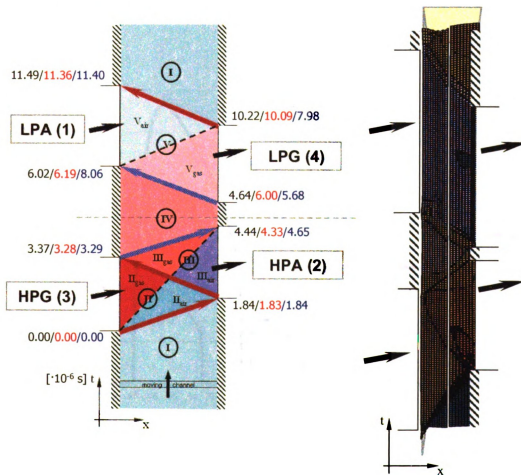


Figure V.4: Comparison between analytical results and numerical results for an initial port prediction of a through-flow wave rotor (first number is analytically obtained, the second one – numerically).



For an optimum port timing calculation, a feedback loop was created between the two models, thus reducing the error in continuity equation from 6.4% to 2%. The mass flow rate graph function of time is presented in Figure V.5. Flow rate through all the ports is positive, meaning that the fluid always travels to the right (positive x-axis). Thus, for the left boundary the positive flow rate means inflow to the channel, while negative means outflow from the channel. The reverse is valid for the right boundary.

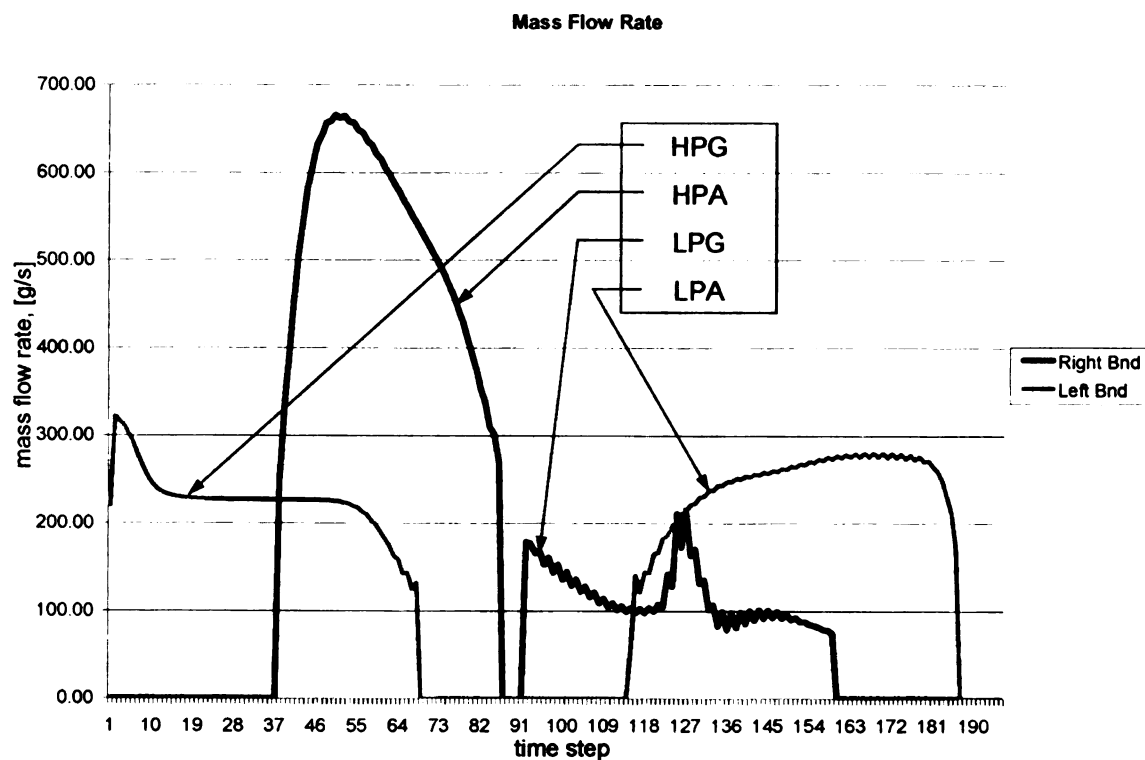


Figure V.5: Mass flow rate through the boundaries of a wave rotor channel in through-flow configuration, [kg/s].

### V.3.2 Reverse – Flow Solution

Next, the reverse-flow configuration is presented. The wave pattern is identical with the through-flow configuration for the high pressure part, while the low pressure part pattern is mirrored (Figure V.6).

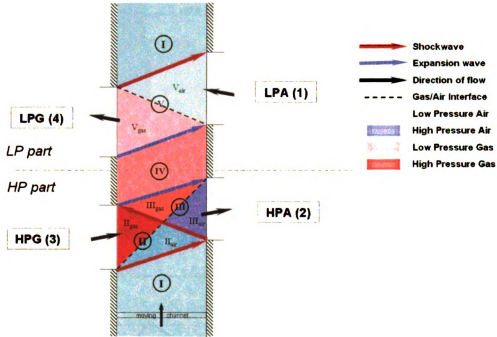


Figure V.6: Wave pattern for a four port reverse-flow wave rotor.

The analytical solution follows the same steps as for through-flow model. Again, the results from the theoretical analysis and the numerical ones were compared, being displayed in Figure V.7. The mass flow rate graph is shown in Figure V.8, where the reverse-flow effect can be seen. On the high pressure part, on both boundaries, the flow rate is positive, which means for the left boundary flow goes into the channel. On the low pressure side, both flow rates are negative; meaning that for the left boundary, fluid leaves the channel.

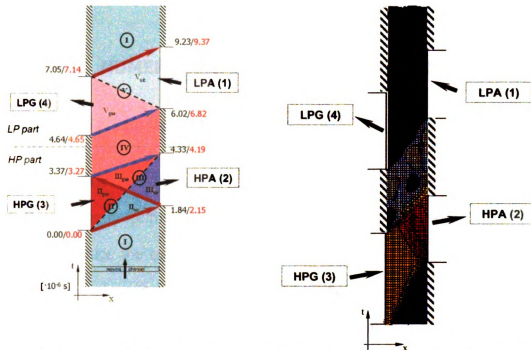


Figure V.7: Comparison between analytical results and numerical results for an initial port prediction of a reverse-flow wave rotor (first number is analytically obtained, the second one – numerically).

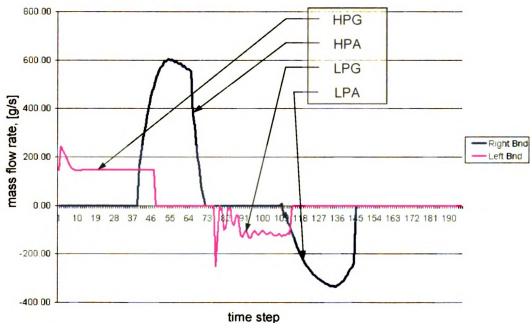


Figure V.8: Mass flow rate through the boundaries of a wave rotor channel in reverse-flow configuration, [kg/s].

## Chapter VI

### NUMERICAL SIMULATIONS OF U<sub>μ</sub>WR

#### VI.1 Setting up GAMBIT

GAMBIT 2.1 was used as a pre-processor for creating the geometry, mesh, and domains necessary for the CFD software. The 3D objects were converted into 2D models to reduce the computational load. The axial wave rotor channels were designed as a sequence of faces, using the unfolded view method, which allows 3D objects to be projected onto 2D surfaces, described in the previous chapter.

Figure VI.1 illustrates the geometry used for creating the mesh of the axial wave rotor in through-flow and reverse-flow configurations. The edge boundaries comprise two *pressure inlets* and two *pressure outlets* for the ports (ducts), as well as two sliding interfaces between stationary walls and moving channels.

The mesh was created using standard, quad elements placed in *map* and *pave* type distributions. For simple geometries like the one of a wave rotor, the quad elements are suitable to use and they decrease the computational time. The *pave* distribution was used to accommodate the transition from finer mesh along the interface to a coarser mesh towards the end of the ports (Figure VI.2). In the case of the axial wave rotor model, the solid walls were modeled as adiabatic ones.

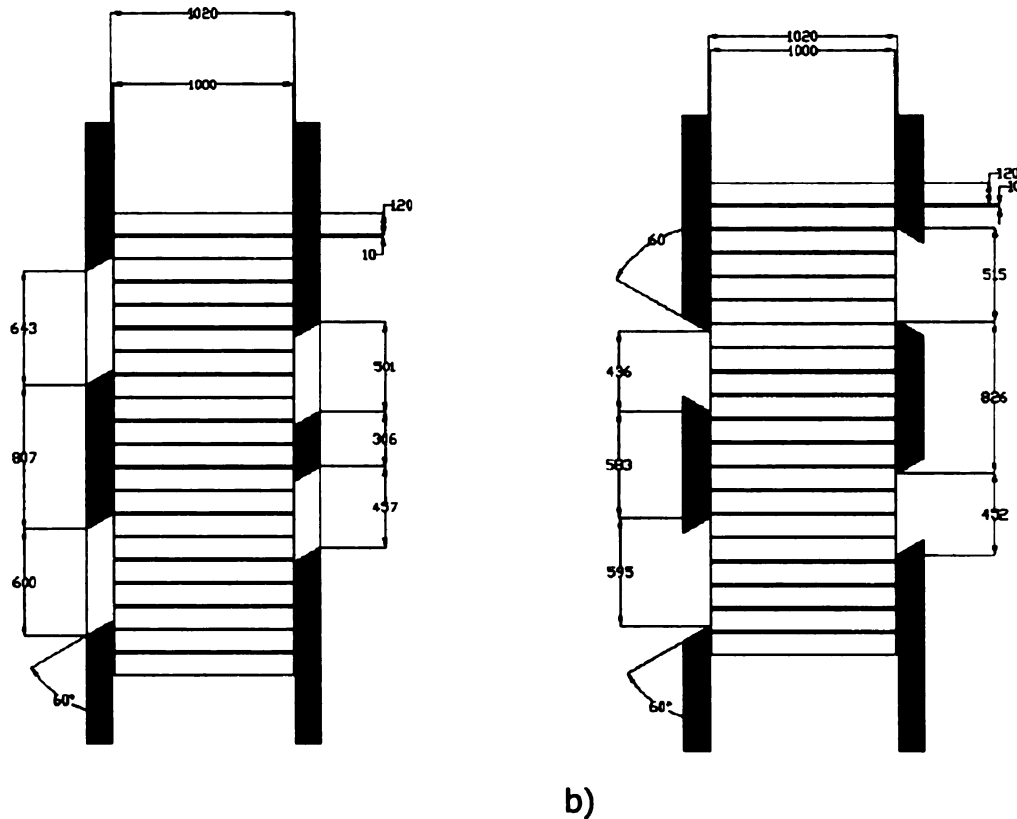


Figure VI.1: Axial wave rotor in 2D developed view: a) through-flow configuration; b) reverse-flow configuration (values in  $\mu\text{m}$ ).

The dynamic aspect was modeled as follows: the channels are sliding between stationary ports with *interface pairs* created between end of channels and ports (Figure VI.2). The pair of interfaces works only if at least one of the interfaces is made out of a single edge. If multiple edges are used for both interfaces in the pair, then the property transfer is not realized between the surfaces in contact. The situation of Figure VI.2-a is acceptable, but for the one in Figure VI.2b a small area was added to the end of the channels, which will transform all the edges from the end of the channel into one. This is actually a more accurate simulation, because this will account for the leakage between the rotor and the

casing (which contains the ports). Another way of creating the interface is to join the two ports together by a small slit (Figure VI.2-c). To be noticed that the slits added to the interfaces are 100 times narrower than the length of the channel. They might be created even smaller with the purpose of realistic modeling; but in this case, the mesh has to be finer, which in turn will generate slower results.

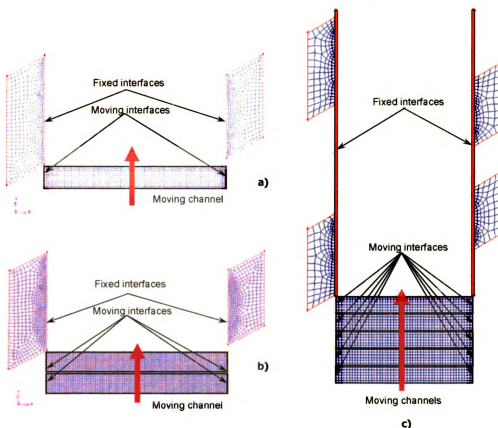


Figure VI.2: Mesh and interfaces setup for 2D axial wave rotor investigations: a) single port – multiple channel interface, b) single port – multiple channel interface with additional gap, c) multiple port – multiple channel interface with gap.

The axial wave rotor mesh adopted here is comprised of 9,406 nodes and 7,836 elements. In the case of the radial wave rotor, the transformation of the 3D object into a 2D model was simpler. A horizontal cross-section of the rotor and

ports was used to create the model. An example of a rotor is illustrated in Figure VI.3. In order to decrease the computational time, a reduced model with a single cycle per revolution was utilized for pin-pointing the final design. The reduced model is basically a quarter of the full model presented in Figure VI.3 with one set of ports and approximately 30 rotating channels. The design schematic can be seen in Figure VI.4.

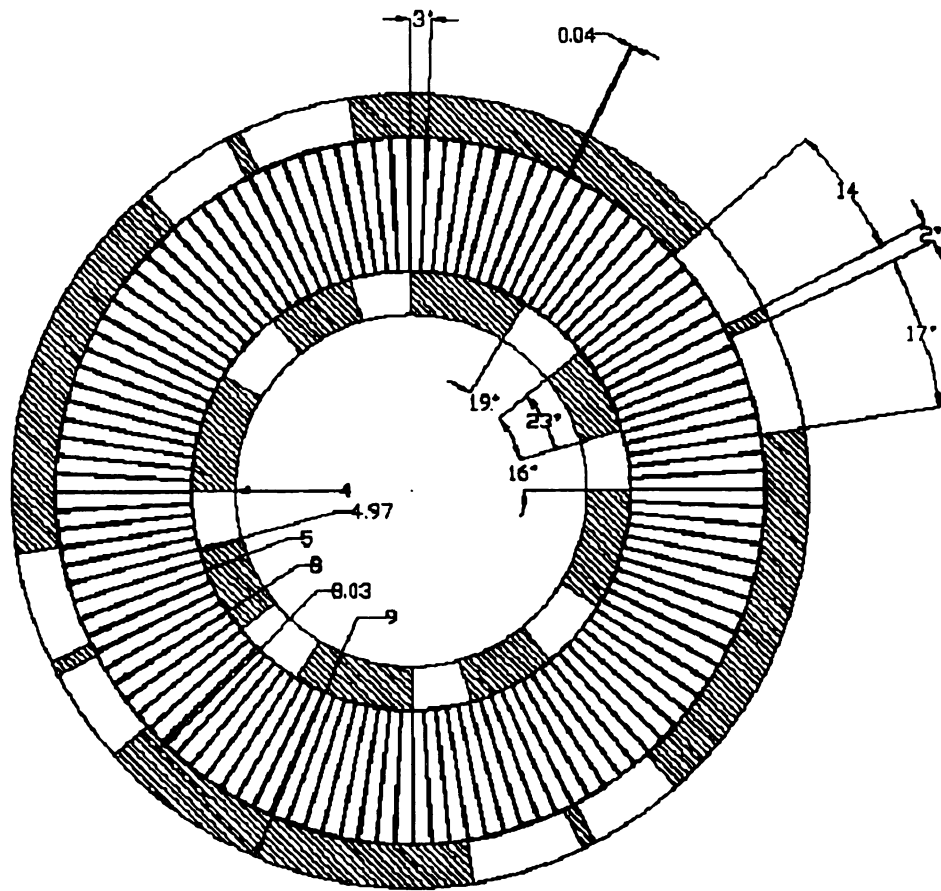


Figure VI.3: Radial wave rotor cross-sectional view [dimensions in mm].

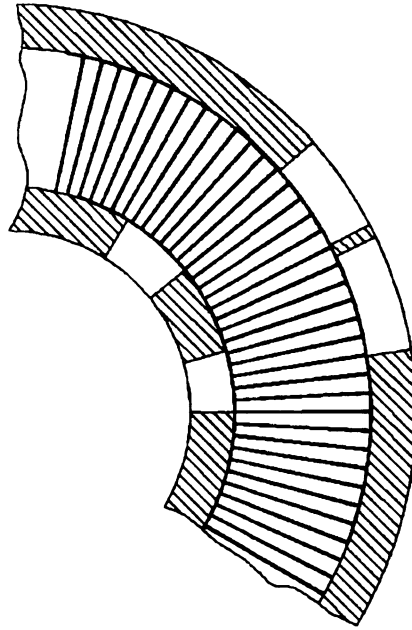


Figure VI.4: Radial wave rotor cross-sectional view – reduced model.

Following a grid sensitivity study with refinements from 10,000 to approximately 170,000 elements, the final design was set to 38,101 elements and 52,519 nodes for the full model and 10,210 elements and 12,884 nodes for the reduced model. The contact zones between fluid region and solid region (channels' interior and walls) have been defined as *coupled walls*. Section VII.3 will present more details about heat transfer modeling.

An example of mesh for a through-flow radial wave rotor, reduced model, is presented in Figure VI.5.



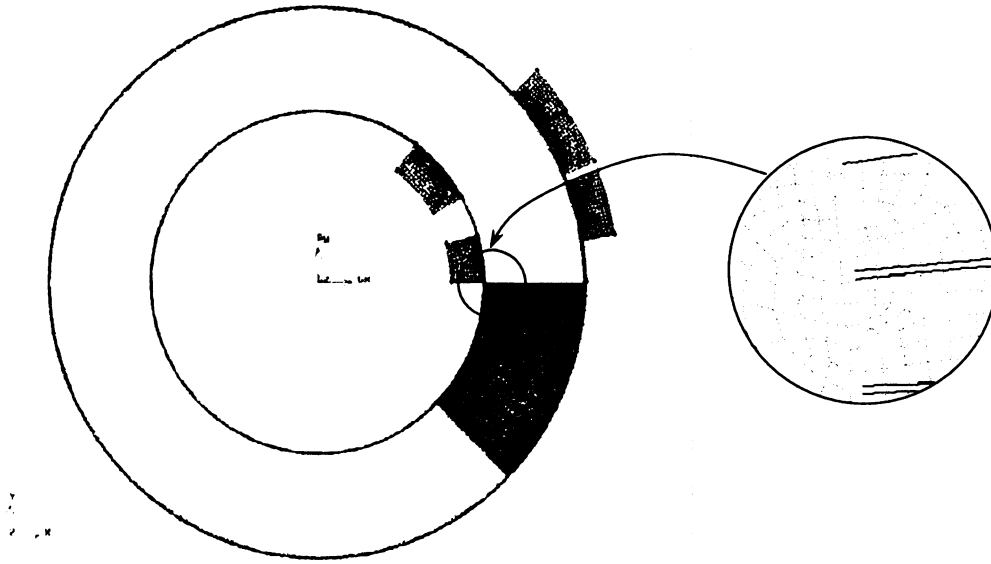


Figure VI.5: Radial waver rotor in a through flow (TF) configuration: reduced model and zoom in of the mesh.

## **VI.2      Setting up FLUENT**

For simulating the behavior of the flow through an ultra-micro wave rotor, the commercial CFD package, FLUENT 6.1 was used. An extensive study of using modern CFD commercial packages to simulate fluid flows in various conditions, either laminar or turbulent, steady or unsteady was done by Kochevsky in 2004. His conclusions were that CFD packages, including Fluent, are capable of simulating accurately unsteady flow behavior (Kochevsky 2004). The following paragraph will describe the solver settings as well as some boundary conditions and convergence criteria used.

The fluid was considered as compressible ideal gas, having constant specific heat and constant thermal conductivity, while the viscosity varied with temperature. Since the difference in gas constant for air and exhaust gases is minor, for modeling simplification only one gas was considered as working fluid – air.

The solid regions were considered to be silicon made, having constant specific heat and temperature dependent thermal conductivity. The properties for the material considered are presented in Annex 1.

The ports were modeled as pressure inlets and outlets, with a fixed value set in the boundary condition. Once the model was started, the *Patch* option was used to increase dramatically the pressure and temperature in the HPG port, allowing the simulation of the unsteady flow phenomena. The inlet and outlet pressure boundary conditions used for modeling inlet and outlet flow to limit the mesh space is a well know technique even for the free flow around objects. Hunt and

his group at the University at Canterbury have used it for modeling the flow around a plane wing (Hunt, Rudge et al. 2002).

A *double-precision solver* was chosen due to the nature of the problem. Since the problem is unsteady, the residuals of the Euler equations will tend not to be in the same order of magnitude. The double-precision solver allows for a twelve order of magnitude drop of the residuals. The *coupled solver* allows for both implicit and explicit methods to be used, solving the governing equations of continuity, momentum, and energy simultaneously as a set of equations. If the coupled solver is used together with the energy equation, the viscous terms (artificial viscosity) are added to the later automatically. The stability of the solution is given by the CFL criterion. Let  $g$  be a flow variable. Its value after at a time  $t+\Delta t$ , function of previous time step,  $t$ , can be described in a basic Taylor series.

$$g(t + \Delta t) = g(t) + \left( \frac{\partial g}{\partial t} \right)_{avg} \Delta t + \dots \quad (\text{VII.1})$$

But  $\Delta t$  cannot be arbitrary. It has to be less or equal than some maximum value, estimated by a stability analysis performed on a set of linear equations in order for the solution to converge. The CFL criterion says that  $\Delta t$  must be less than equal to the time required for a sound wave to travel between two adjacent grid points (Courant, Friedrichs et al. 1928; Courant, Friedrichs et al. 1967).

But  $\Delta t / \Delta x$  (distance between adjacent grid points) is proportional to the Courant number (or CFL number). Because of this coupling, reducing the grid size will

increase the solving time, unless the Courant number is increased, up to the stability limit. For an explicit solution it is set to 1 and can go up to 2, while for an implicit solution, it is set to 5 and can go up to 100 (Fluent 2003). For the coupled solver, this is the main stability control parameter.

When using *laminar flow conditions*, the viscosity is modeled as a function of temperature, based on the *Sutherland model* (Brillouin 1938; Kim and Chair 2002)

$$\mu = \mu_{ref} \left( \frac{T}{T_0} \right)^{1.5} \frac{T_{ref} + S}{T + S} \quad (\text{VII.2})$$

where  $\mu_{ref} = 1.789 \cdot 10^{-5}$  kg/ms is the reference viscosity,  $T_{ref} = 273.11$  K is the reference temperature and  $S = 110.56$  K is the effective temperature in the three coefficients Sutherland law (Sutherland 1893).

The solution controls are *Courant number* (which is automatically adjusted for convergence of solution) and type of accuracy determined by the solution scheme. The *first order upwind scheme* has been used, which is a first order accuracy solution, meaning that the quantities at faces are determined by assuming constant values through out the cell, calculated in the center and averaged over the cell. This scheme is useful and accurate when the flow is aligned with the grid. Otherwise, first order convective discretization increases the numerical error (due to diffusion). The same upwind scheme was used by Liu

and his team when modeling a 4mm diameter shock tube used for delivering a powder vaccine (Liu, Truong et al. 2004).

Convergence is attained once each residual of the continuity equation, energy equation, and flow velocities dropped at least three orders of magnitude. The residuals were monitored, allowing the computation to advance to the next time step once the convergence criterion was met.

Results show that the flow is well into the continuous and laminar region, thus determining an accurate simulation. The Reynolds numbers vary between 10 and 1000, while the Knudsen number stays lower than  $10^{-4}$ .

As discussed in Chapter VI, the debate over the explicit and implicit solver has arguments for both sides. For solving the numerical model of a wave rotor, a coupled implicit solver was used, flow being modeled as laminar viscous, but not before doing some investigations on proper type of solver to be used. Thus, it was concluded that between laminar viscous and inviscid flow as well as between implicit and explicit solver, the difference is not significant.

In the Lax scheme that FLUENT uses when the coupled option is used, a term called "artificial viscosity" appears when solving an inviscid flow model. This artificial viscosity behaves just like the viscous term in the Navier-Stokes equation. Assuming two properties  $f$  and  $g$  functions of time and space ( $t, x$ ), related through a simple partial differential equation (Eq. VII.3)

$$\frac{\partial g}{\partial t} = \frac{\partial f}{\partial x} \quad (\text{VII.3})$$

According to Lax, the time derivative is based on an average value of  $g$  between points  $(i - 1)$  and  $(i + 1)$

$$\left(\frac{\partial g}{\partial t}\right)_i^k = \frac{g_i^{k+1} - 0.5(g_{i+1}^k + g_{i-1}^k)}{\Delta t} \quad (\text{VII.4})$$

After some mathematical operations with the two equations,

$$\frac{\partial g}{\partial t} = \frac{\partial f}{\partial x} + \frac{(\Delta x)^2}{2\Delta t} \frac{\partial^2 g}{\partial x^2} \quad (\text{VII.5})$$

Equations VII.3 and VII.5 are different. By applying Lax's finite-difference procedure (Lax 1954) to Eq. VII.3, a difference equation was obtained; and by applying the definition of the derivative to this equation, the partial differential equation (VII.5) was obtained. This equation contains the extra, second order term  $\partial^2 g / \partial x^2$  multiplied by  $(\Delta x)^2 / 2\Delta t$ . This coefficient is called artificial viscosity and is a consequence of the mathematical procedure, not a physical term. This term is specifically added to the equation to account for a more realistic simulation (Anderson 2003).

When examining the results obtained with the CFD code, it can be seen that the difference between artificial viscosity and laminar viscosity in the wave rotor case is negligible. The artificial (numerical) viscosity is triggered by the pressure gradients, while the real (physical) viscosity is activated by the velocity gradients. Since the velocity is induced by the force of the shock, which is the pressure ratio, it can be clearly seen why the two viscosities generate the same effect.

Figure VI.6 presents the pressure and temperature distribution in the cases of inviscid and laminar viscous flows.

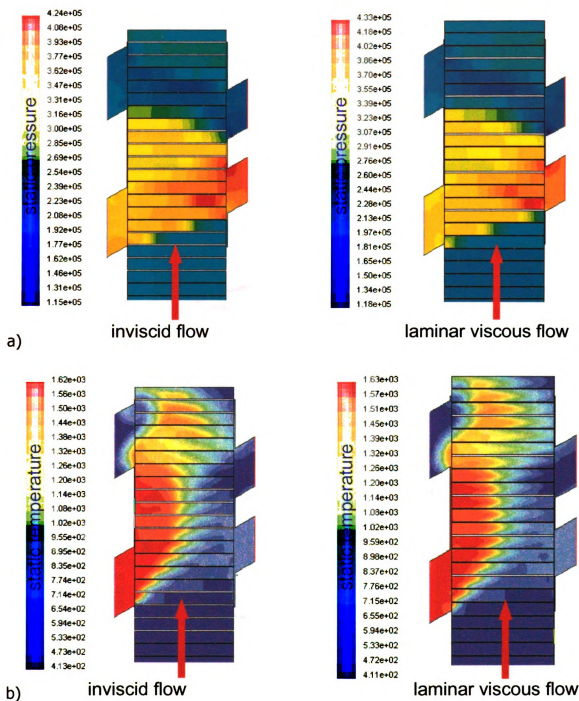


Figure II.1: 2D simulation of axial wave rotor: a) pressure distribution, b) temperature distribution.

When comparing the explicit and implicit solvers, the numerical model proved to be robust enough, thus indifferent to the type of solver. Since the time step was

small enough for both explicit and implicit solution to converge, the two solutions provided almost identical results. The time steps varied from  $1e-9$  to  $2.5e-8$  seconds. Figure II. presents the distribution of pressure and temperature for a model with laminar viscous flow solved with an explicit and an implicit solver.

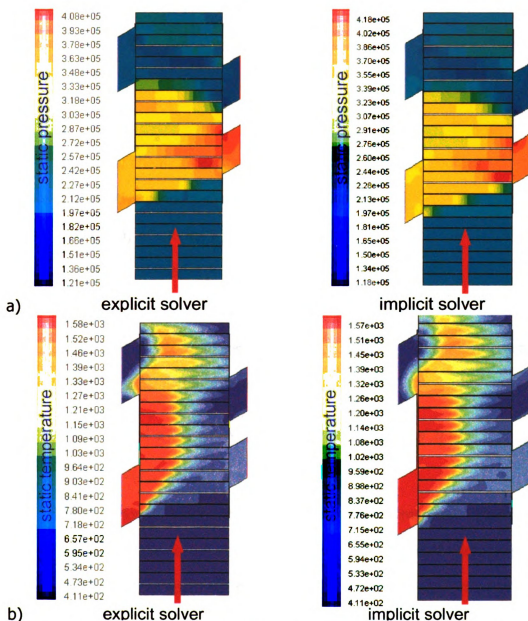


Figure II.7: 2D simulation of axial wave rotor: a) pressure distribution, b) temperature distribution.



### VI.3 Heat Transfer Simulations

When FLUENT is used to solve the heat conjugate problem, the energy equation (I.3) becomes

$$\begin{aligned} \frac{\partial}{\partial t} \left( \rho \left( e + \frac{u^2}{2} \right) \right) + \nabla \left( \rho u \left( e + \frac{u^2}{2} \right) \right) + \nabla ( \rho u ) - \rho f_x u - S_h - \\ - \nabla \left( k_{eff} \cdot \nabla T - \sum_j h_j \bar{J}_j + \bar{\sigma}_{eff} \cdot \bar{u} \right) = 0 \end{aligned} \quad (VII.6)$$

where

- $S_h$ : heat of chemical reaction and other volumetric heat sources
- $k_{eff}$ : effective conductivity
- $h_j$ : enthalpy of species  $j$
- $J_j$ : diffusion of species  $j$
- $\bar{\sigma}_{eff} \cdot \bar{u}$ : viscous dissipation

Since the simulation accounts for only one species and no chemical reactions, Eq. VII.6 can be simplified as follows:

$$\begin{aligned} \frac{\partial}{\partial t} \left( \rho \left( e + \frac{u^2}{2} \right) \right) + \nabla \left( \rho u \left( e + \frac{u^2}{2} \right) \right) + \nabla ( \rho u ) - \rho f_x u - \\ - \nabla \left( k_{eff} \cdot \nabla T - h \bar{J} + \bar{\sigma}_{eff} \cdot \bar{u} \right) = 0 \end{aligned} \quad (VII.7)$$

The microscale flow is described using a set of non – dimensional parameters. These parameters define the continuity of the flow and conduction properties (*Knudsen number*), temperature gradient at the surface (*Nusselt number*), heat transfer resistance of the interior and surface of a body (*Biot number*), diffusivity (*Prandtl number*), advection (*Peclet number*) and convection (*Eckert number*).

The Knudsen number is defined as mean free path of the molecules divided by the characteristic length.

$$Kn = \frac{\lambda}{\Lambda} \quad (\text{VII.8})$$

For a one-dimensional microchannel

$$Kn = \sqrt{\frac{\pi}{2}} \frac{1}{\sqrt{RT}} \frac{\mu}{\rho D_H} \quad (\text{VII.9})$$

Based on previous investigations, the Knudsen number of the flow inside the channels of the ultra-micro wave rotor was calculated as  $Kn = 2.75 - 3.39 \cdot 10^{-4}$ . These values indicate that the flow is inside the continuous flow domain.

The Nusselt number is defined as a dimensionless indicator of the temperature gradient at the surface and compares the real heat transfer from a surface with the heat transfer obtained taking into consideration only conduction.

$$Nu = D_H \frac{h}{k} \quad (\text{VII.10})$$

For silicon microchannels, convective heat transfer coefficients have been reported in the range of 24 kW/m<sup>2</sup>·K (Kang, Chen et al. 2002) up to 10 MW/m<sup>2</sup>·K (Tuckerman and Pease 1981).

The thermal conductivity of silicon varies with temperature. For the numerical simulations, a linear variation was considered based on the following values:

$k = 98.9 \text{ W/m} \cdot \text{K}$  at 400 K and  $k = 31.2 \text{ W/m} \cdot \text{K}$  at 1000 K ([www.efunda.com](http://www.efunda.com)).

The convective heat flux is calculated in FLUENT using Eq. VII.11

$$\dot{q} = h A (T_w - T_f) \quad (\text{VII.11})$$

where  $A$  is the contact area,  $T_w$  is the wall temperature, and  $T_f$  is the fluid temperature.

Next, a study was performed to investigate the influences of heat transfer upon the pressure exchange process inside the ultra-micro wave rotor channels. Three models were created and analyzed.

First model assumed adiabatic walls. The channels were modeled as a single fluid zone. The energy transfer between the channels is done only through the interface regions at the ends (see Figure VI.8).

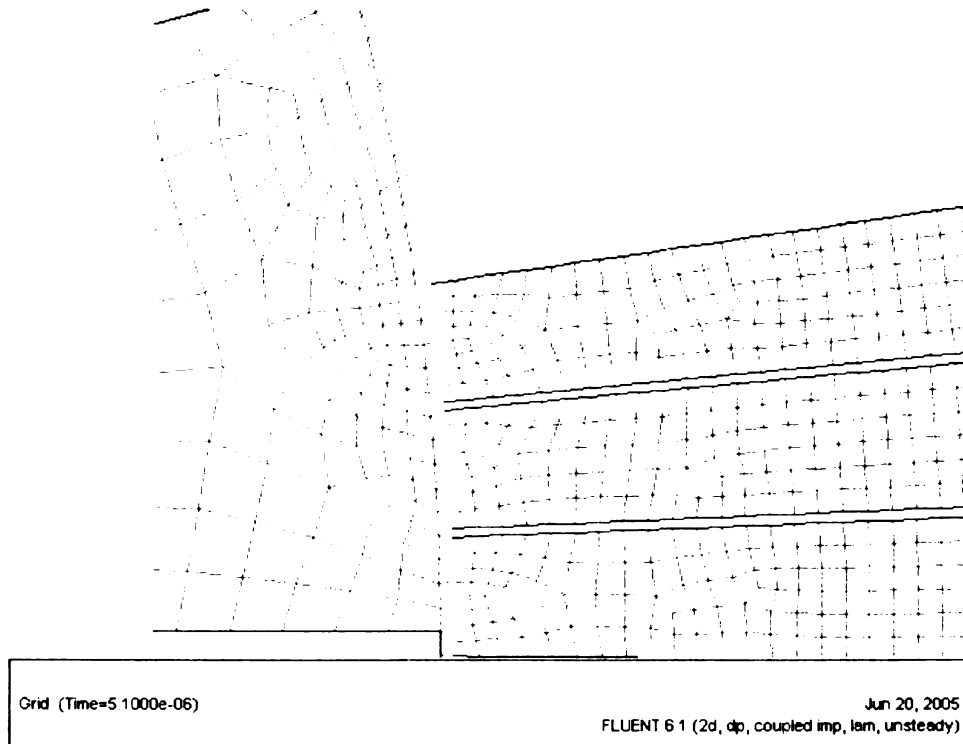


Figure VI.8: Mesh of radial wave rotor with adiabatic walls – zoom-in view.

Second model had a limited heat transfer. A mixed (convection- radiation) model was used; but the emissivity coefficient was set to 1, so only the convective part was active (see BC in the Figure VI.9). The continuum fluid zone was identical

with the first model. The value for the heat transfer coefficient was chosen based on previous approximate calculations and literature figures.

Zone Name  
wall

Adjacent Cell Zone  
channels

Thermal | DPM | Momentum | Species | Radiation | UDS

Thermal Conditions

- ☐ Heat Flux
- ☐ Temperature
- ☐ Convection
- ☐ Radiation
- ☒ Mixed

Heat Transfer Coefficient (w/m²·k) 1500 constant

Free Stream Temperature (k) 300 constant

External Emissivity 1 constant

External Radiation Temperature (k) 300 constant

Material Name  
aluminium Edit...

Well Thickness (m) 0

Heat Generation Rate (w/m³) 0 constant

OK Cancel Help

Figure VI.9: Wall boundary conditions – set up window.

Third model had an unrestricted heat transfer, governed only by the material properties. Material properties of silicon are presented in Table. A1

The model uses a two continuum zones: a fluid for over the interior of the channels and a solid for the walls. The interface between the continua is defined as a coupled wall, which is a two-sided wall. This kind of boundary condition is defined when the wall zone has a fluid and a solid region on each side. In this case no additional thermal boundary conditions are required because the solver will calculate heat transfer directly from the solution in the adjacent cells. All that needs to be specified are the material properties. The Figure VI.10 shows the meshes of the channels' interior and walls.

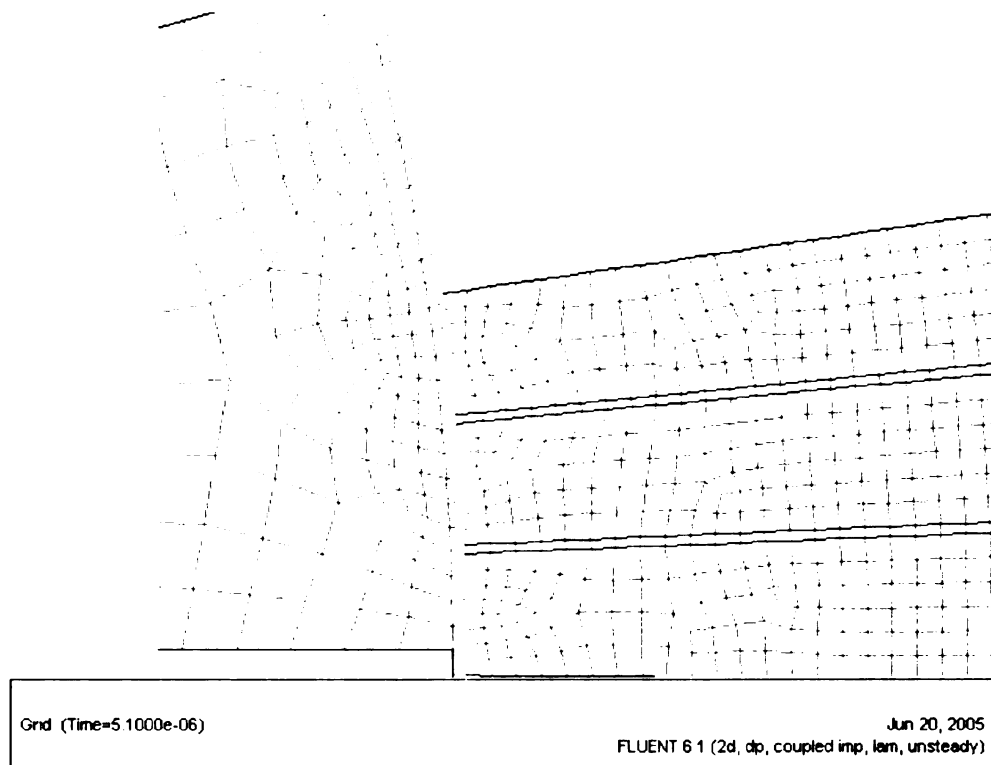


Figure VI.10: Mesh of radial wave rotor with solid walls – zoom-in view.

The three examples were based on a through-flow radial wave rotor, but the simulation was reduced to a single cycle, single set of ports.

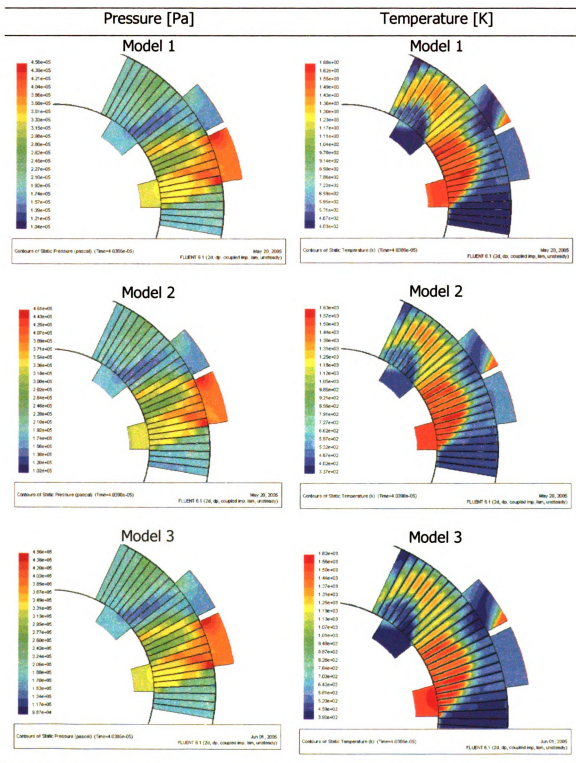
All the models used the coupled implicit solver with laminar viscosity. The gas was defined as compressible ideal gas with a laminar viscosity dependent on temperature – Sutherland law (Sutherland 1893). The implicit solver used the unsteady flow option with the first order, upwind scheme. No-slip boundary conditions were defined for all three examples.

If the coupled solver option is used in setting up the numerical model of a compressible flow, the pressure work and kinetic energy as well as diffusion at inlets is automatically accounted for.

Table VI.1: Comparison of numerical results between the three models.

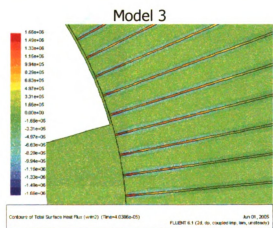
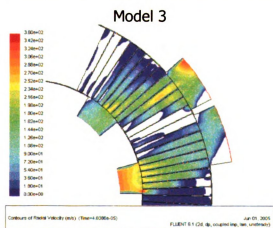
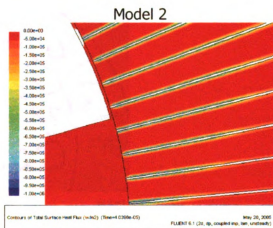
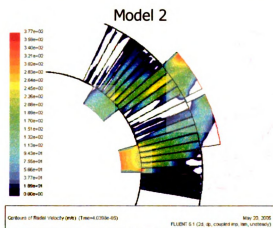
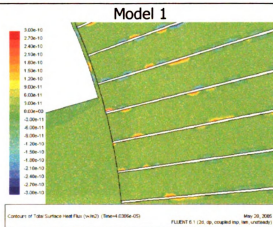
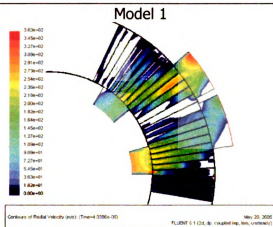
	Model 1	Model 2	Model 3
$p_{max}$ [bar]	4.56	4.61	4.56
$T_{max}$ [K]	1680	1630	1620
$q_{fluid}$ [W/m <sup>2</sup> ]	0	$-1 \cdot 10^6$	$-1.66 \cdot 10^6$
$q_{solid}$ [W/m <sup>2</sup> ]	N/A	N/A	$1.66 \cdot 10^6$
$h_{surface}$ [W/m <sup>2</sup> ·K]	0	-1540	-11000
$u_{max-fluid}$ [m/s]	291	283	288

Table VI.2: Comparison of contour plots between the three models: pressure, temperature, velocity, heat flux and heat transfer coefficient.



Positive Radial Velocity [m/s]

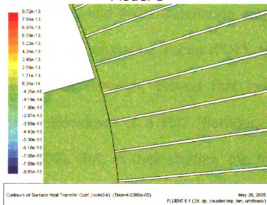
Surface Heat Flux [ $W/m^2$ ]



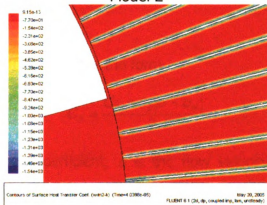


## Surface Heat Transfer Coefficient [ $\text{W/K}\cdot\text{m}^2$ ]

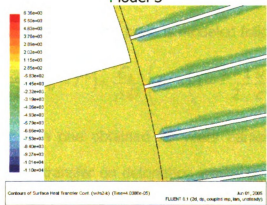
Model 1



Model 2



Model 3



The results seem conform with the conclusions from extant literature on heat transfer impact on shock tubes and Pulse Detonation engines (PDE). Studying the behavior of PDE and Pulse Detonation Tubes (PDT), the research group at Stanford University led by Dr. Hanson, proved that heat transfer plays an important role during the blowdown of a PDT (Barbour, Hanson et al. 2005; Radulescu and Hanson 2005). But, in their studies, the friction effect was not considered having a separate influence on the behavior of the flow, instead they incorporated the effect of friction into the heat transfer, based on the Reynolds analogy.

The heat transfer coefficient  $C_h$  has the form

$$C_h = \frac{C_f \rho c_p |u - u_w|}{2} \quad (\text{VII.12})$$

where  $C_f$  is the friction coefficient,  $u$  is the flow velocity and  $u_w$  is the wall velocity ( $u_w = 0$ ).

The heat transfer mechanism that influences the flow field in a PDE is mainly convective. The heat loss rate per unit mass is modeled following the equation:

$$q = \frac{C_h}{\rho D} (T_w - T^0) = \frac{C_h}{\rho D} \left( T_w - \left( 1 - \frac{\gamma - 1}{2} \frac{u^2}{c^2} \right) T \right) \quad (\text{VII.13})$$

Their result is similar with one obtained 30 years earlier when studying the influence of the wall heat transfer on detonation waves by Edwards, Brown and others in the United Kingdom. When analyzing the expansion waves, it was assumed that the Reynolds analogy holds between friction force and convective heat transfer, so that both effects can be accounted for by means of a single

friction coefficient,  $C_f$  (Edwards, Brown et al. 1970). The conclusion is that the rate of heat transfer falls linear with pressure, which requires  $\dot{q}(t)$  to vary linearly with flow velocity and thus initial density. It was concluded that

$$\dot{q} = \frac{St}{Re^{1/5}} 4.46 \cdot 10^{-2} \quad (\text{VII.14})$$

where  $St$  is the Stanton number.

Thus,

$$\dot{q} = \frac{h v^{6/5}}{u^{6/5} L^{1/5} c_p \mu} 4.46 \cdot 10^{-2} \quad (\text{VII.15})$$

Again, it was proven that the convective term is the one that influences the heat transfer from the fluid to the walls of a shock tube.

This was the conclusion of the research group at NASA investigating the wave rotors and the gasdynamic process inside the rotor cells (Paxson and Wilson 1993). Moreover, Dr. Wilson stated that the heat losses are very low and could be incorporated in the friction losses, since both depend on the same parameter, the friction coefficient (Wilson 1998).

### *Conclusions*

Pressure, temperature, and velocity are the parameters that characterize an unsteady compression process. When comparing their distributions between the three models, small variations can be noticed. The maximum pressure difference between models is 1%, temperature – 3.5%, velocity – 2.7%. As expected, the maximum temperature and maximum velocity of the flow was reduced when heat transfer was included in the model.

The heat flux values are similar between model 2 and 3, but the surface heat coefficient is much higher when calculated automatically by FLUENT. The maximum heat transfer coefficient is  $11 \text{ kW/m}^2 \cdot \text{K}$ , which is below the values documented previously.

The heat transfer process was implemented successfully to the numerical model by two methods. The pressure and temperature distributions were compared with the original (no heat transfer) model and differences in results were computed from 1% to 3.5%. The distribution of parameters was unchanged when heat transfer was included.

Section VII.5 contains CFD simulations of more detailed models of radial wave rotors. It will be shown that convective heat transfer plays a more important role in influencing the flow field inside the rotor cells than conductive heat transfer by analyzing the Nusselt number.

## **VI.4      Axial U<sub>μ</sub>WR**

There are two possible configurations of the axial wave rotor: through-flow and reverse-flow. Based on data available from the MIT Micro Gas Turbine Project (Kang 2001; Epstein 2004; Frechette, Jacobson et al. 2005) initial thermodynamic calculations were performed to find the optimum design point. A detailed description of these calculations was presented in section III.5.

Two sets of data were extracted from the design space of ultra-micro wave rotors. The first set was determined by enforcing the continuity equation. Port dimensioning was based on time calculations and a set tangential speed of 183m/s. The second set of thermodynamic parameters was based on maintaining the essence of wave rotor engine, thus supplying exhaust gas to the turbine with higher pressure than fresh air coming from the compressor.

Table VI.3: Thermodynamic parameters of the ultra-micro wave rotor – set one.

	Pressure [bar]	Temperature [K]
Low Pressure Air (LPA)	1.96	435
High Pressure Air (HPA)	3.93	542
Low Pressure Gas (LPG)	1.62	1500
High Pressure Gas (HPG)	3.53	1589

Table VI.4: Thermodynamic parameters of the ultra-micro wave rotor – set two.

	Pressure [bar]	Temperature [K]
Low Pressure Air (LPA)	1.965	435
High Pressure Air (HPA)	3.93	542
Low Pressure Gas (LPG)	2.72	1500
High Pressure Gas (HPG)	3.53	1589

Table VI.5: General thermodynamic parameters of the ultra-micro wave rotor.

Wave Rotor Pressure Ratio	$\Pi_{WR}$	2
Ambient Temperature	$T_0$	293K
Specific Heat for Air	$C_{p_{air}}$	1.005 kJ/Kg·K
Polytropic Coefficient for Air	$\gamma_{air}$	1.4
Efficiency of Combustion	$\eta_{Comb}$	80%

Using the 1D code for the one channel described above, and having the overall geometric dimensions of the wave rotor from the design in Figure II.1, a porting solution was found for the axial wave rotor. The next table presents this set of data.

Table VI.6: Details of the full model.

Length of channels	1mm
Radius of the rotor	5mm
Number of cells (channels)	240
Cell width	130 $\mu$ m
Rotational speed	350,000RPM
Tangential velocity	183m/s

Port openings	Degree	Circ. Length [mm]	Time [s]
HPG open	0.00	0.000	0.00E-06
HPG close	6.87	0.600	3.28E-06
HPA open	3.83	0.335	1.83E-06
HPA close	9.08	0.792	4.33E-06
LPA open	12.98	1.133	6.19E-06
LPA close	23.33	2.037	1.11E-05
LPG open	9.93	0.867	4.74E-06
LPG close	18.74	1.636	8.94E-06

The full model had a 12 cycles per revolution (Figure VI.11-a) configuration; but due to enormous computational volume, a reduced model was later created. The reduced model had a one cycle per revolution configuration and kept the same dimensions of the channel, the same tangential speed and same boundary conditions (Figure VI.11-b). The data for the reduced model are presented in the following table.

Table VI.7: Details of the reduced model.

Length of channels	1mm
Radius of the rotor	0.42mm
Number of cells (channels)	20
Cell width	130 $\mu$ m
Rotational speed	4,200,000RPM
Tangential velocity	183m/s

Port openings	Degree	Circ. Length [mm]	Time [s]
HPG open	0	0.000	0.00E-06
HPG close	81.88	0.600	3.28E-06
HPA open	45.68	0.335	1.83E-06
HPA close	108.09	0.792	4.33E-06
LPA open	154.53	1.133	6.19E-06
LPA close	277.85	2.037	1.11E-05
LPG open	118.33	0.867	4.74E-06
LPG close	223.18	1.636	8.94E-06

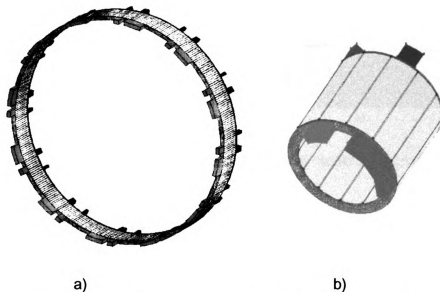


Figure II.11: 3D model of axial wave rotor: a) full model with 12 cycles per revolution, b) reduced model with 1 cycle per revolution.

The gap between the rotating drum and the end plates that house the ports is essential. A study on the influence of this gap prove that for both  $2\mu\text{m}$  and  $20\mu\text{m}$  the pressure rise has comparable values (Figure II.1) and the wave pattern is



almost the same. For future investigations a  $20\mu\text{m}$  clearance will be used. The gap has both a physical and a computational effect. The  $2\mu\text{m}$  gap would be extremely difficult to obtain with today's microfabrication possibilities. Also, from the computational one point of view such a gap would be difficult to obtain, since the mesh in the gap has to have a certain length/width ratio, which affects the rest of the meshes in the model. A too coarse mesh in the gap will result in inaccurate results; a too fine mesh will result in huge computational time.

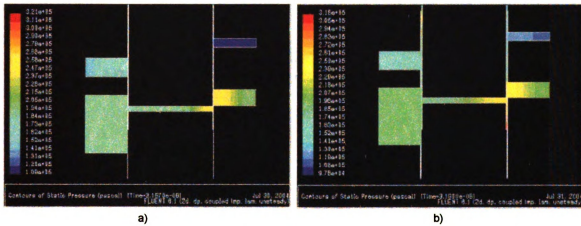
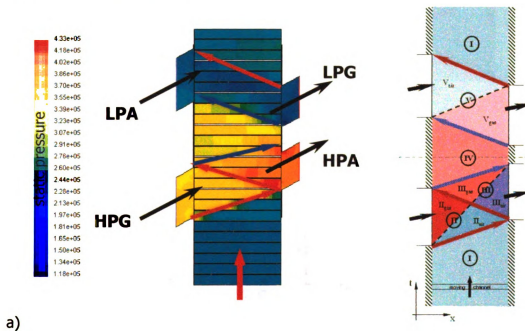


Figure VI.12: Pressure distribution for a single channel mode: a)  $2\mu\text{m}$  gap, b)  $20\mu\text{m}$  gap.

### Through Flow/Reverse Flow

Both CFD models (TF & RF) predict the wave pattern desired, the pattern decided for the porting scheme by the 1D in-house code. It appears though, that the HPA port is opening too soon, meaning that the speed of the rotor is too high. In Figure VI.13 it can be seen the expected pressure wave pattern with two shock and an expansion wave for the high pressure part and one shock and one expansion for the low pressure part, very close to the theoretical prediction displayed on the right

side. The contour plots are very similar with the ones in Figures V.4 and V.6, which were results of the 1D code. The temperature distribution (Figure VI.14) shows that the shock heats up the fresh air but a lot less than the temperature of the hot gases, which are around 1500K. The advantage of the RF wave rotor is that hot gases exit on the same side as they enter, thus scavenging all the hot temperature fluid and keeping the rotor cooled.



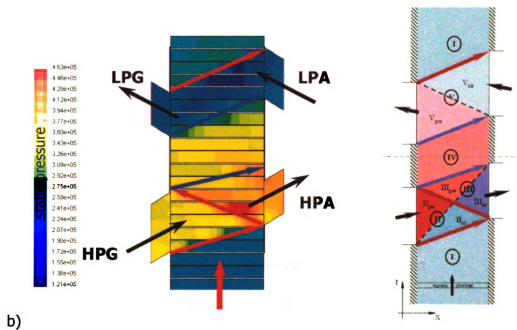


Figure VI.13: Pressure distribution for 2D simulation of axial wave rotor:  
a) TF model, b) RF model, [Pa].

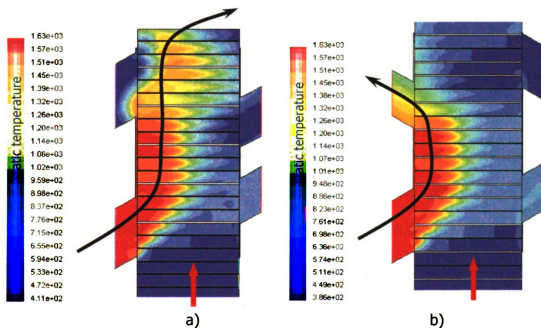


Figure VI.14: Temperature distribution for 2D simulation of axial wave rotor:  
a) TF model, b) RF model, [K].

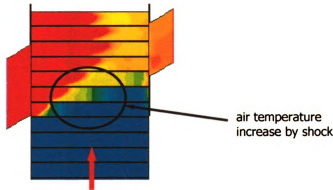


Figure VI.15: Low temperature distribution.

Figure VI.15 is a zoom-in from Figure VI.14, having the maximum temperature value limited to 1000K (red color). The flow temperature is increased by the shock wave; this phenomenon being clearly observed in the figure. Thus, disregarding the high temperature of the exhaust gas, the shock trajectory can be traced on the temperature contour plot.

The velocity distribution in Figure VI.16-a demonstrates that this is a truly TF wave rotor, having all the inflows and outflows in the same direction. The Figures VI.16 b and c, presenting a RF wave rotor displays a correct direction of the flow through the ports, with a positive direction on the high pressure part and negative on the low pressure part. Some oscillations in the flow direction are noticed when channels are closed, but their magnitude indicate that they do not influence the flow on the ends of the channels.

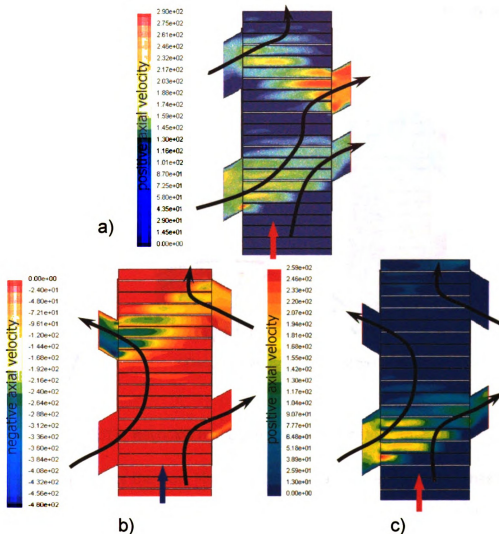


Figure VI.16: Velocity distribution in an axial wave rotor: a) TF – positive direction flow, a) RF – negative direction flow, c) RF – positive direction flow, [m/s].

The Reynolds number is below 400 in all the channels and at all times, as shown in the snap-shot presented in Figure VI.17. Based on previous research, stating that laminar flow in microchannels is characterized by  $Re$  below 1500 – 2000 (Choi, Barron et al. 1991; Hao, He et al. 2005), the flow in the wave rotor channels is well into the laminar region. This result enforces the accuracy of the

CFD model, by reducing the number of inaccuracies in the fluid dynamics equations.

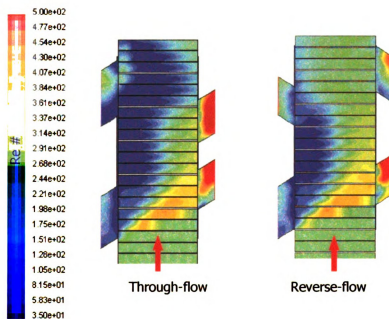


Figure VI.17: Reynolds number distribution for axial wave rotor.

Figure VI.18 presents the flow Mach number. It can be seen that the maximum value for the axial wave rotor, inside the channel, for both through-flow and reverse-flow configurations is 0.8. That means the shock Mach number reaches 1.59, thus the shock travels at supersonic speed.

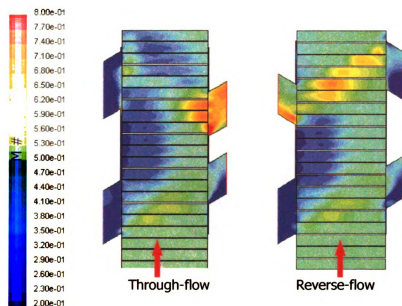


Figure VI.18: Flow Mach number distribution for axial wave rotor.

Results of 3D investigation of the reduced model show that a higher rotational speed is needed, the shock wave reaching the end of the channel short of the high pressure exhaust port (Figure VI.19).

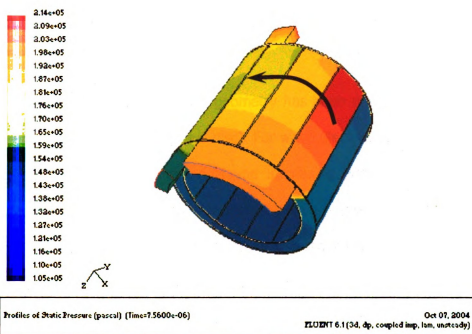


Figure VI.19: Pressure distribution in the channels of the 3D reduced axial wave rotor model.



## **VI.5      Radial U<sub>μ</sub>WR**

As described in section II.2 a new geometry has been envisioned for the wave rotor – the radial wave rotor (wave disc). For wave discs, centrifugal acceleration acting on the fluid in the channels and increasing with radius needs to be considered in governing equations additionally. In a proper port configuration the presence of centrifugal forces can improve the scavenging process, which is a typical challenge in wave rotor design and operation. In the radial configuration, depending on the application, the wave rotor can be designed with several cycles per revolution. The overall dimensions and the mass flow rate, as well as the wave pattern will determine the width of the ports. Increase of wave disc rotational speed increases centrifugal forces and reduces the number of ports, which can be located in a disc of the same diameter. Hence, for higher speed, instead of several port sets and two cycles per revolution only one port set and one cycle per revolution could be used.

There exist four configurations in each the wave disc ports can be positioned: (1) a through-flow wave rotor with fluids traveling from inside to outside radius, (2) a through-flow with flow coming from outside to inside, (3) a reverse-flow with gas ports located on the inner radius, and (4) a reverse-flow with air ports located on the outer radius.

In this study only three models were created and analyzed (models 1, 3, and 4) since model 2 presents no apparent advantage.

### VI.5.1 Through-Flow Radial Wave Rotor

A single cycle was studied in the beginning to build confidence in the model. At the same time, the single cycle model was used to establish the final configuration of the porting scheme. Starting with the port configuration given by the 1D gasdynamic model, the Gambit model was created and analyzed into Fluent – first iteration. Only some of the channels are used to reduce calculation time, thus allowing for simple tests of compression and expansion processes with a much finer grid. This method is used to find a rotational speed at which the compression and expansion process is better tuned with the port opening and closing fixed in this study.

Figure VI.20 shows the porting solution as well as the flows (air and gas) trajectories.

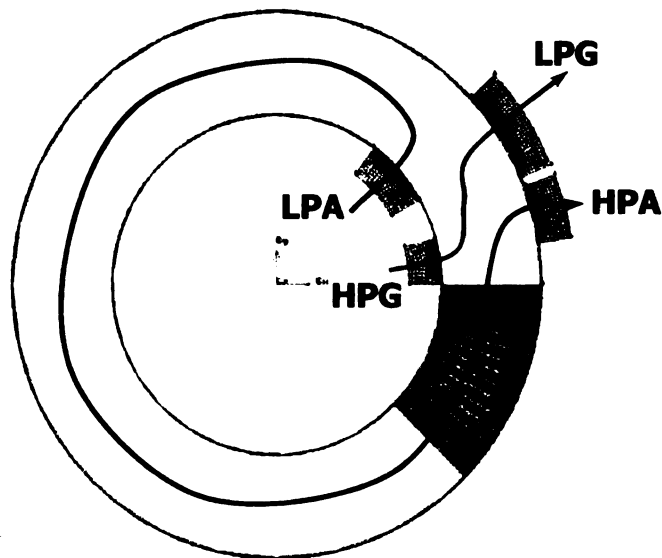


Figure VI.20: Through-flow wave disc – porting schematic.

Figure VI.21 presents the static pressure distribution for the first iteration. As it can be seen from the tentative pressure wave trajectories, the port timing needs some modifications, since neither the first expansion wave on the high pressure part, nor the pressure waves in the low pressure part do not meet the ports at their proper times. This effect can be also observed in the radial velocity contour plots shown in Figure VI.22, where there is some outflow in the LPA port, instead of inflow.

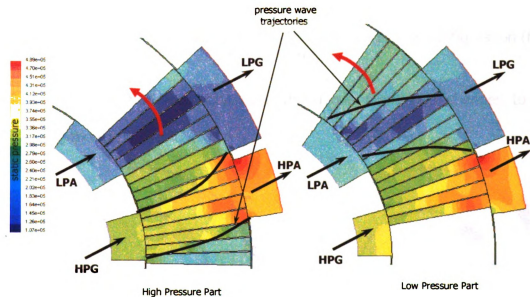


Figure VI.21: Pressure distribution for the through-flow configuration (first iteration), [Pa].

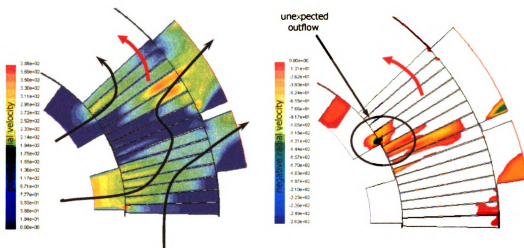


Figure VI.22: Radial velocity distribution for the through-flow configuration (first iteration), [m/s].

The second iteration incorporates all the above mentioned changes to the following model (Figure VI.23).

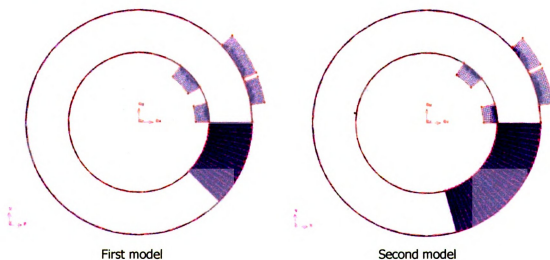


Figure VI.23: Comparison between initial and updated models.

Figure VI.24 presents the pressure distribution for the high and low pressure parts of the wave rotor. Both pictures show the same results, but the scale of

pressure values is different in each plot to visualize pressure trajectories in each part more accurately. The picture on the left shows the full pressure spectrum, while the one on the right shows the pressure values characteristic of the high pressure part. It can be seen that the behavior of the flow is as expected. Primary shock generated by the opening of the HPG port arrives at the outer radius at the moment when the HPA port opens. It reflects off the end wall as a secondary shock wave. An expansion wave generated by closing of the HPG port travels to the point of closing the HPA port. In the low pressure part, the results reveal small design offsets. An expansion wave is generated by closing of the LPG port, while a shock wave is produced by the closing of the LPA port. The second wave appears to be advanced by one channel width and reached the LPG port earlier than expected.

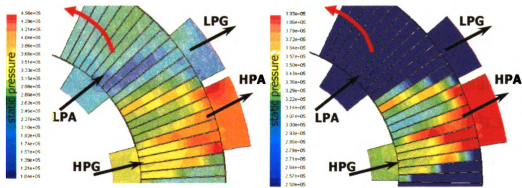


Figure VI.24: Through-flow wave disc– static pressure distribution, [Pa], left: full pressure spectrum, right: pressure values form  $2.5 \cdot 10^5$  to  $3.93 \cdot 10^5$  Pa.

Figure VI.25 shows the temperature distribution revealing the penetration of hot gases towards the end of the channel. Centrifugal forces assist driving the gases from the inner ports towards the outer side. The gas penetration length is

increased by boosting the pressure of the high-pressure part (or lowering the pressure of the low-pressure part) and increasing the number of port sets (cycles) as shown in the next figure.

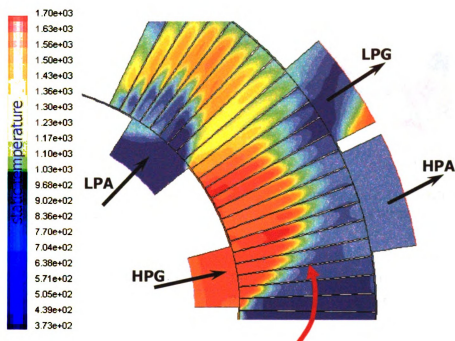


Figure II.25: Through-flow wave disc – static temperature distribution, [K].

To simulate the wave rotor internal gasdynamic process through several cycles, a four cycle per revolution model was created. As seen in Figure II.1-a, the temperature distribution shows that after several cycles, the hot gases travel the channel length and exit at the outer ports. In addition, the average temperature of the fluid in the hot zone of the channels reduces from about 1300K to 1000K. The hot gas penetration is even deeper if the port pressures are changed and the shock strength is increased. Figure II.1-b simulates such a situation where corresponding port pressures are listed in Table II.1.

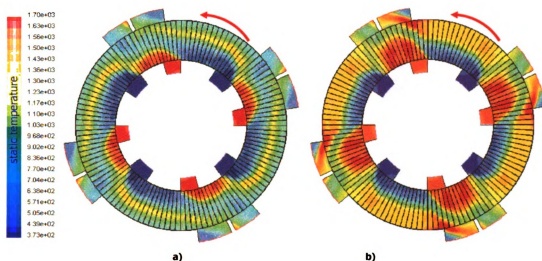


Figure VI.26: Through-flow wave disc – static temperature distribution, [K]  
a) lower port pressures, b) boosted port pressures.

Table VI.8: Wave rotor operating conditions adjusted for higher pressures in the high-pressure region and lower pressures for the low-pressure region.

	Pressure [bar]	Temperature [K]
Low Pressure Air (LPA)	1.50	435
High Pressure Air (HPA)	4.50	542
Low Pressure Gas (LPG)	1.62	1500
High Pressure Gas (HPG)	4.00	1589

The radial velocity vectors presented in Figure VI.27 represent well the characteristics of radial-flow wave rotors. As expected for the through-flow configuration, the flows are directed from the inner ports toward outer ports. They are also indicators of some offset port timing, for instance the part of the outflow at the HPA port (lower right corner) tends to return to the channels. This shows that the width of the HPA is designed greater than the optimized value.

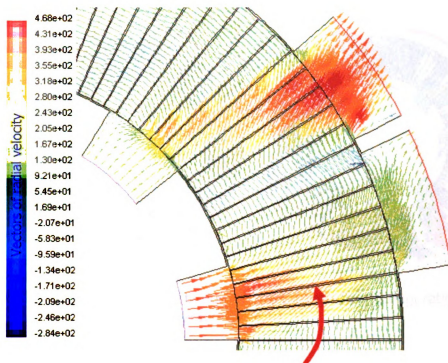


Figure II.27: Through-flow wave disc – velocity vectors distribution, [m/s].

Although the second model delivers improved results in terms of pressure waves and port timing, as well as inflows and outflows, the problem of resultant velocities of the outflow and inflow has remained. The flow has both a radial component due to flow traveling along the channel, but also a tangential component due to the rotation of the disc (Figure II.27). The third iteration works on improving the shape of the ports. Figure II.3 highlights the port shape changes as well as an improvement in the flow through the ports.



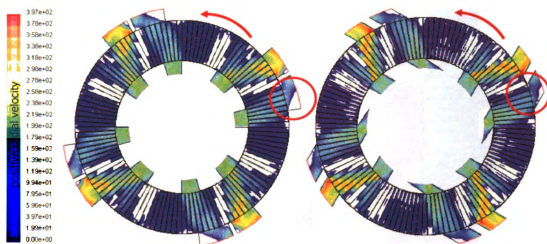


Figure VI.28: Radial velocity distribution for the through-flow configuration (third iteration), [m/s].

Overall, the influence of the centrifugal force is best seen when comparing the axial wave rotor with the radial one after one cycle, the models having identical initial and boundary conditions. Figure VI.29 shows the difference in hot gas penetration along the channel. It can be seen that flow with temperature of 1300K goes almost all the way to the right side wall in the case of the wave disc, while for the axial wave rotor it travels only three quarters of the way.

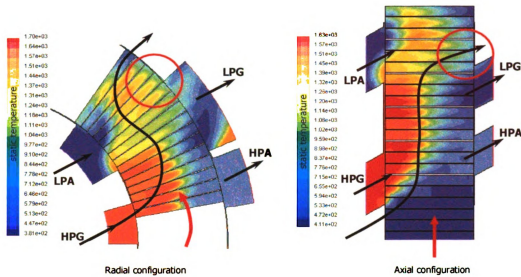


Figure VI.29: Comparison of radial and axial flow wave rotors – static temperature distribution, [K].

As proven in section VII.3, the heat transfer between adjacent cells is not influencing significantly the energy exchange process inside the wave rotor. Next, the influence of other components of the ultra-micro gas turbine was investigated. Heat transfer coming from the combustion chamber located below the wave disc, or the turbine located in the lower interior of the wave disc is studied. For this, constant temperature boundary conditions have been set: in the first case, the walls between the cells were considered having a constant 2000K temperature; in the second case, the interior wall between the ports was assigned the same boundary condition (Figure VI.30). Results have shown that in the first case, the overall temperature of the fluid inside the channels has increased (Figure VI.31), but that did not affect the overall pressure distribution (Figure VI.32).

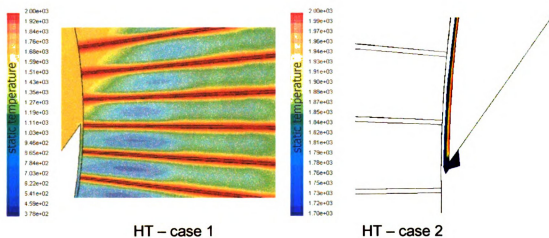


Figure VI.30: Temperature boundary conditions for the external heat transfer investigations, [K].

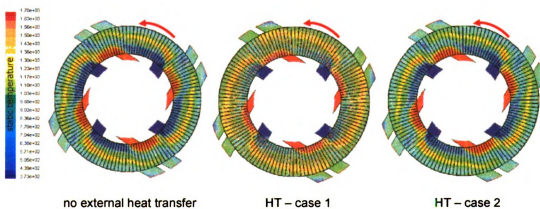


Figure VI.31: Comparison of temperature distributions without and with external heat transfer, [K].

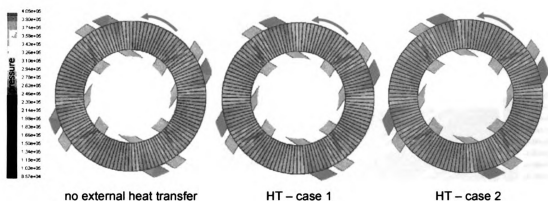


Figure VI.32: Comparison of pressure distributions without and with external heat transfer, [Pa].

When examining the Nusselt number distribution along the cells' walls, Figure VI.33, it can be noticed that the values are going up to several thousands. Considering the definition of Nusselt number (Eq. VII.10), the conclusion is that the convective heat transfer is much higher than the conductive one. So heat will be transferred from the walls (the heat source in case 2) to the fluid, but not from one cell to the other through the walls. Flow in one channel does not influence the flow in the adjacent channels through the walls.

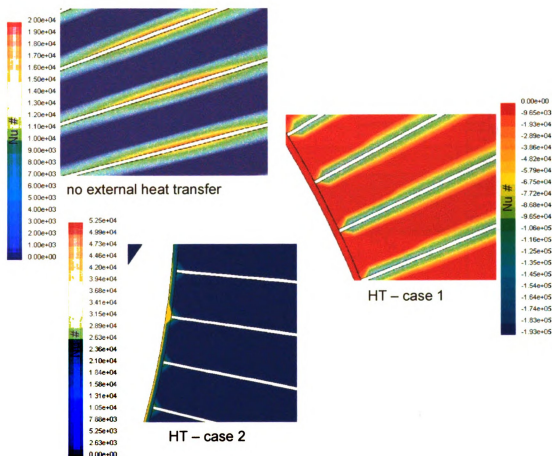


Figure VI.33: Comparison of Nusselt number distributions along the rotor walls without and with external heat transfer.

### Entry Lengths and Boundary Layers

Important factors in the fluid flow behavior and heat transfer to and from the walls are the flow and thermal entry lengths, as well as velocity and thermal boundary layers thicknesses. Figure VI.34, below, describes schematically the flow at the entrance to the channels, showing the entry lengths and boundary layers.

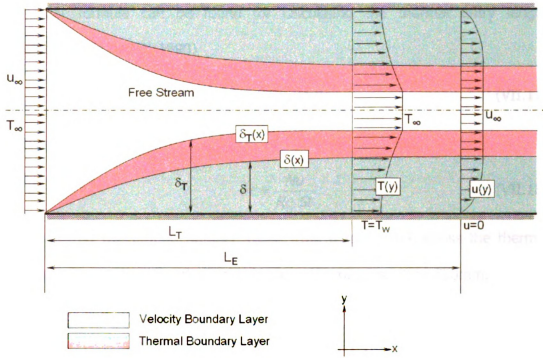


Figure VI.34: Schematic of flow entry into a channel.

It is known from preliminary investigations that the flow has a highly laminar aspect ( $Re < 1000$ ), thus the calculation of the flow (velocity) entry length can be performed using Eq. VII.16 (Sabersky, Acosta et al. 1998)

$$\frac{L_E}{D} \approx 0.06 Re \quad (VII.16)$$

Assuming that  $Re$  varies from 100 to 1000 along the channel length, and knowing that the average diameter is  $300\mu m$ , it results in an average entry length  $L_E = 9mm$ . The minimum and maximum entry lengths are 1.8mm and 18mm respectively. The conclusion is that the flow has not reached the fully developed state while passing through the wave rotor channels.

A similar formula can be found for calculating the thermal entry length (Incropera and DeWitt 1990)

$$\frac{L_T}{D} \approx 0.05 Re Pr \quad (VII.17)$$

Knowing that

$$Pr = \frac{Nu}{Re St} \quad (VII.18)$$

it shows that the Prandtl number varies from 0 to 101.84 across the thermal boundary layer. Thus, the thermal entry length varies from 0 to 750mm.

As expected for such small channel diameters and high temperatures, the entire flow is placed in the combined entry lengths region. A pressure drop in developing regions exceeds its value in the fully developed region because it must overcome the wall shear and increase in flow momentum. Similarly, the heat transfer has increased values, but not high enough to influence the flow behavior.

When investigating the boundary layers thicknesses, the Euler equations lead to specific solutions for the case studied. The thermal boundary layer thickness is

$$\delta_T(x) = 3.6 \sqrt{\frac{\alpha x}{u_\infty}} \quad (VII.19)$$

where  $x$  is the coordinate along the channel (see Figure VI.34) and  $u_\infty$  is the velocity of the free stream.

The Reynolds analogy between the flow field and the thermal field along the wave rotor channel length is used. Introducing the assumption of large Prandtl

number ( $Pr > 5$ ), it results the following relation between the velocity and thermal boundary layer thickness:

$$\frac{\delta_T}{\delta} = 0.975 \sqrt[3]{Pr} \quad (VII.20)$$

Using Eqs. VII.19 and VII.20 the two boundary layers thickness can be computed:  $\delta_T \approx 53\mu\text{m}$  and  $\delta \approx 15\mu\text{m}$ . Although these values are not identical with the one provided by the CFD code ( $\delta_T \approx 75\mu\text{m}$  and  $\delta \approx 48\mu\text{m}$ ) it has been shown that the range of values are similar. The discrepancies in results come from the many approximations and averaging of the non-dimensional parameters used in the theoretical formulas.

#### VI.5.2 Reverse-Flow Radial Wave Rotor

In this section, two different reverse-flow models are studied to highlight the differences between such configurations. Results of such a comparison can be used to evaluate the advantageous and disadvantageous of each design for a specific application. Figure VI.35 shows the flow trajectories for the air and exhaust gases of each case. The same procedure was applied for the reverse-flow configuration as for the through-flow. Initially a single cycle was studied until the best porting solution was found, then after the CFD iterations, the full model with four-cycle per revolution was investigated.



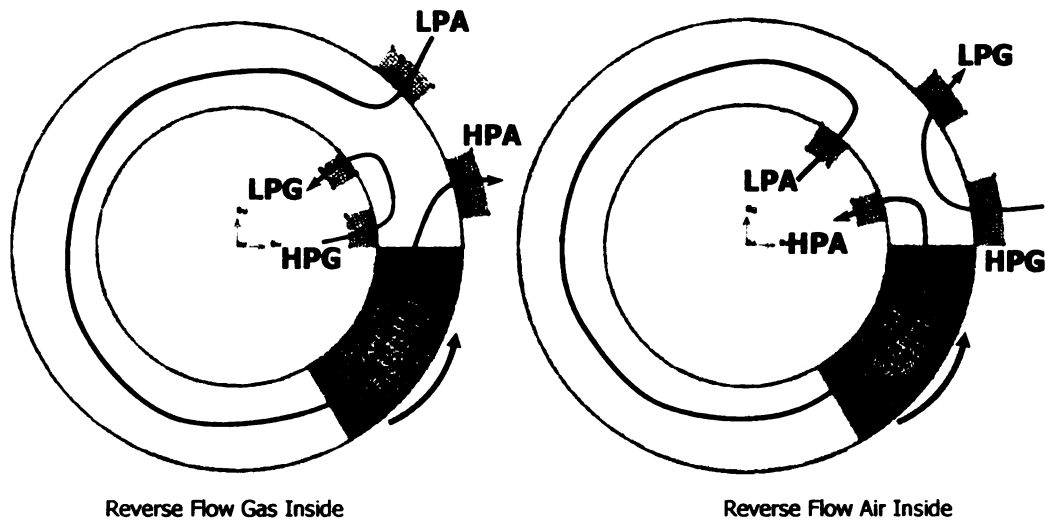


Figure VI.35: Reverse-flow wave disc – possible port arrangements.

The pressure distribution of the two models, displayed in Figure VI.36, are similar in the high-pressure part (bottom part of the figures), considering the direction of the flow. Some discrepancies exist due to the influence of the centrifugal forces for different flow directions. On the low-pressure part (top part), a better stratification of the flow can be seen for the air inside model. The wave patterns are in agreement with the wave rotor gasdynamic theory and they clearly show the effects of compression and expansion waves.

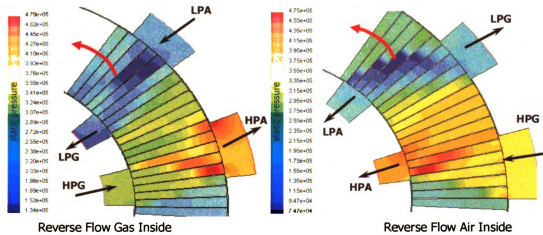


Figure VI.36: Reverse-flow wave disc – static pressure distribution, [Pa].

The temperature distributions shown in Figure VI.37 show that the air inside model has a better hot flow scavenging feature due to the positive influence of the centrifugal forces. For both models, most of the hot gases are exhausted through the LPG ports.

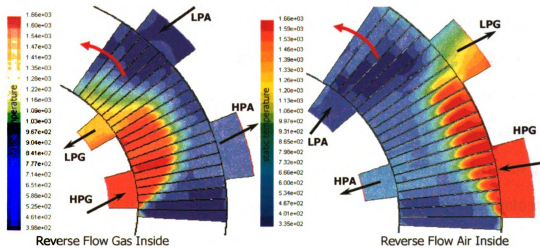


Figure VI.37: Reverse-flow wave disc – static temperature distribution, [K].

The ideal gas flow assumption allows for considering density as directly proportional with pressure at constant temperatures regions. Thus, by studying

the density plots for the two models shown in Figure VI.38, it can be seen that a larger amount of high pressurized air is extracted by the HPA port on the gas inside model, rather than air inside model. The results clearly indicate that the configuration with inner air ports has a better scavenging feature.

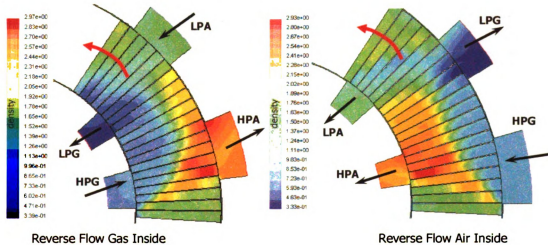


Figure VI.38: Reverse-flow wave disc – density distribution,  $[\text{kg/m}^3]$ .

Figure VI.39 shows the radial velocity distributions (inward and outward). The flow patterns are consistent with the predictions for reverse-flow configurations. By studying the velocity contour plots, one can see that further improvements can be done in the geometry of the ports for better flow guidance and avoiding backflows or undesired flow direction. For example, in the configuration with gas inside (figures on the left), the HPA port has a zone where the air flows into the channels which is not desired. The ports should be adjusted to account for tangential component of flow velocity, by inclining the walls with respect to the channels. Some small backflows can be seen in the LPG port of the rotor with inside air configuration.

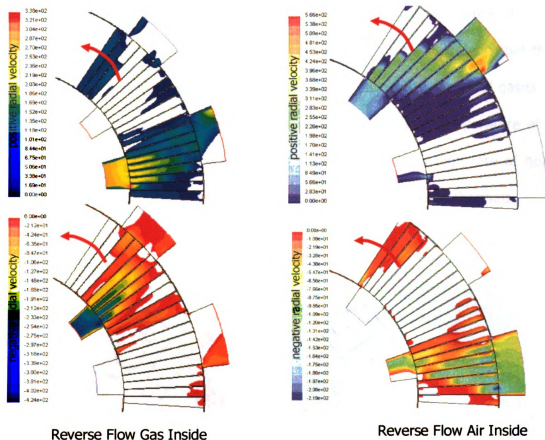


Figure VI.39 Reverse-flow wave disc – radial velocity distribution, [m/s].

Figures VI.40, indicating the temperature distributions in the reverse-flow wave disc with inner air ports, compares the model with one set of ports with a full model with four cycles per revolution. Alternatively, Figure VI.41 makes a similar comparison for the reverse-flow wave disc with inner gas ports. The port timing, rotor geometry, and the operating conditions are the same in both full models. In Figure VI.40, the gas penetration reduces after several revolutions while it increases for the reverse-flow configuration with the gas ports on the inner

radius shown in Figure VI.41. Therefore, the channel wall mean temperature is less for the reverse-flow wave disc with the inner air ports. It is seen that the burned gas almost leaves the channel at the end of each cycle. Residual gases of the reverse-flow wave disc with inner gas ports keep the wall temperature at a high temperature during the wave rotor operation, causing a high rate of heat transfer and non-uniform temperature distribution along the rotor channels.

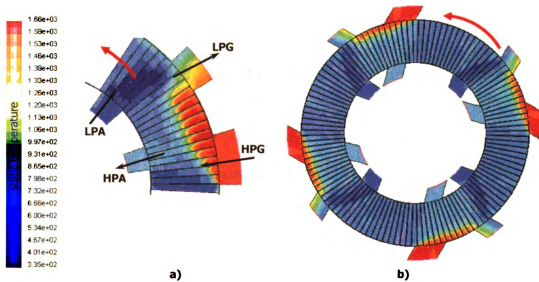


Figure VI.40: Reverse-flow wave disc with air ports on inner diameter – temperature distribution, [K]: a) results after first cycle, b) results after several cycles.

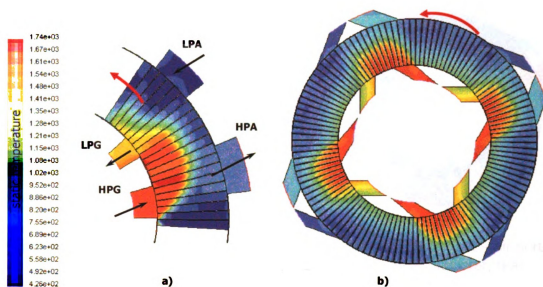


Figure VI.41: Reverse-flow wave disc with gas ports on inner diameter – temperature distribution, [K]: a) results after first cycle, b) results after several cycles.

Figure VI.42 presents the static pressure distribution, and it can be clearly seen that the updated geometry provides an accurate wave pattern for both reverse-flow configurations. Also the velocity distribution (Figure VI.43) shows the appropriate directions of the flow through each port, red arrows indicate the active ports.

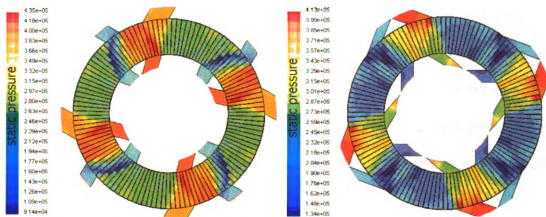


Figure VI.42: Reverse-flow wave disc – static pressure distribution: left – air ports located on inner diameter, right – gas ports located on inner diameter, [Pa].

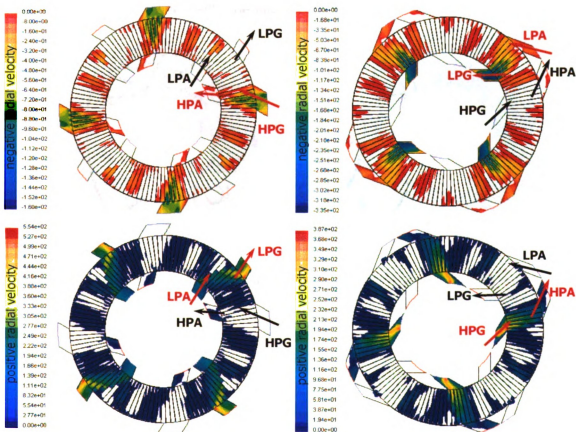


Figure VI.43: Reverse-flow wave disc – static pressure distribution: left – air ports located on inner diameter, right – gas ports located on inner diameter, [Pa].

The port inclined solution delivers more accurate results and better conclusions can be formulated. The Mach number is higher for the configuration with air ports located on the inner diameter, showing that pressure waves travel faster and thus improving the flow and energy exchange in the low pressure part. For the high pressure part, the values are comparable for both configurations (Figure VI.44).

The Reynolds number distribution (Figure VI.45) shows similar values for both cases, with a maximum around 1300 inside the channels. This will place the flow in the wave rotor cells well inside the laminar region.

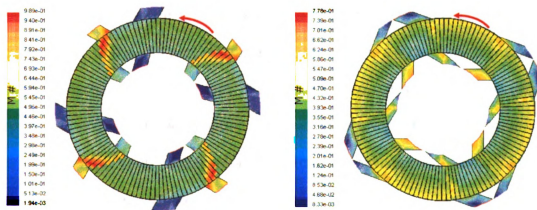


Figure VI.44: Reverse-flow wave disc – Mach number distribution: left – air ports located on inner diameter, right – gas ports located on inner diameter.



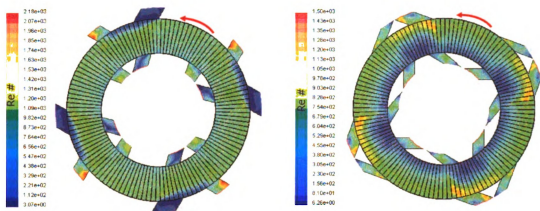


Figure VI.45: Reverse-flow wave disc – Reynolds number distribution: left – air ports located on inner diameter, right – gas ports located on inner diameter.

As for the through-flow configuration, the reverse-flow was investigated with a new set of given parameters, in which the pressure of the LPG port is higher than the one of the LPA port. This is a true wave rotor configuration in which the pressure exchanger actually tops the baseline cycle. Based on a new design cycle, a new geometry was created for a model of reverse-flow wave rotor with air ports on the inside of the rotor. The values of pressure and temperature in the ports are presented next:

Table VI.9: Wave rotor operating conditions adjusted for higher pressures in the high-pressure region and lower pressures for the low-pressure region.

	Pressure [bar]	Temperature [K]
Low Pressure Air (LPA)	1.94	443
High Pressure Air (HPA)	3.88	582
Low Pressure Gas (LPG)	2.11	1500
High Pressure Gas (HPG)	3.10	1616

The results are presented side by side with the one from the original RFAI model. In Figure VI.46 the pressure distribution is presented for the two models. First observation is that the new model is not optimized in terms of port timing. If for the original design (on the left) the pressure waves' trajectories are clearly defined, the same thing cannot be said about the new design.

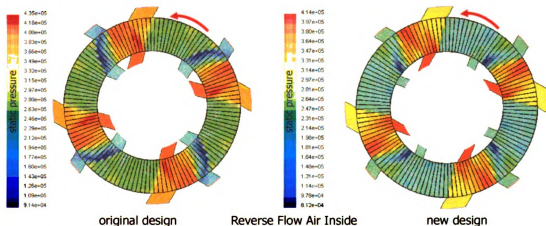


Figure VI.46: Static pressure distribution for the RFAI models, [Pa].

The low pressure part shows a slightly higher pressure in the LPG port compared to the LPA port, the opposite being valid for the original model.

Figure VI.47 shows the temperature distribution over more than four cycles of operation. In terms of absolute values, the two models are comparable, both having the top temperature of about 1700K. When studying the distribution, it can be noticed that the new model has more hot gas penetration into the channels and also, it utilizes the whole length of the LPG port to scavenge the hot gas. This difference is attributed to the lack of geometry optimization in the case of the new design.

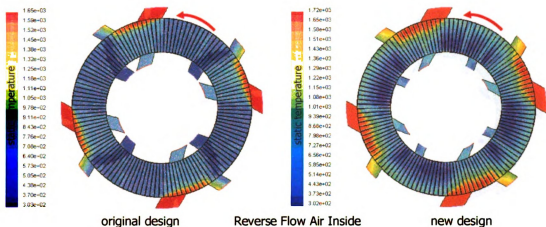


Figure VI.47: Static temperature distribution for the RFAI models, [K].

But when studying the Mach number distribution (Figure VI.48), a 20% decrease in the Mach number of the flow is observed for the new design model. That means the flow velocities are smaller through the channels (considering almost matching temperatures distribution), which in turn deliver slower flow to the ports and other components. One can conclude that the process will be less efficient, but complete efficiency evaluations could not be performed without investigations of the full thermodynamic system.

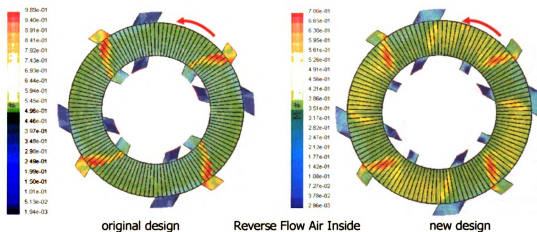


Figure VI.48: Mach number distribution for the RFAI models.

### VI.5.3 Comparison of Radial Configurations

To better study the performance of the wave rotor and to compare the three radial configurations (through-flow, reverse-flow with air ports at the inner part, and reverse-flow with gas ports at the inner part), a series of graphs representing pressure, temperature, and Mach number along the inner and outer circumference of the disc have been extracted.

The values at the middle of each channel opening have been plotted against the angle of the channel.

Figure VI.49 presents the pressure distributions along the inner and outer circumference for the three configurations. It can be easily noticed that the distribution is periodic over the four cycles. Thus, for clarity purpose, the following results will present only one cycle (0 to 90 degrees), like in Figure VI.50.

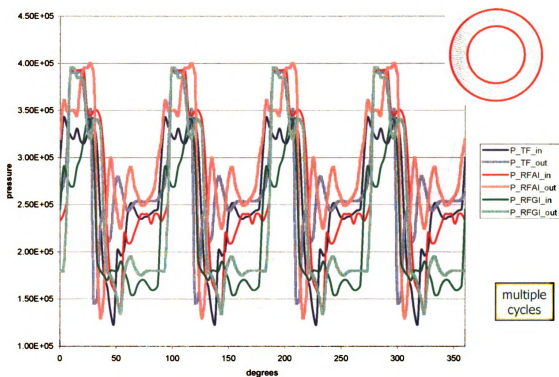


Figure VI.49: Pressure diagram for inner and outer circumference for the three configurations, [Pa].

In Figure VI.50, it is noticed that the pressure distribution is divided into a high and a low pressure part. To compare more effectively the three configurations, the pressure, temperature, and Mach number distributions were compared based on the location of the ports. Although the ports do not have the same length and location for all configurations, each graph was translated and scaled to the same length that is why there is no variable associated with the abscissa. The ordinate values of pressure, temperature, and Mach number are the exact values.

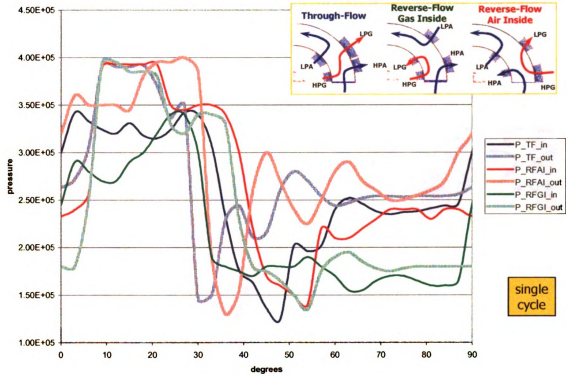


Figure I.10: Pressure diagram for inner and outer circumference displayed for one cycle only, [Pa].

Figure I.2 presents both gas ports for each configuration. The first conclusion that can be stated, is that the pressure in the HPG port for the RFAI configuration is the highest (Figure I.2-a) due to the centrifugal force that compresses the gas as it enters the channel. Studying this effect, it is expected that the Mach number should be the lowest for this configuration at the HPG port.

On the low pressure side, it can be seen that the pressure drop is stopped by the opening of the LPA port, soon after the opening of the LPG (Figure I.2-b). The RFGI configuration shows almost constant pressure distribution, the pressure drop being attenuated by the centrifugal forces effect.

RFGI configuration shows almost constant pressure distribution, the pressure drop being attenuated by the centrifugal forces effect.

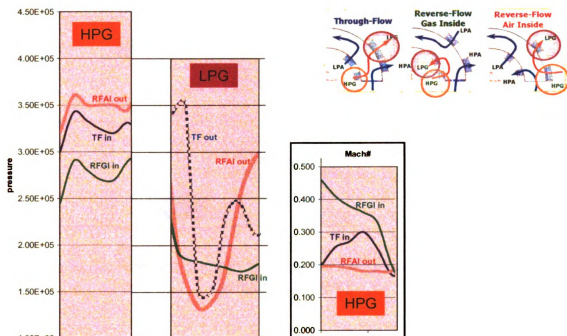


Figure VI.51: Pressure diagram for high and low pressure gas for the three configurations, [Pa].

On the air side (Figure VI.52) the HPA distribution is almost identical for all the configurations. That is an indication that pressure at these ports is not affected by the centrifugal effects, but the flow rate is. Studying the Mach number for the same port, it is noticed that RFGI shows the highest Mach number. Taking into consideration the fact the RFGI configuration has the lowest temperature (Figure VI.55-a), it results that it generates the highest flow rate for HPA.

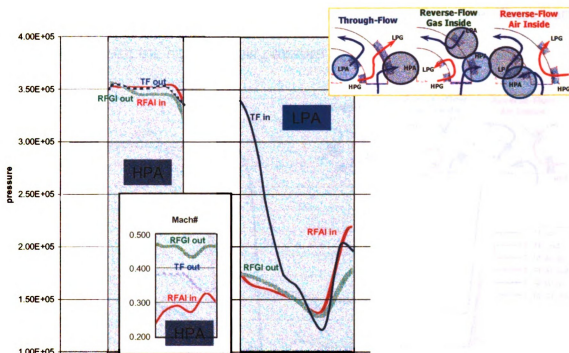


Figure VI.52: Pressure diagram for high and low pressure air for the three configurations, [Pa].

The pressure in the through-flow configuration for the LPA port has a lowest value (Figure VI.52-b) where the LPG port closes. An increase in pressure and a decrease in Mach number accompanies the LPG closing (Figure VI.56).

The temperature distribution of air ports shows, as expected, the highest values in the through-flow configuration (Figure VI.55), associated with the worst scavenging of hot flow.

Figure VI.53 shows the distribution of the temperature in all cases for a complete cycle. As for the pressure distribution in Figure VI.50, the temperature graphs



are divided into a high temperature part and a low temperature one. These parts are consistent with the high and low pressure zones.

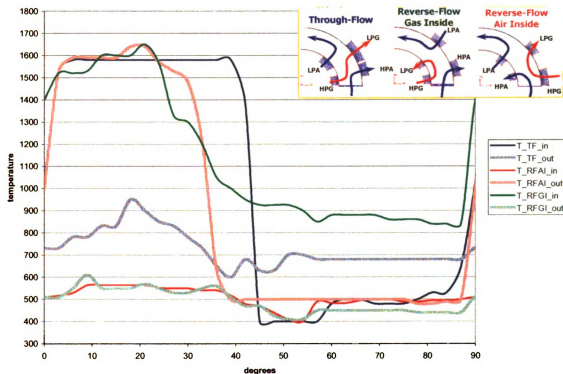


Figure VI.53: Temperature diagram for inner and outer circumference displayed for one cycle only, [K].

The HPG temperature has almost identical distributions for all cases, with a slower temperature rise in the case of RFGI (Figure VI.54-a). The RFGI scavenges the LPG at highest temperature (Figure VI.54-b), an effect that is beneficial for the air, which is scavenged at lowest temperature (Figure VI.55).

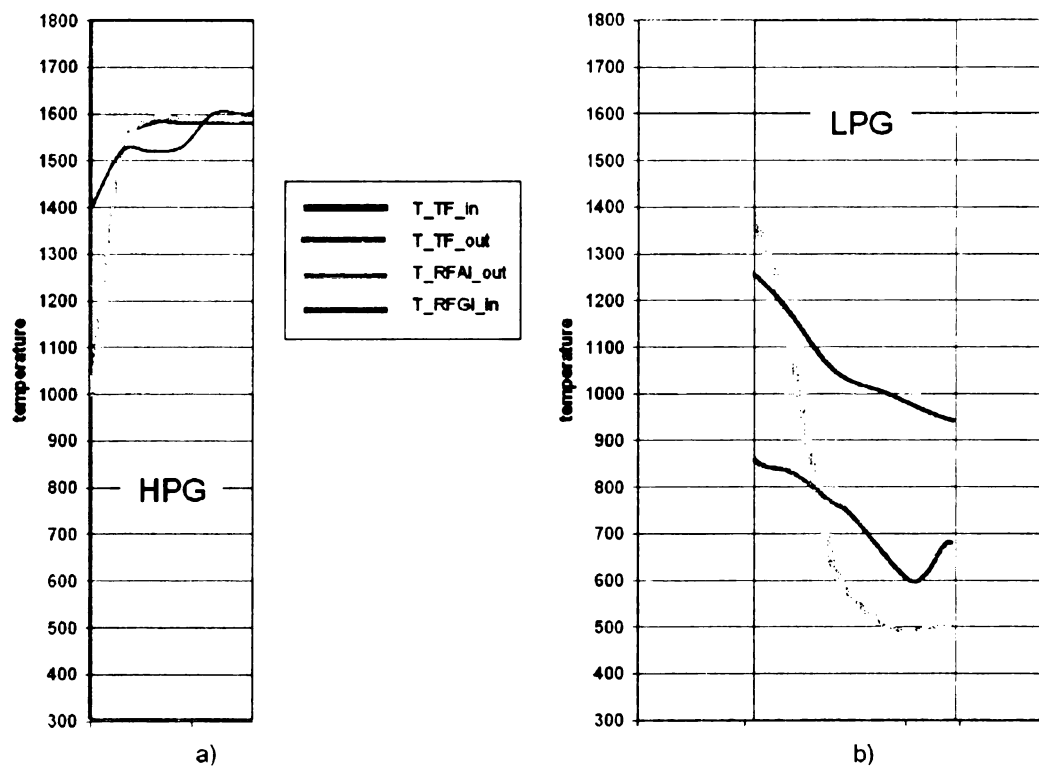


Figure VI.54: Temperature diagram for high and low pressure gas for the three configurations, [K].

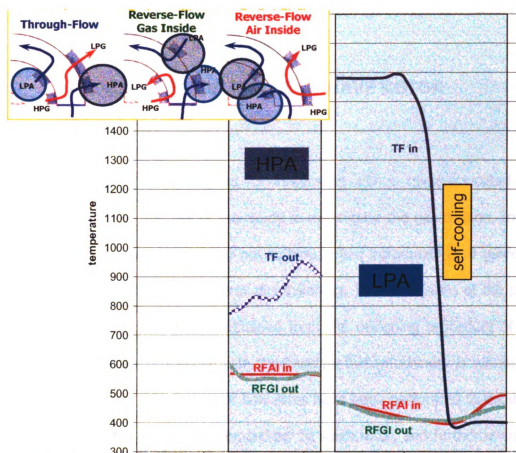


Figure VI.55: Temperature diagram for high and low pressure air, [K].

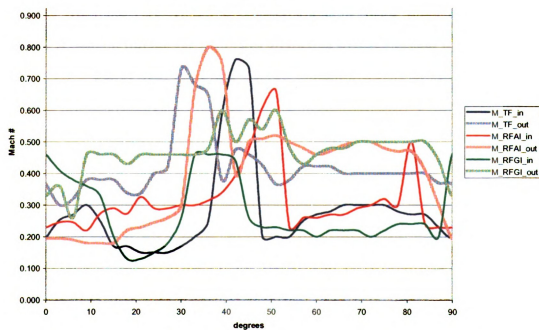


Figure VI.56: Mach number diagram for inner and outer circumference.

## **Chapter VII**

### **FINAL DESIGN OF THE U<sub>μ</sub>WAVE ROTOR**

Although the U<sub>μ</sub>WR was designed for integration with a microfabricated gas turbine, it is not the purpose of this study to investigate the gas turbine. In the final design of the wave rotor, the gas turbine is just introduced as a guideline for wave rotor positioning and overall dimensioning. The dimensions of the ports and ducts are exact dimensions obtained from the designing procedure of the wave rotor, but their connection with the baseline turbomachinery is schematic. Only some tentative calculations of flow rates have been performed to establish the geometry of the ducts from compressor to wave rotor, and further away, to the turbine.

Starting from the MIT H<sub>2</sub> Demo engine, the ultra-micro wave rotor has been designed, having the overall geometry adaptable to the baseline turbomachinery. This section will present some 3D renderings of the most important components of a wave rotor topped ultra-micro gas turbine. Although most of the components are going to be etched away in silicon wafers, these drawings present the negative part (mold) for clarity purposes.

First, the overall engine is presented in two isometric views and with the main components labeled (Figure VII.1). The design presented has a through-flow configuration, but similar designs can be constructed for reverse-flow configurations.

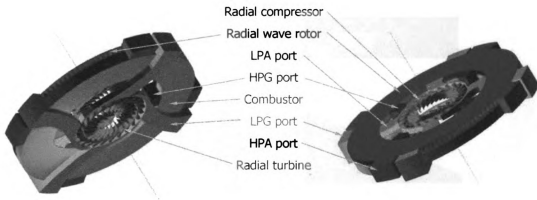


Figure VII.1: Full assembly of the wave rotor topped ultra-micro gas turbine.

Figure VII.2 shows several cross-sectional views of the final design. In these figures, the combustor, ports and ducts are shown as in the final product as cavities, compared to the previous set of figures where they are shown as negative.

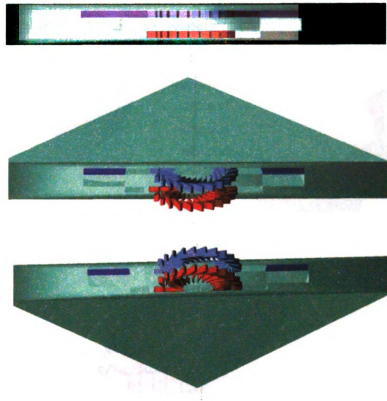


Figure VII.2: Cross-sectional views of the U $\mu$ GT unit.

Some details of each component are displayed in three pictures (grouped in the Figure VII.3). The wave rotor is placed at the same level as the radial compressor, surrounding it. From the compressor, ducts lead to the LPA ports of the wave rotor and on the internal part HPG ports where combustion gases come from the burner to the rotor. The combustion chamber has an annular shape and is placed directly beneath the wave rotor. The channels for fuel intake as well as the ignition system have not been included in this design. On the outer part of the rotor, the HPA and LPG ports take the air to the combustor and pre-expanded gases to the turbine, respectively. The turbine is placed at the interior

part, and its rotor is connected by a shaft to the rotor of the compressor (not shown).

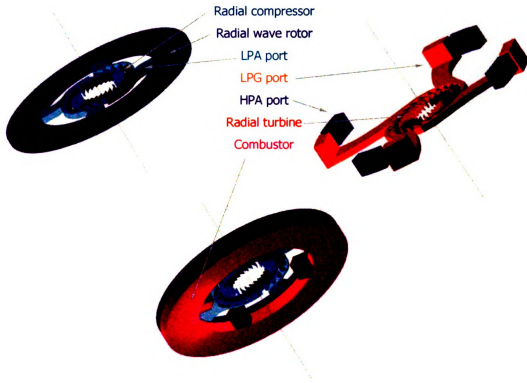


Figure VII.3: Partial assembly views of the U $\mu$ GT, showing different components.

The last figure in this section (Figure VII.4) explains graphically the directions of the two flows involved in the energy exchange process: the air and exhaust gas flows. The directions of the flows have been schematically superimposed on the top and bottom views of the U $\mu$ GT.

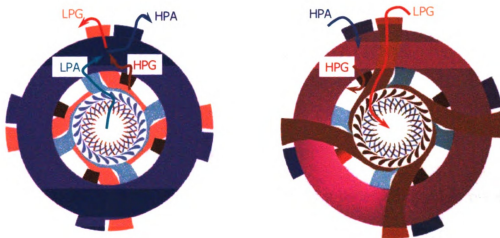


Figure VII.4: Top and bottom view of the U $\mu$ GT, showing also flow paths.



## **Chapter VIII**

### **EXPERIMENTAL INVESTIGATIONS**

#### **VIII.1 Axial Ultra-Micro Wave Rotor**

The rotor in the axial wave rotor configuration is a series of channels placed at the periphery of a spinning cylinder or disc. The fabrication process of these channels is vertical etching into a silicon wafer. Figure VIII.1 presents a computer rendering of the wave rotor model.

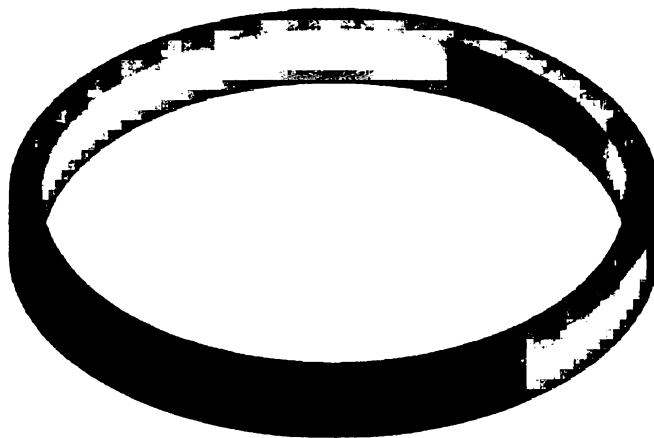


Figure VIII.1: Axial ultra-micro wave rotor.

The top and side cross-sectional views are displayed in Figure VIII.2.

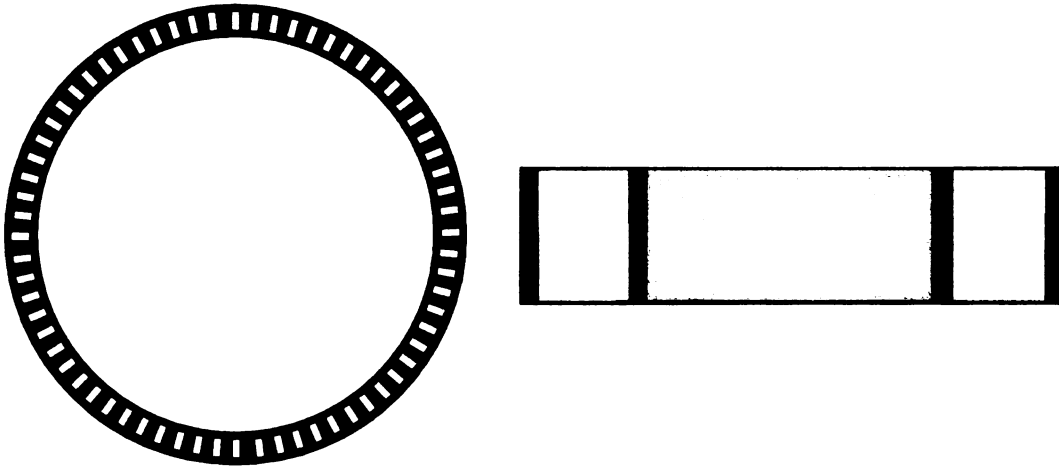


Figure VIII.2: Axial ultra-micro wave rotor: left – top view; right – cross-section.

The microfabrication process uses standard techniques for developing micro-electro-mechanical systems. It is a ten-step procedure using two photolithographic masks, one  $\text{SiO}_2$  etch step, and one deep reactive ion etching step. A schematic illustration of the process flow is shown in Figure VIII.3, below. The vertical scaling was highly exaggerated for clarity since the layers in the figures vary from  $1\mu\text{m}$  to  $500\mu\text{m}$ .

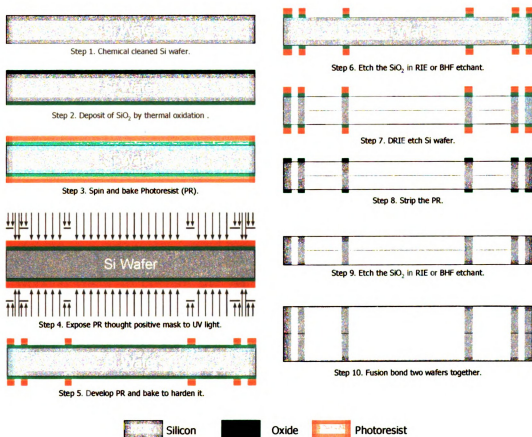


Figure VIII.3: Schematic process flow for microfabrication of axial wave rotor.

The process starts with a clean silicon wafer,  $500\mu\text{m}$  thick. On the wafer a  $1\mu\text{m}$  silicon oxide is deposited in a furnace at  $900\text{-}1200\text{ }^\circ\text{C}$ , that will help tailor the DRIE step. Through a photolithography process the oxide layer is patterned, following a  $250\mu\text{m}$  deep etching of silicon substrate (Ayon, Bayt et al. 2001). The photolithography process uses a  $10\mu\text{m}$  photoresist (PR) layer that is patterned by exposure to UV light through a positive mask. The mask (Figure VIII.4) is made of glass, and the pattern is formed by impregnating a thin metal film on the glass (Chromium or Gold). The photoresist is a polymer, whose chemical properties

change when exposed to radiation. The PR is commonly in a liquid phase that can be spun onto the silicon oxide layer at speeds of thousands of RPM's. The spinning process creates a uniform film thickness. After the application, the PR is baked at 90-100C to remove the solvents. Steps 1 to 9 target both faces of the wafer. Once the etching is completed and the channels are etched all the way through, the layers of  $\text{SiO}_2$  are stripped in a BHF solution. For wafer-through etching, a quartz wafer (called handling wafer) might need to be attached to the working wafer to prevent the wafer-back cooling Helium from leaking into the plasma chamber (Lin, Ghodssi et al. 1999). Two such wafers are prepared. Before aligned fusion bonding (Ayon, Zhang et al. 2003; Miki, Zhang et al. 2003), the two wafers are cleaned by ashing.



Figure VIII.4: Positive mask used in step 5 of axial wave rotor fabrication.

## VIII.2 Radial Ultra-Micro Wave Rotor

In a similar fashion, the radial ultra-micro wave rotor will be fabricated. The main difference lays in the fact that width/depth etch ratio is much higher for the radial rotor, and DRIE process is no longer required. The channels are going to be created by isotropic etching each half the width of the channels into a wafer and bond the two wafers in the end. Figures VIII.5 and VIII.6: show computers rendering of the rotor and two cross-sectional views (top and side).

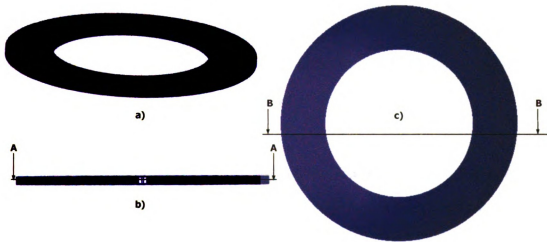


Figure VIII.5: Radial ultra-micro wave rotor: a) 3D view; b) side view; c) top view.

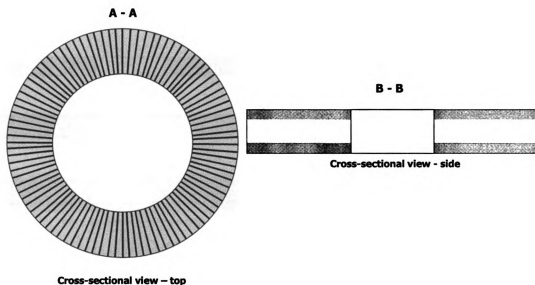


Figure VIII.6: Radial wave rotor: left – A-A cross-section (from Fig.5); right – B-B cross-section.

The microfabrication process starts with cutting the wafer out of the interior of the rotor, using the Laser MicroJet<sup>®</sup> cutting technique developed by The Gem City Engineering and Synova (Dushkina, Wagner et al.). For the radial wave rotor 250 $\mu$ m thick wafers are going to be used, and as the axial one, the rotor will be made out of two wafers fusion bonded together. Steps 3 to 7 are similar with the ones for the fabrication of axial wave rotor. The process is shown schematically in Figure VIII.7.

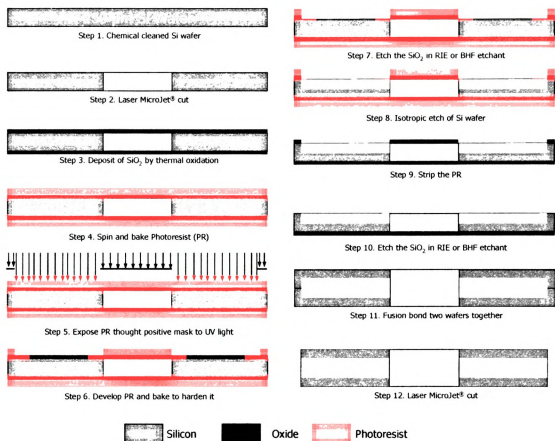


Figure VIII.7: Process flow for radial ultra-micro wave rotor fabrication.

The etching of the channels is going to be an isotropic etch, thus creating circular channels but with a larger cross-section on the outer diameter (Figure VIII.8).



Figure VIII.8: Radial wave rotor with rounded cross-sectional channels.

The last step involves cutting the outer edge of the wafer, which has not been etched, to reveal the outer opening of the channels. The mask used in step 5 is presented in Figure VIII.9.

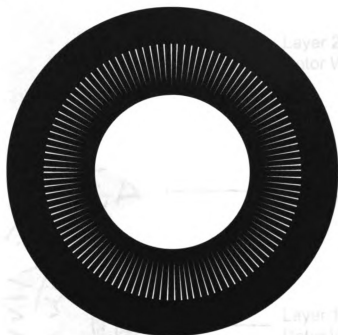


Figure VIII.9: Positive mask used in step 5 of radial wave rotor fabrication.

#### VIII.2.1 Fabrication of the Radial Wave Rotor Test Rig

The process flow for microfabrication of the radial wave rotor test rig uses four wafers and nine masks. The process follows the same procedure as described in section IX.1 and IX.2, but here it applies to both the rotor and the plenums and ports. The flow plenums are some cavities into which the fluid comes from external sources, is collected and its pressure raised to specifications and then directed to the wave rotor channels by means of ports.



Figure VIII.10 presents the exploded view of the rotor with the four etched layers of the two wafers, while Figure VIII.11 presents a similar view of the static part comprising plenums and ports.

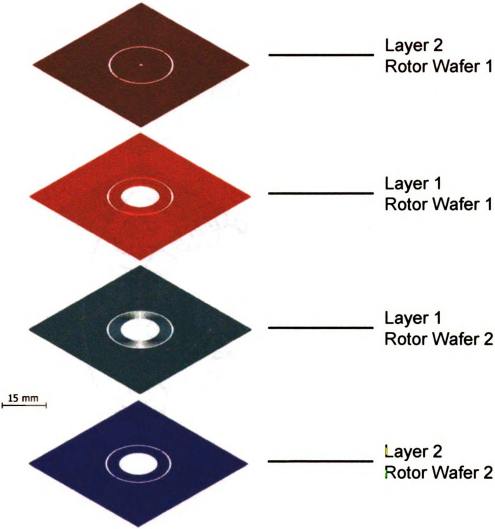


Figure VIII.10: Wafers used for rotor fabrication.

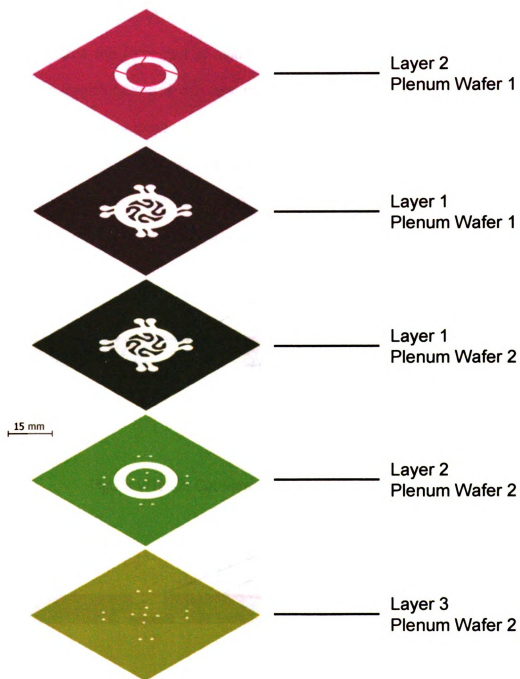


Figure VIII.11: Wafers used for ports and plenums fabrication.

Figures VIII.12 and VIII.13 present cross-sectional views of these parts. It can be seen that the rotor part is made out of 4 layers (each involving a different etch step and utilizing a different mask), 2 for each 500mm wafer, while the stationary part comprises 5 layers, 2 for the top wafer and 3 for the bottom wafer. The masks have alignment marks on them, under the form of etched rectangles, positive for one mask and negative for the other mask. The alignment marks are displayed in Figure VIII.15.

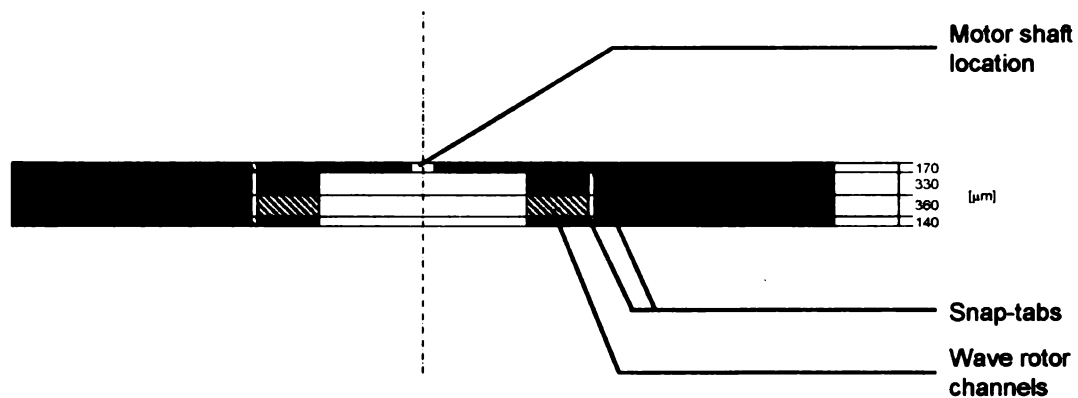


Figure VIII.12: Cut-view of the rotor wafers' assembly.

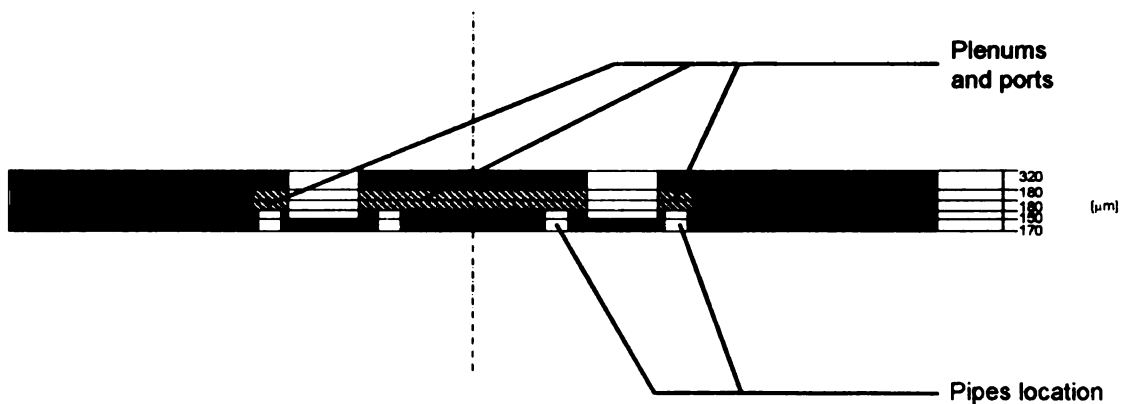


Figure VIII.13: Cut-view of the ports' and plenums' wafer assembly.

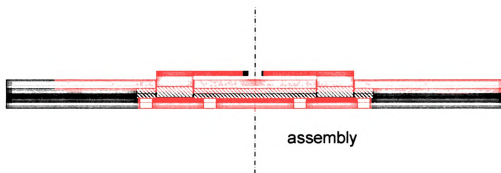


Figure VIII.14: Full wave rotor assembly.

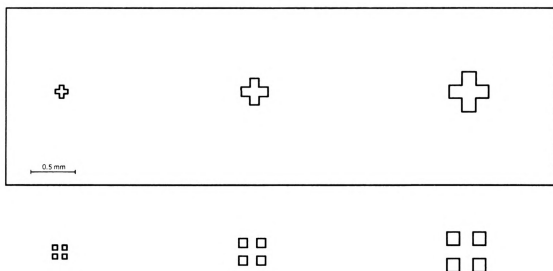


Figure VIII.15: Alignment marks – example.

Annex 2 presents the dimensions of the design as well as the masks used for each DRIE step.

### VIII.3 Single Channel Experiment

A single channel experiment has been developed to investigate the wave phenomenon inside a single wave rotor cell. The channel has a square cross-section with a  $360\mu\text{m}$  side length and  $3\text{mm}$  length. To be able to obtain more information, the channel was replicated at different scales on the same design matrix. Although the depth of the channel was maintained at  $360\mu\text{m}$ , the length and width was varied to  $90\times 750\mu\text{m}^2$ ,  $180\times 1500\mu\text{m}^2$ ,  $360\times 3000\mu\text{m}^2$ ,  $720\times 6000\mu\text{m}^2$ .

The process flow used in microfabricating the single channel test rig is described in Figure VIII.16. The process uses both a silicon and a glass wafer. Two glass masks are created for the two etch steps. One step creates the channels, while the other step creates the access holes for the tubing. The masks are shown in Figure VIII.17.

The glass wafer is bonded to the silicon wafer to close and insulate the channels.

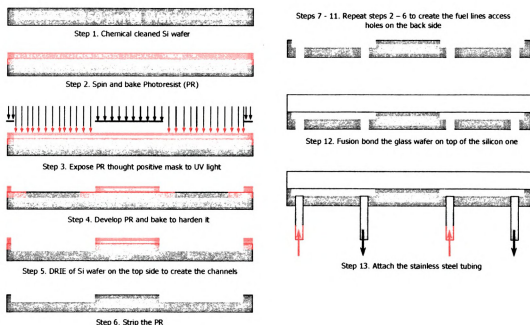


Figure VIII.16: Process flow for microfabrication of single channel test rig.

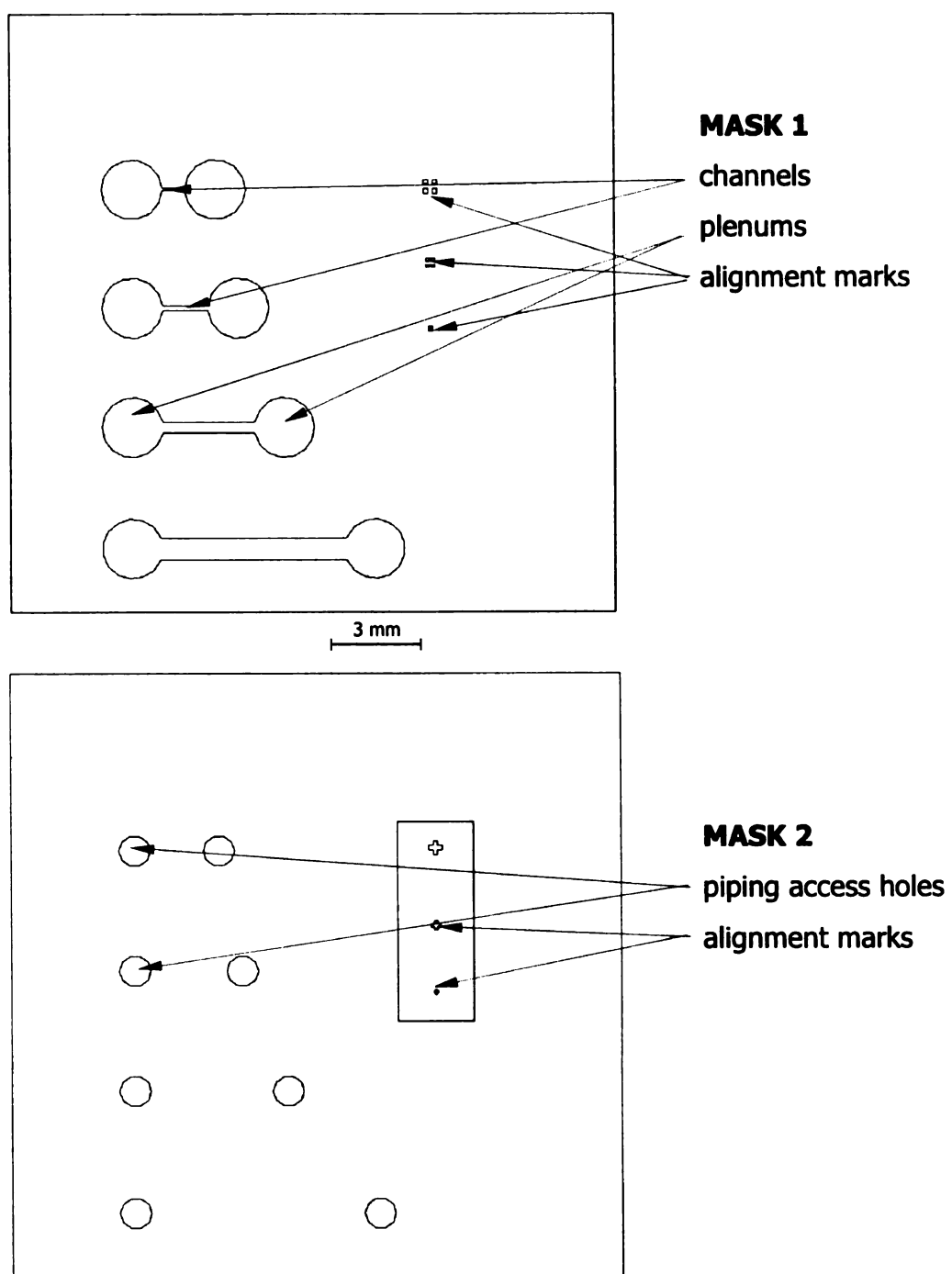


Figure VIII.17: Masks used for etching single channels.

Figure VIII.18 presents photos of the silicon/glass microfabricated dies. In the Figure VIII.18-a) an array of dies is displayed. Figures VIII.18-b) and VIII.18-c) present a single die – front side and back side. On the front side, the channels and the flow plenums can be observed. The quality of the geometry resulted from the microfabrication technique is impressive, allowing for clear view of the smallest channel ( $90\mu\text{m}$  in width). On the back side, the access holes for the flow pipes are precisely etched, and the alignment marks are also visible.

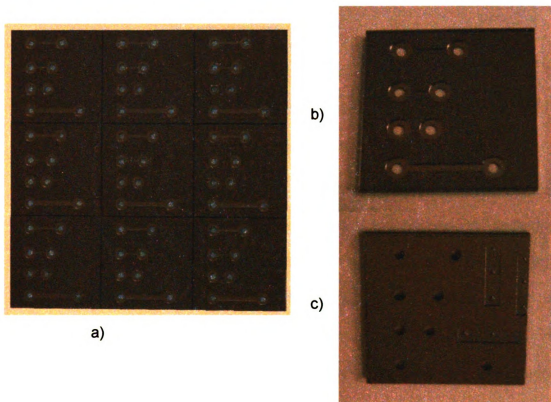


Figure VIII.18: Silicon microchannels: a) array of silicon dies; b) single die – front view; c) single die- back view.

When examining the die under an optical microscope, it can be seen that the geometry is accurate enough, errors varying from 1.3% to 95% (Figure VIII.19).

Part of this error is generated by the optical measurement of channels' width. Since the silicon is not transparent, reflection had to be used for visualizing the die instead of transmittance, and the walls generated some light interference, thus the walls looking blurry. Due to this an exact positioning of the side walls was not possible.

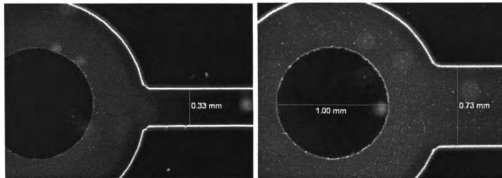


Figure VIII.19: Different size channels visualized with optical microscope.

This effect becomes more evident when trying to visualize the smallest channel, with a width of  $90\mu\text{m}$ . On a 5x magnification it looks like the ends of the channel are obstructed, but when magnifying to 20x, it can be seen that the light reflected from the chamfered edges between plenum and channel creates the distorted image (Figure VIII.20). The microscope used was an Olympus BH2 optical microscope equipped with a SPOT Camera (by Diagnostic Instruments Inc.).



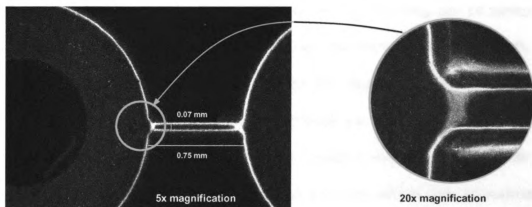


Figure VIII.20: Light reflection interference when visualizing silicon channels with optical microscope.

The next step was the Scanning Electron Microscope (SEM) imaging of the microfabricated channels. In Figure VIII.21 the four channels are photographed. With a small magnification factor the four channels appear to have very clean and well-defined geometry. In Figure VIII.21-a) the smaller channels are presented, while the larger ones are shown in Figure VIII.21-b).

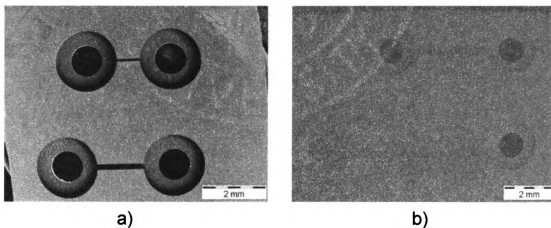


Figure VIII.21: Different size channels visualized with SEM: a) 90  $\mu\text{m}$  and 180  $\mu\text{m}$  wide channels; b) 360  $\mu\text{m}$  and 720  $\mu\text{m}$  wide channels.

Going to a higher magnification, the details of manufacturing can be observed. In Figure VIII.22-a) and c) it can be observed that the walls are not smooth, but wrinkles in the axis of the channel. This characteristic might affect the boundary layer of the flow through the channels, although the wrinkles are a few microns in height. In Figure VIII.22-b) a different aspect is noticed, that the walls are underetched. The lateral walls are deviated from the vertical with approximately  $20\mu\text{m}$  on the bottom (ie. an angle of 3 degrees), thus transforming the cross-sectional shape of the channels from rectangular to trapezoidal. Although this will not affect the microchannel measurements or the wave rotor performance, this aspects plays an important role for some of the turbomachinery components.

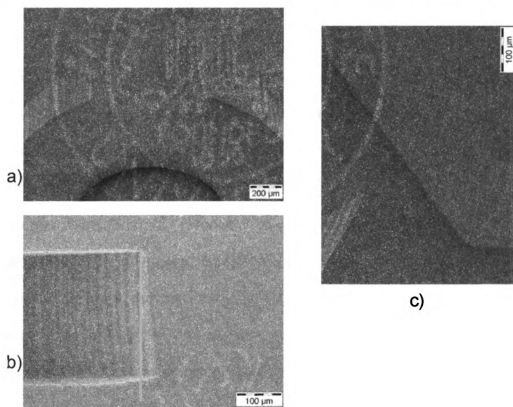


Figure VIII.22: Details of microfabrication of the silicon channel.

The great achievement of this fabrication process is the quality of the bonded structure. In Figure VIII.23, the bond between silicon and glass wafers is highlighted and it can be noticed that the bond is almost indistinguishable.

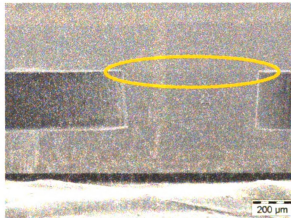


Figure VIII.23: Bond between silicon and glass wafers.

Last step of the manufacturing part was to create a bracket for handling the silicon die (chip). The bracket was created on the same system as the chip itself, based on a layer structure (Figure VIII.24-a). A 1mm thick aluminum plate was the middle layer (Figure VIII.24-b) that holds the waver from moving sideways. Two Plexiglas plates (5mm thick) restrain the chip from the top and bottom. The Plexiglas was used for its transparent property which allows for flow visualization equipment to be used. Further more, the bottom Plexiglas plate had a set of 2mm wide holes to allow the 1mm (outer diameter) flow pipes to be connected to the chip. The whole assembly is fastened with four screws, one in each corner.

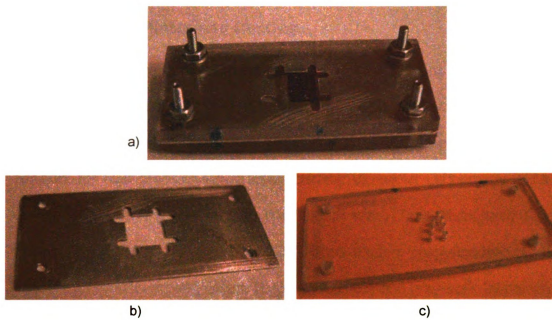


Figure VIII.24: Mounting bracket for the silicon chip: a) assembly; b) middle aluminum plate; c) bottom plate with access holes.

#### **VIII.4 End Plates and Ducting**

The rest of the wave rotor components, end plates and ducting will be designed as a function of the micro-turbomachinery to which the wave rotor will be integrated. The same processes will be applied to create these components. In addition, for high precision lithography, Extreme Ultraviolet Lithography (EUVL) can be used (Stulen), or for high depth/width ratio, Time Multiplexed Deep Etching (TMDE) (Ayon, Zhang et al. 2001). Other modern processes that can be used are directional etching (Ayon, Nagle et al. 2000) and gray-scale lithography (Waits, Morgan et al. 2005) that can create inclined surfaces or oblique channels. Drilling micron-size holes can be accomplished by Electrical Discharge Machining (EDM).

## **Chapter IX**

### **SUMMARY AND CONCLUSIONS**

#### **IX.1 Summary**

Given any ultra-micro gas turbine, using the information presented in this work, it is possible to find an optimum design point, where, by introducing the ultra-micro wave rotor and modifying the work load on the baseline engine, the topped gas turbine will operate at improved performance conditions. Calculations of wave rotor superior efficiency at microscale, as well as design schemes for wave diagrams, porting, wave rotor geometry, are presented. Also, detailed description of 2D wave rotor setup and investigations using CFD commercial code FLUENT are introduced. In the end, one configuration for final design and manufacturing process flow, fabrication steps are given. Incipient experimental investigations, as well as blueprints for a more complex test rig are also presented.

## **IX.2 Conclusions**

Utilizing a wave rotor to improve the performance of an U $\mu$ GT appears to be a promising solution. Even if the pressure ratio of the baseline engine is already optimized, the wave rotor can still enhance both the overall thermal efficiency and cycle specific work output if the wave rotor compression efficiency is higher than that of the baseline engine compressor. Adding a wave rotor also reduces the baseline compressor pressure ratio and the exit temperature of the compressor. Furthermore, this may reduce the compressor diameter and rotational speed, which results in reduced mechanical and thermal stresses and relaxed design constraints. From the manufacturing point of view, adding a wave rotor is much easier at microscale than at macro scale because the wave rotor can easily be etched in silicon due to its common extruded 2D shape. Additionally, in a regenerative way the wave rotor is able to harvest some of the significant amount of heat conducted away from the combustor through the structure, which is a severe problem for microfabricated gas turbines and also reduces the efficiency of the spool compressor severely.

Four possible designs for integrating a wave rotor in microfabricated gas turbines are introduced: three axial and one radial wave rotor. Based on documented wave rotor efficiencies at larger scale and subsidized by a gasdynamic model that includes wall friction, the wave rotor compression efficiency at microfabrication scale could be estimated with about 70%, which is much higher than the obtained efficiency of compressors in a microfabricated gas turbine. It is shown

that at such ultra-micro scale, the wave rotor can have the highest efficiency for shock wave pressure ratios in the range of  $1.7-2$ , assuming that the microfabrication can generate a smooth enough surface with a low friction coefficient. The results show that the efficiency depends not only on pressure gain across the shock wave traveling through the wave rotor channel but also depends highly on the loss coefficient for the channel geometry. According to the here employed model that is applicable for all wave rotor sizes, shorter wave rotor channels with larger diameter let expect a higher compression efficiency of the wave rotor.

Several innovative ideas and concepts have been introduced and investigated in the present dissertation. The most important one is the delivery of a viable solution for improving the performance of a ultra-micro gas turbine, by adding a miniaturized wave rotor. Second, for the first time, the variable efficiency compression process has been incorporated into wave rotor design space investigations. This sheds a new light on where, when and under what conditions the topping of gas turbines with wave rotors is efficient and desirable. Third, the concept of radial wave rotor (wave disc) is an important step forward for wave rotor technology. Its unique features can improve the compression process and/or flow scavenging, and also phase separation. The manufacturing process sounds is ideal for microfabrication. Being able to embed the compressor inside the wave discs, the overall dimensions can be reduced. Last, simulation of unsteady gas dynamic process inside the ultra-micro wave rotor channels using a



commercial CFD package is a first. FLUENT offers tools that allow for relatively easy preparation of geometries, some range of typical boundary conditions, relatively fast and robust solvers and a wide range of post-processing which are valuable tools for engineers beside scientists. Using FLUENT it has been shown extensively that such tools can be effectively used for simulation of rather complex time dependent flow phenomena that occur typically in wave rotors.

### **IX.3        Suggestions for Future Work**

#### **IX.3.1 Wave Disc with Curved Channels**

Reduction of the wave disc diameter can be obtained by the use of curved or spiral channels. Curving the channel allows for modulating the acceleration in flow direction because the component of the centrifugal force that is tangential to the path of the fluid motion affects the fluid acceleration. Thus, the channel shape, which may be easier to modify in a wave disc configuration, is another parameter that should be taken into account for a proper wave disc design. To fully realize the unsteady flow phenomena occurring inside rotor channels, the channel length to width ratio should be a large value (e.g., 6-10). This requirement influences the dimensions of the wave disc. Figure IX.1 presents a possible configuration of a radial wave rotor in a reverse-flow configuration with curved channels, and Figure IX.2 presents a 3D rendering of such a rotor.

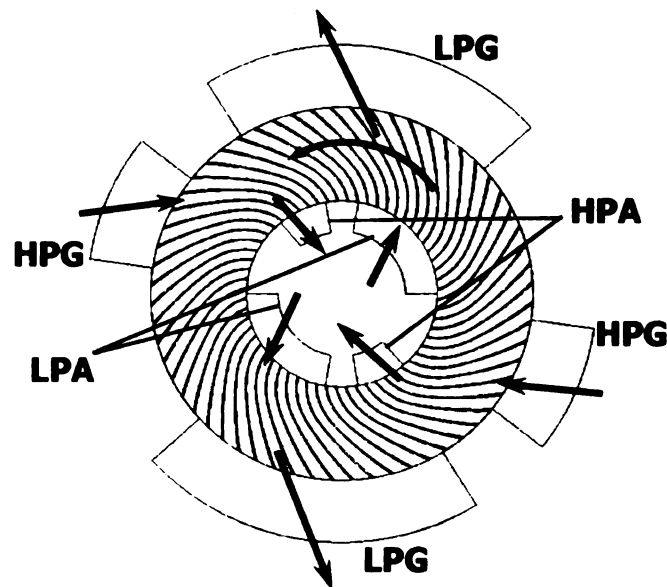


Figure IX.1: Wave disc with curved channels – ports schematic.

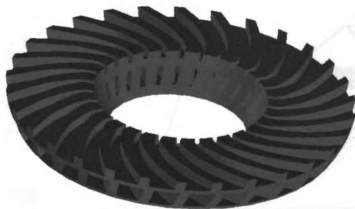


Figure IX.2: Wave disc with curved channels – 3D rendering.

### IX.3.2 Optimization of the Thermodynamic Parameters

Using the newly available design space for ultra-micro gas turbines, baseline and topped with wave rotors, points in this domain can be found for optimum design performance. These optimum points, from the thermodynamic point of view, can be incorporated as input for the wave rotor design scheme. Then, through geometry and port timing iterations (as described in Chapters V and VI), the best solution, from mechanical point of view, can be found.

### IX.3.3 Experimental Testing

A new, simplified, design for a ultra-micro wave rotor test rig is presented in the end of this work. This design uses only two silicon wafers for the whole setup

(both rotational and stationary part) and only two masks for etching. The masks as well as the cross-sectional assembly are displayed next.

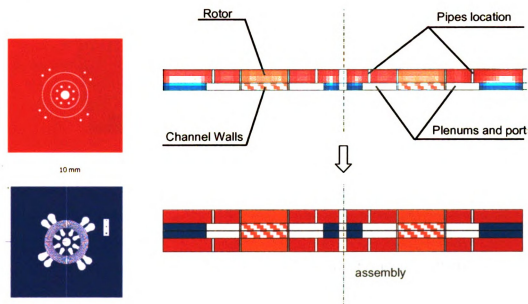


Figure IX.3: Simplified ultra-micro wave rotor test rig.

### IX.3.4 3D CFD Investigations

Since the regular 3D CFD models are difficult to investigate, not to mention extremely time and resource consuming, the author proposes building “quasi-3D” mesh models, as presented next. The models account for a two-dimensional mesh and elements arranged into a three-dimensional geometry. The following figure displays the concept of the single channel test setup, having one of the reservoirs (plenums) out of plane with the channel.

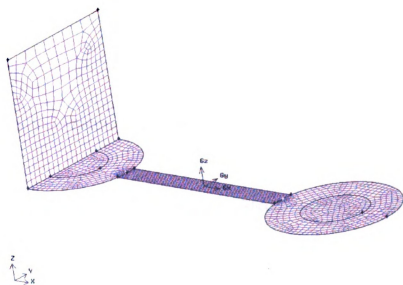


Figure IX.4: Quasi 3D mesh model for 3D CFD investigations.

## Appendices

### Appendix 1 – Material Properties

Table A.1: Properties of Silicon <1 0 0>

Si <1 0 0> properties	Value
elasticity modulus, $E$	130 GPa
Poisson's ration, $\nu$	0.28
density, $\rho$	2320 Kg/m <sup>3</sup>
thermal expansion coefficient, $\alpha$	2.33·10 <sup>-6</sup> 1/K @ 300K
	4·10 <sup>-6</sup> 1/K @ 1000K
thermal conductivity, $k$	98.9 W/m·K @ 400 K
	31.2 W/m·K @ 1000 K
specific heat, $c_p$	700 J/kg·K
thermal conductivity, $k$	157 W/m K
heat transfer coefficient, $h$	24 kW/m <sup>2</sup> ·K - 10 MW/m <sup>2</sup> ·K
failure stress, $\sigma_f$	1.1 – 3.4 GPa

(Tuckerman and Pease 1981; Kovacs 1998; Mehra, Waitz et al. 1999; Kang, Chen et al. 2002; [www.efunda.com](http://www.efunda.com) 2005)

Table A.2: Properties of Silicon Carbide

SiC (hot-pressed) properties	Value
elasticity modulus, $E$	450 GPa
Poisson's ration, $\nu$	0.14
density, $\rho$	2550 Kg/m <sup>3</sup>
thermal expansion coefficient, $\alpha$	$4.5 \cdot 10^{-6}$ 1/K
thermal conductivity, $k$	55 W/m K
heat transfer coefficient, $h$	24 kW/m <sup>2</sup> ·K - 10 MW/m <sup>2</sup> ·K
failure stress, $\sigma_f$	1.1 – 3.4 GPa

(Stark 1999)

Table A.3: Properties of Silicon Nitride

Si <sub>3</sub> N <sub>4</sub> (hot-pressed) properties	Value
elasticity modulus, $E$	310 GPa
Poisson's ration, $\nu$	0.27
density, $\rho$	3290 Kg/m <sup>3</sup>
thermal expansion coefficient, $\alpha$	$3.3 \cdot 10^{-6}$ 1/K
thermal conductivity, $k$	30 W/m K

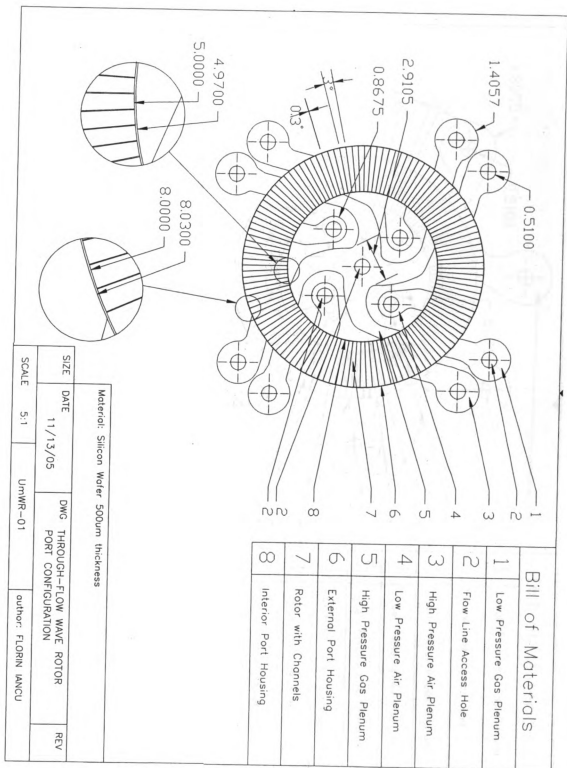
(www accuratus.com 2005)

## **Appendix 2 – U<sub>μ</sub>WR Fabrication Drawings**

Figure A.5: Technical drawing of the ultra-micro wave rotor in a through-flow configuration.

Figure A.6: Technical drawing of the ultra-micro wave rotor in a reverse-flow configuration with air ports placed on the inside region.





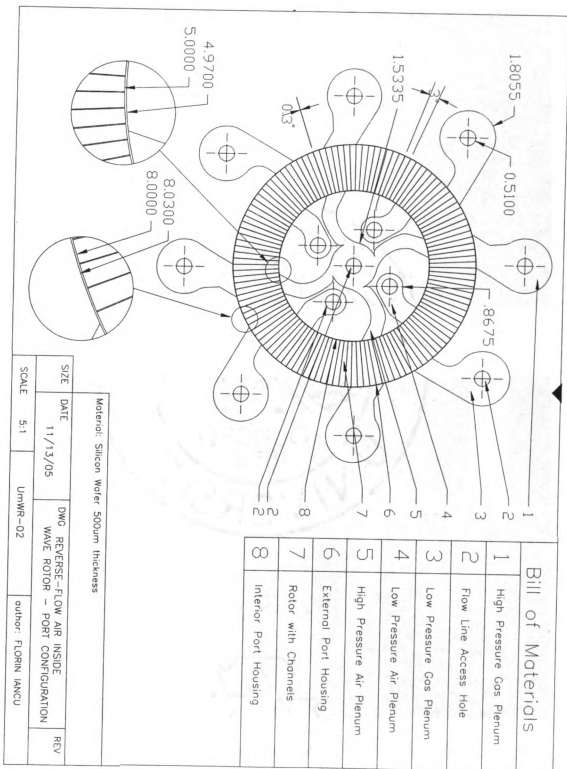




Figure A.7: Mask used for first etch step of rotor wafer 1.

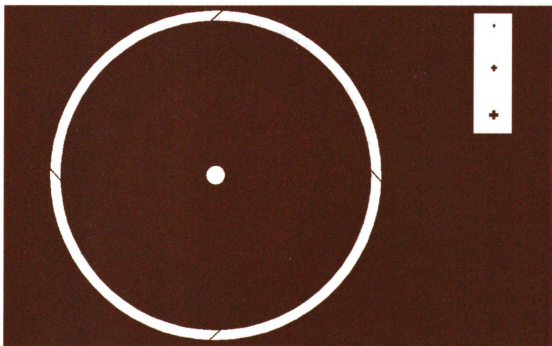


Figure A.8: Mask used for second etch step of rotor wafer 1.

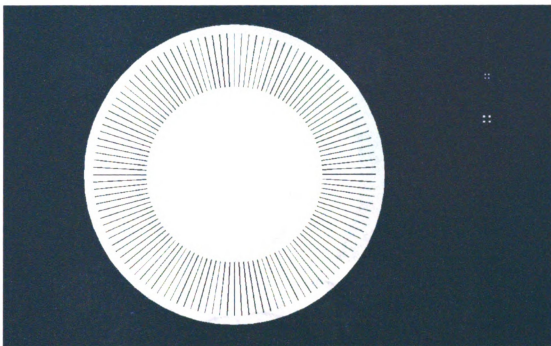


Figure A.9: Mask used for first etch step of rotor wafer 2.

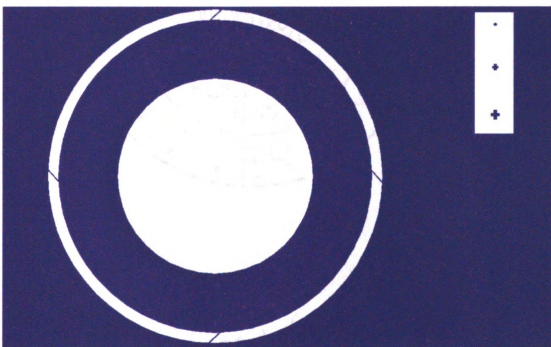


Figure A.10: Mask used for second etch step of rotor wafer 2.

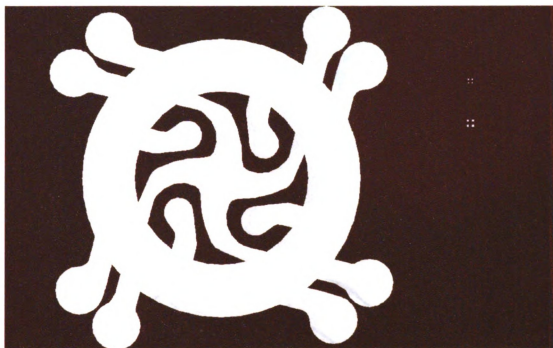


Figure A.11: Mask used for first etch step of plenum wafer 1.

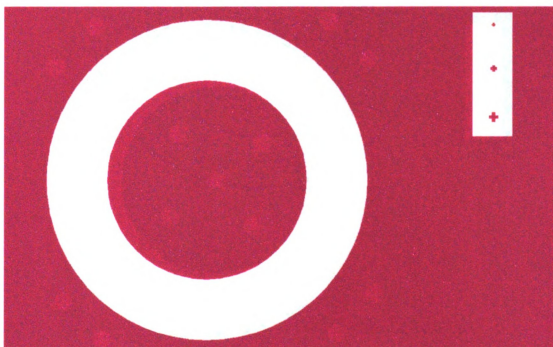


Figure A.12: Mask used for second etch step of plenum wafer 1.



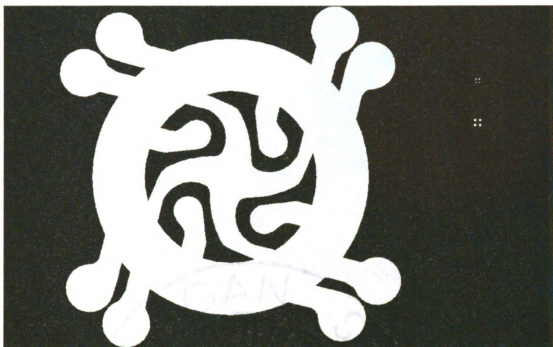


Figure A.13: Mask used for first etch step of plenum wafer 2.

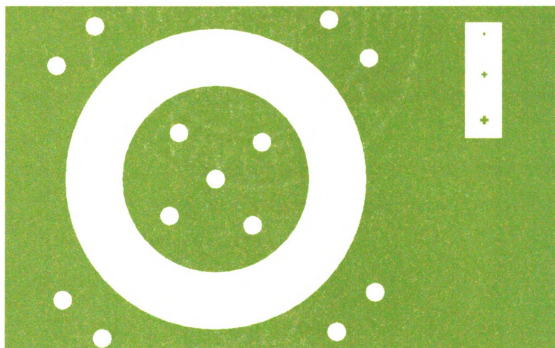


Figure A.14: Mask used for second etch step of plenum wafer 2.

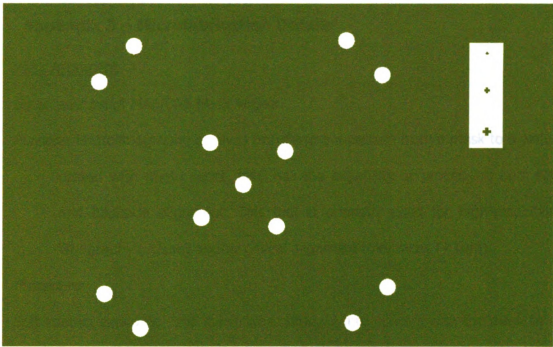


Figure A.15: Mask used for third etch step of plenum wafer 2.



## **Appendix 3 – Microfabrication Details<sup>3</sup>**

### **Mask Alignment**

*Equipment used:* MA6/BA6 Mask Aligner

*Purpose:* Photolithography involves transferring a pattern from a mask to a wafer coated with photo resist. MA6 has the capability of processing both top and backside alignment. This tool is primarily used for high-resolution lithography ( $<2\mu\text{m}$ ) and/or critical alignment tolerances ( $<1\mu\text{m}$ ).

*Procedure:*

Soft contact exposure - the substrate is brought into contact with the mask by a preset force during exposure, for features  $\geq 2\mu\text{m}$ .

Flood Exposure: for first level exposure. Once the mask and wafer are loaded the aligner proceeds to expose skipping the alignment step.

### **Alignment Features**

Top side: TSA, the top microscope is used to align mask features to the topside of the wafer.

Back side: BSA, the bottom objectives are used to align mask features to the back of the wafer. This is achieved by aligning a captured image of the mask and the real image of the wafer.

Mask Clean - Dip in Acetone/ IPA #1/ IPA #2 and  $\text{N}_2$  dry.

---

<sup>3</sup> Material extracted from the University of Michigan, WIMS Laboratory – Lab notebooks.

Photo Resist - Positive resist (Any resist exposed to ultra-violet light is developed away) and Negative resist (Resist remains on the surface where exposed).

Lamp Power Supply: 405nm (20 mW/cm<sup>2</sup>) and 365nm (11mW/ cm<sup>2</sup>)

Configuration: MA6 for lithography/BA6 is for bonding alignment.

The alignment marks are used to ensure each mask step fits on top of the previous step. If anything is misaligned you have the chance for devices to fail.

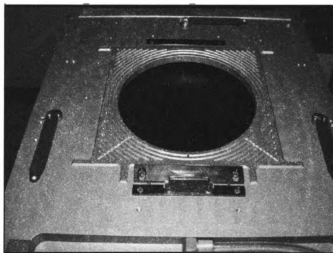


Figure A.16: MA6/BA6 Mask Aligner - mask tray.

### Deep Reactive Ion Etching

*Equipment used:* STS Etch System

*Purpose:* It is a deep reactive etch (DRIE) system that uses SF<sub>6</sub> for etching and C<sub>4</sub>F<sub>8</sub> for passivation.

*Procedure:*

Carrier Wafer Bonding: For any substrate etched more than 250 $\mu$ m deep, shall be bonded to a carrier wafer.

Chiller temperature between 40°C and 45°C to start the process.

Turbo rotational velocity - 3600rpm.

The process consists of two steps: one is an isotropic etch using SF<sub>6</sub> high density plasma, the other is a passivation step in which the wafer is covered is covered with a C<sub>4</sub>F<sub>8</sub> film. Ion bombardment removes preferentially the passivation film from the horizontal surfaces, allowing these surfaces to be isotropic etched, thus creating anisotropic geometries.

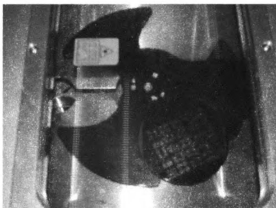


Figure A.17: Wafer holder for etching.

Bonding

*Equipment used:* SB6 Bonder

*Purpose:* The SB6 is used for anodic, diffusion and thermal/compression bonding of 4-inch substrates.

*Procedure:*

Following materials are allowed in the system, besides silicon wafers: tin, indium or solder, glass, BoroFloat, Pyrex, borosilicate glass with thermal characteristics to silicon wafers.

Compressed air: 6-10 bar

Vacuum: 90-95 mbar

Inert Gas: N<sub>2</sub> at 1.1 –10 bar

Room temperature: 20-22C

Temperature inside the chamber: 100C to 550C

Humidity: 40-45%

Silicon Direct Bonding, Fusion Bond is used to join two silicon wafers by creating a hydrophobic or hydrophilic surface. (Hydrophobic: an HF dip is advisable for a better bond; Hydrophilic: a standard RCA clean is required)

Bond Chamber is designed for processing pressures from  $5 \cdot 10^{-5}$  mbar to 3 bar (absolute). Voltage: -2000V to + 2000V possible, change the polarity as required for bonding.

Dicing

*Equipment used:* Micro Automation Dicing Saw

*Purpose:* The dicing saw is used to separate dies from the wafer. A specified blade (dependant on substrate type) cuts the scribes lines in the x and y direction.

*Procedure:*

The wafer is temporarily placed on an adhesive film to hold it on a vacuum chuck.

The wafer is marked for cutting. It is important to know the width of streets (scribe lines), thickness of cut and location of alignment marks.

Cleavage Plane: {100} wafers, natural cleavage planes exist perpendicular to the surface of the wafer in the directions parallel and perpendicular to the wafer flat. {111} wafers, a vertical cleavage plane runs parallel to the wafer flat.

Types of Blades: The grit size of a blade is dependant on material to be cut.

Blade 777 is used to cut glass or silicon, the cut width is 230um (9.05mils). Blade 42525 is used only to cut silicon, the cut width is 110um (4.33mil).

Thickness of the wafers: Silicon wafer: 24mils for 4 inch (500-550um). Glass wafer: 33.5 mils. Adhesive film: 3.5 to 4 mils.

Cutting Speed: Silicon – 100, Glass - 50

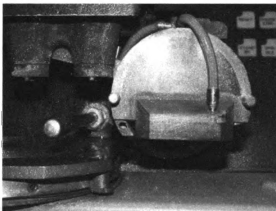


Figure A.18: Wafer dicing saw.

## References

- Akbari, P. (2004). Performance Prediction and Preliminary Design of Wave Rotors Enhancing Gas Turbine Cycles, Mechanical Engineering, Michigan State University, East Lansing.
- Akbari, P. and N. Müller (2003). Performance Improvement of Small Gas Turbines Through Use of Wave Rotor Topping Cycles. 2003 International ASME/IGTI Turbo Exposition, GT2003-38772.
- Akbari, P. and N. Müller (2003). Performance Investigations of Small Gas Turbine Engines Topped with Wave Rotors. 39th AIAA/ASME/SAE/ASEE Joint Propulsion Conference, Huntsville, AL, AIAA2003-4414.
- Akbari, P., N. Müller, et al. (2003). Utilizing Wave Rotor Technology to Enhance the Turbo Compression in Power and Refrigeration Cycles. ASME International Mechanical Engineering Congress & Exposition, Washington, DC, IMECE2003-44222.
- Akbari, P., M. R. Nalim, et al. (2004). A Review of Wave Rotor Technology and Its Applications. 2004 International Mechanical Engineering Conference, IMECE2004-60082.
- Anderson, J. D. (2003). Modern Compressible Flow With Historical Perspective. New York, NY, McGraw-Hill.
- Ayon, A. A., R. L. Bayt, et al. (2001). "Deep Reactive Ion Etching: A Promising Technology for Micro- and Nanosatellites." Smart Materials and Structures 10: 1135-1144.
- Ayon, A. A., S. Nagle, et al. (2000). "Tailoring Etch Directionality in a Deep Reactive Ion Etching Tool." Journal of Vacuum Science & Technology B 18(3): 1412-1416.
- Ayon, A. A., X. Zhang, et al. (2001). "Anisotropic Silicon Trenches 300-500  $\mu\text{m}$  Deep Employing Time Multiplexed Deep Etching (TMDE)." Sensors and Actuators A 91: 381-385.
- Ayon, A. A., X. Zhang, et al. (2003). "Characterization of Silicon Wafer Bonding for Power MEMS Applications." Sensors and Actuators A 103: 1-8.
- Azim, A. (1974). An Investigation Into the Performance and Design of Pressure Exchangers, Ph.D. Dissertation, University of London., London, UK.

- Azoury, P. H. (1965). "An Introduction to the Dynamic Pressure Exchanger." Proceedings of the Institution of Mechanical Engineers 180, Part 1(18): 451-480.
- Azoury, P. H. (1992). Engineering Applications of Unsteady Fluid Flow. New York, John Wiley and Sons.
- Azoury, P. H. and S. M. Hai (1975). "Computerized Analysis of Dynamic Pressure Exchanger Scavenge Processes." Proceedings of the Institution of Mechanical Engineers 189: 149-158.
- Barbour, E. A., R. K. Hanson, et al. (2005). A Pulsed Detonation Tube with a Converging-Diverging Nozzle Operating at Different Pressure Ratios. The 43rd AIAA Aerospace Sciences Meeting and Exhibit, Reno, NV, AIAA-2005-1307.
- Brillouin, L. (1938). "On Thermal Dependence of Elasticity in Solids." Physical Review 54: 916-917.
- Brouillette, M. (2003). "Shock Waves at Micro Scale." Shock Waves 13: 3-12.
- Cauley, T. H. I., J. D. Rosario-Rosario, et al. (2004). Feasibility Study of a MEMS Viscous Rotary Engine Power System (VREPS). 2004 ASME International Mechanical Engineering Congress & Exposition, Anaheim, CA, IMECE2004-59916.
- Choi, S. B., R. F. Barron, et al. (1991). "Fluid Flow and Heat Transfer in Microtubes." ASME DSC Micromechanical Sensors, Actuators and Systems 32: 123-134.
- Courant, R., K. Friedrichs, et al. (1928). "Über die Differenzengleichungen der Mathematischen Physik." Mathematische Annalen 100: 32-74.
- Courant, R., K. Friedrichs, et al. (1967). "On the Partial Difference Equations of Mathematical Physics." IBM Journal of Research and Development 11: 215-234.
- DeCourtye, D., M. Sen, et al. (1998). "Analysis of Viscous Micropumps and Microturbines." International Journal Of Computational Fluid Dynamics, 10: 13-25.
- Dempsey, E., P. Akbari, et al. (2005). Optimum Applications of Four-Port Wave Rotors for Gas Turbine Enhancement. 17th International Symposium on Airbreathing Engines, Munich, Germany, ISABE-2005-1214.

- Dessornes, O., C. Dumand, et al. (2003). Micro Combustion Chambers Principles Dedicated to Micro-Turbines. Power MEMS,
- Doerfler, P. K. (1975). "Comprex Supercharging of Vehicle Diesel Engines."
- Dushkina, N. M., F. R. Wagner, et al. (2002). Free-Shape Cutting of Thin Semiconductor Wafers with Synova Laser MicroJet(R). Dayton, OH, Lausanne, Switzerland, The Gem City Engineering Co. and SYNOVA SA.
- Edwards, D. H., D. R. Brown, et al. (1970). "The Influence of Wall Heat Transfer on the Expansion Following a C-J Detonation Wave." Journal of Physics D: Applied Physics 3.
- Eidelman, S. (1984). The Problem of Gradual Opening in Wave Rotor Passages. 19th Intersociety Energy Conversion Engineering, San Francisco, CA,
- Eidelman, S. (1985). "The Problem of Gradual Opening in Wave Rotor Passages." Journal of Propulsion and Power 1(1): 22-28.
- Eidelman, S. (1986). Gradual Opening of Rectangular and Skewed Wave Rotor Passages. ONR/NAVAIR Wave Rotor Research and Technology Workshop, Naval Postgraduate School, Monterey, CA., NPS-67-85-008.
- Eidelman, S. (1996). "Gradual Opening of Skewed Passages in Wave Rotors." Journal of Propulsion and Power 2(4): 379-381.
- Eidelman, S., W. Grossmann, et al. (1991). "Review of Propulsion Applications and Numerical Simulations of the Pulsed Detonation Engine Concept." Journal of Propulsion and Power 7(6): 857-865.
- Eidelman, S., A. Mathur, et al. (1984). "Application of Riemann Problem Solvers to Wave Machine Design." AIAA Journal 22(7): 1010-1012.
- Eldin, H. A. N. and H. Oberhem (1993). Accurate Animation of the thermo-fluidic Performance of the Pressure Wave Machine and its Balanced Material Operation. 8th International Conference on Numerical Methods in Laminar and Turbulent Flow, UK,
- Eldin, H. A. N., H. Oberhem, et al. (1987). The Variable Grid-Method for Accurate Animation of Fast Gas Dynamics and Shock-Tube Like Problems. IMACS/IFAC International Symposium on Modeling and Simulation of Distributed Parameter Systems, Japan,
- Elloye, K. J. and J. Piechna (1999). "Influence of the Heat Transfer on the Operation of the Pressure Wave Supercharger." The Archive of Mechanical Engineering 46(4): 297-309.



- Epstein, A. H. (2003). Millimeter-Scale, MEMS Gas Turbine Engines. ASME Turbo Expo 2003, Atlanta, GA, GT-2003-38866.
- Epstein, A. H. (2004). "Millimeter-Scale, Micro-Electro-Mechanical Systems Gas Turbine Engines." Journal of Engineering for Gas Turbines and Power 126: 205-226.
- Epstein, A. H., A. A. Ayón, et al. (1997). Micro-Heat Engines, Gas Turbines, and Rocket Engines - The MIT Microengine Project. 28th AIAA Fluid Dynamics Conference, Snowmass Village, CO, AIAA Paper 97-1773.
- Epstein, A. H., S. A. Jacobson, et al. (2000). Shirtbutton-Sized Gas Turbines: The Engineering Challenges of Micro High Speed Rotating Machinery. 8th International Symposium on Transport Phenomena and Dynamics of Rotating Machinery, Honolulu, Hawaii,
- Epstein, A. H., S. D. Senturia, et al. (1997). Power MEMS and Microengines. IEEE Transducers '97 Conference, Chicago, IL,
- Fatsis, A. and Y. Ribaud (1997). Numerical Analysis of the Unsteady Flow Inside Wave Rotors Applied to Air Breathing Engines. 13th International Symposium on Air Breathing Engines, Chattanooga, TN, AIAA, ISABE-97-7214.
- Fatsis, A. and Y. Ribaud (1998). "Preliminary Analysis of the Flow Inside a Three-Port Wave Rotor by Means of a Numerical Model." Aerospace Science and Technology, 2(5): 289-300.
- Fatsis, A. and Y. Ribaud (1999). "Thermodynamic Analysis of Gas Turbines Topped with Wave Rotors." Aerospace Science and Technology(5): 293-299.
- Fluent, I. (2003). Fluent 6.1 User Manual.
- Frechette, L., C. Lee, et al. (2004). Development of a MEMS-Based Rankine Cycle Steam Turbine For Power Generation: Project Status. 4th International Workshop on Micro and Nano Technology for Power Generation & Energy Conversion Applications (Power MEMS'04), Kyoto, Japan,
- Frechette, L. G. (2000). Development of a Microfabricated Silicon Motor-Driven Compression System, Ph.D. Dissertation, Mechanical Engineering, Massachusetts Institute of Technology, Cambridge, MA.
- Frechette, L. G. (2001). Assessment of Viscous Flows in High-Speed Micro Rotating Machinery For Energy Conversion Applications. 2001 ASME

International Mechanical Engineering Congress and Exposition, New York, NY,

Frechette, L. G., S. A. Jacobson, et al. (2000). Demonstration of a Microfabricated High-Speed Turbine Supported on Gas Bearings. Solid-State Sensor and Actuator Workshop, Hilton Head Is., SC,

Frechette, L. G., S. A. Jacobson, et al. (2005). "High-Speed Microfabricated Silicon Turbomachinery and Fluid Film Bearings." Journal of Microelectromechanical Systems 14(1): 141-152.

Greendyke, R. B., D. E. Paxson, et al. (2000). "Dynamic Simulation of a Wave-Rotor-Topped Turboshift Engine." Journal of Propulsion and Power 16(5): 792-796.

Guzzella, L., U. Wenger, et al. (2000). IC-Engine Downsizing and Pressure-Wave Supercharging for Fuel Economy, SAE Paper 2000-01-1019.

Gyarmathy, G. (1983). How Does Compresx® Pressure-Wave Supercharger Work, SAE Paper 830234.

Hao, P.-F., F. He, et al. (2005). "Flow Characteristics in a Trapezoidal Silicon Microchannel." Journal of Micromechanics and Microengineering 15: 1362-1368.

Heisler, H. (1995). Advanced Engine Technology. SAE, Warrendale,

Hiereth, H. (1989). Car Tests With a Free-Running Pressure-Wave Charger - A Study for an Advanced Supercharging System, SAE Paper 890 453.

Horrocks, G. D., J. A. Reizes, et al. (1998). Numerical Study of Flow in a Rotating Shock Tube. 13th Australasian Fluid Mechanics Conference, Melbourne, Australia,

Hoxie, S. S., W. E. Lear, et al. (1998). A CFD Study of Wave Rotor Losses Due to the Gradual Opening of Rotor Passage Inlets, AIAA98-3253.

Hunt, S., A. Rudge, et al. (2002). "Micro-Electro-Mechanicals-Systems direct Fluid Shear Stress Sensor Array for Flow Control." Smart Materials and Structures 11: 617-621.

Iancu, F., P. Akbari, et al. (2004). Feasibility Study of Integrating Four-Port Wave Rotors into Ultra-Micro Gas Turbines (U $\mu$ GT). 40th AIAA/ASME/SEA/ASEE Joint Propulsion Conference and Exhibit, Fort Lauderdale, Florida, AIAA2004-3581.

- Iancu, F. and N. Müller (2005). "Efficiency of Shock Wave Compression in a Microchannel." Journal of Microfluidics and Nanofluidics.
- Incropera, F. P. and D. P. DeWitt (1990). Introduction to Heat Transfer. New York, NY, John Wiley & Sons, Inc.
- Jacobson, S. A. (1998). Aerothermal Challenges in the Design of a Microfabricated Gas Turbine Engine. 29<sup>th</sup> AIAA Fluid Dynamics Conference, Albuquerque, NM, AIAA 98-2545.
- Jacobson, S. A., S. Das, et al. (2004). Progress Toward a Microfabricated Gas Turbine Generator for Soldier Portable Power Applications. 24th Army Science Conference, Orlando, FL,
- Jacobson, S. A. and A. H. Epstein (2003). An Informal Survey of Power MEMS. The International Symposium on Micro-Mechanical Engineering, ISMME2003-K18.
- Jenny, E. and T. Bulaty (1973). "Die Druckwellen-Maschine Compresx als Oberstufe einer Gasturbine." Motortechnische Zeitschrift 34(10): 329-335.
- Johnston, D. T. (1987). Further Development of a One-Dimensional Unsteady Euler Code for Wave Rotor Applications, MS Thesis, Naval Postgraduate School, Monterey, CA.
- Johnston, J. P., S. Kang, et al. (2003). Performance of a Micro-scale Radial-Flow Compressor Impeller made of Silicon Nitride. International Gas Turbine Congress, Tokyo, IGTC2003Tokyo OS-110.
- Jonsson, V. K., L. Matthews, et al. (1973). Numerical Solution Procedure for Calculating the Unsteady, One-Dimensional Flow of Compressible Fluid, ASME73-FE-30.
- Kang, S. (2001). Fabrication of Functional Mesoscopic Ceramin Parts for Micro Gas Turbine Engines, Ph.D. Dissertation, Mechanical Engineering, Stanford University, Stanford, CA.
- Kang, S., J. P. Johnston, et al. (2004). "Microscale Radial-Flow Compressor Impeller Made of Silicon Nitride: Manufacturing and Performance." Journal of Engineering for Gas Turbines and Power 126: 358-365.
- Kang, S.-W., Y.-T. Chen, et al. (2002). "The Manufacture and Test of (110) Orientated Silicon Based Micro Heat Exchanger." Tamkang Journal of Science and Engineering 5(3): 129-136.

- Keith (2004). Silicon Carbide Technical Data Sheet. Pico Rivera, CA, Keith Company.
- Kentfield, J. A. C. (1993). Nonsteady, One-Dimensional, Internal, Compressible Flows. Oxford, Oxford University Press.
- Kentfield, J. A. C. (1998). Wave Rotors and Highlights of Their Development, AIAA Paper 98-3248.
- Kharazi, A., P. Akbari, et al. (2004). An Application of Wave Rotor Technology for Performance Enhancement of R718 Refrigeration Cycles, AIAA2004-5636.
- Kharazi, A., P. Akbari, et al. (2004). Performance Benefits of R718 Turbo-Compression Cycles Using a 3-Port Condensing Wave Rotors. 2004 International Mechanical Engineering Conference and Exposition, Anaheim, CA, IMECE2004- 60992.
- Kharazi, A., P. Akbari, et al. (2004). Preliminary Study of a Novel R718 Turbo-Compression Cycle Using a 3-Port Condensing Wave Rotor. 2004 International ASME Turbo Exposition, Austria, GT2004-53622.
- Kim, W. and T.-S. Chair (2002). "A Calculation of the Viscosity of Fluid at the Critical Point." Bulletin of Korean Chemical Society 23(11): 1524-1526.
- Kochevsky, A. N. (2004). "Possibility of Simulation of Fluid Flows Using the Modern CFD Software Tools." Bulletin of Sumy State University.
- Kollbrunner, T. A. (1981). "Comprex Supercharging for Passenger Diesel Car Engines." SAE.
- Kovacs, G. T. A. (1998). Micromachine Transducers Sourcebook.
- Larosiliere, L. M. (1993). Three-Dimensional Numerical Simulation of Gradual Opening in a Wave-Rotor Passage, AIAA93-2526, NASA CR-191157.
- Larosiliere, L. M. (1995). "Wave Rotor Charging Process - Effects of Gradual Opening and Rotation." Journal of Propulsion and Power 11(1): 178-184.
- Larosiliere, L. M. and M. Mawid (1995). "Analysis of Unsteady Wave Processes in a Rotating Channel." International Journal for Numerical Methods in Fluids 21(6): 467-488.
- Lax, P. D. (1954). "Weak Solutions of Nonlinear Hyperbolic Equations and Their Numerical Computation." Communications on Pure and Applied Mathematics VII: 159-193.

- Lear, W. E. and G. Candler (1993). Direct Boundary Value Solution of Wave Rotor Flow Fields, AIAA93-0483.
- Lee, C., S. Arslan, et al. (2004). Design Principles and Aerodynamics of Low Reynolds Number Multi-Stage Microturbomachinery. ASME International Mechanical Engineering Congress & Exposition, Anaheim, CA, ASME, IMECE2004-60703.
- Lin, C.-C., R. Ghodssi, et al. (1999). Fabrication and Characterization of a Micro Turbine/Bearing Rig. IEEE International MEMS'99,
- Liu, L. X., C. J. Teo, et al. (2005). "Hydrostatic gas journal bearings for micro-turbomachinery." Journal of Vibration and Acoustics-Transactions of the Asme 127(2): 157-164.
- Liu, Y., N. K. Truong, et al. (2004). Numerical Studies of Contoured Shock Tube for Murine Powdered Vaccine Delivery System. 15th Australasian Fluid Mechanics Conference, Sydney, Australia,
- Makarious, S. H., H. A. N. Eldin, et al. (1997). Wave-Control Modelling in the Pressure-Wave Supercharger (Comprex). 10th International Conference on Numerical Methods for Laminar and Turbulent Flow, Swansea, UK,
- Makarious, S. H., H. A. N. Eldin, et al. (1995). Inverse Problem Approach for Unsteady Compressible Fluid-Wave Propagation in the Comprex. 9th International Conference on Numerical Methods in Laminar and Turbulent Flow, US,
- Mathur, A. (1985). A Brief Review of the GE Wave Engine Program (1958-1963). ONR/NAVAIR Wave Rotor Research and Technology Workshop, Naval Postgraduate School, Monterey, CA, NPS-67-85-008.
- Mathur, A. (1985). Wave Rotor Research: A Computer Code for Preliminary Design of Wave Diagrams. Monterey, CA., Naval Postgraduate School,.
- Mathur, A. (1986). Code Development for Turbofan Engine Cycle Performance With and Without a Wave Rotor Component. Monterey, CA, Naval Postgraduate School.
- Mathur, A. (1986). Estimation of Turbofan Engine Cycle Performance With and Without a Wave Rotor Component. Monterey, CA, Naval Postgraduate School.
- Mathur, A. and R. P. Shreeve (1987). Calculation of Unsteady Flow Processes in Wave Rotors. AIAA 25th Aerospace Sciences Meeting, Reno, NV, AIAA, AIAA-87-0011.

- Mathur, A., R. P. Shreeve, et al. (1984). Numerical Techniques for Wave Rotor Cycle Analysis. Winter Annual Meeting of the American Society of Mechanical Engineers, US,
- Matsuo, E., H. Yoshiki, et al. (2003). Towards the Development of Finger-Top Gas Turbines. International Gas Turbine Congress, Tokyo, Japan, IGC2003Tokyo OS-103.
- Matsuura, K., C. Kato, et al. (2003). Prototyping of Small-sized Two-dimensional Radial Turbines. International Gas Turbine Congress, Tokyo, Japan, IGTC2003Tokyo OS-107.
- Matthews, L. (1969). An Algorithm for Unsteady Compressible One-Dimensional Fluid Flow, MS Thesis, University of London,
- Mayer, A., J. Oda, et al. (1989). "Extruded Ceramic - A New Technology for the Comprex® Rotor."
- Mehra, A., I. A. Waitz, et al. (1999). Combustion Tests in the 6-Wafer Static Structure of a Micro Gas Turbine Engine. Transducers'99,
- Mehra, A., X. Zhang, et al. (2000). "A Six-Wafer Combustion System for a Silicon Micro Gas Turbine Engine." Journal of Microelectromechanical Systems 9(4): 517-527.
- Meyer, A. (1947). "Recent Development in Gas Turbines." Journal of Mechanical Engineering 69(4): 273-277.
- Miki, N., X. Zhang, et al. (2003). "Multi-Stack Silicon-Direct Wafer Bonding for 3D MEMS Manufacturing." Sensors and Actuators A 103: 194-201.
- Moran, M. J. and H. N. Shapiro (2004). Fundamental of Engineering Thermodynamics, John Wiley & Sons, Inc.
- Moritz, R. (1985). Rolls-Royce Study of Wave Rotors (1965-1970). ONR/NAVAIR Wave Rotor Research and Technology Workshop, Naval Postgraduate School, Monterey, CA, Report NPS-67-85-008.
- Müller, N. and L. G. Fréchette (2002). Performance Analysis of Brayton and Rankine Cycle Microsystems for Portable Power Generation. ASME International Mechanical Engineering Congress & Exposition, New Orleans, Louisiana, IMECE2002-39628.
- Nagasaki, T., R. Tokue, et al. (2003). Conceptual Design of Recuperator for Ultramicro Gas Turbine. International Gas Turbine Congress, Tokyo, Japan, IGTC2003Tokyo OS-102.

- Nalim, M. R. (1995). Preliminary Assessment of Combustion Modes for Internal Combustion Wave Rotors, AIAA 95-2801.
- Nalim, M. R. (1999). "Assessment of Combustion Modes for Internal Combustion Wave Rotors." Journal of Engineering for Gas Turbines and Power 121: 265-271.
- Nalim, M. R. and D. E. Paxson (1997). "A Numerical Investigation of Premixed Combustion in Wave Rotors." Journal of Engineering for Gas Turbines and Power 119(3): 668-675.
- Nalim, M. R. and D. E. Paxson (1997). Numerical Study of Stratified Charge Combustion in Wave Rotors, AIAA 97-3141.
- Nalim, M. R. and D. E. Paxson (1999). Method and Apparatus for Cold-Gas Reinjection in Through-Flow and Reverse-Flow Wave Rotors. US Patent.
- Oberhem, H. and H. A. N. Eldin (1990). Fast and Distributed Algorithm for Simulation and Animation of Pressure Wave Machines. IMACS International Symposium on Mathematical and Intelligent Models in System Simulation, Belgium,
- Oberhem, H. and H. A. N. Eldin (1991). A Variable Grid for Accurate Animation of the Nonstationary Compressible Flow in the Pressure Wave Machine. 7th International Conference on Numerical Methods in Laminar and Turbulent Flow, US,
- Oberhem, H. and H. A. N. Eldin (1995). "Accurate Animation of the Thermo-Fluidic Performance of the Pressure-Wave Machine and its Balanced Material Operation." International Journal of Numerical Methods of Heat and Fluid Flow 5(1): 63-74.
- Okamoto, K. and T. Nagashima (2003). A Simple Numerical Approach of Micro Wave Rotor Gasdynamic Design, ISABE-2003-1213.
- Okamoto, K., T. Nagashima, et al. (2001). Rotor-Wall Clearance Effects upon Wave Rotor Passage Flow. 15th International Symposium on Airbreathing Engines, ISABE-2001-1222.
- Okamoto, K., T. Nagashima, et al. (2003). Introductory Investigations of Micro Wave Rotor. International Gas Turbine Congress, Tokyo, Japan, IGTC 2003Tokyo FR-302.
- Papautsky, I., T. Ameel, et al. (2001). A Review of Laminar Single-Phase Flow in Microchannels. ASME International Mechanical Engineering Congress and Exposition, New York, NY,

- Paxson, D. E. (1992). A General Numerical Model For Wave Rotor Analysis, NASA.
- Paxson, D. E. (1993). A Comparison between Numerically Modelled and Experimentally Measured Loss Mechanism in Wave Rotors. 29th Joint Propulsion Conference and Exhibit, Monterey, CA, AIAA-93-2522.
- Paxson, D. E. (1995). "Comparison between Numerically Modeled and Experimentally Measured Wave-Rotor Loss Mechanisms." Journal of Propulsion and Power 11(5): 908-914.
- Paxson, D. E. (1995). A Numerical Model for Dynamic Wave Rotor Analysis. 31st Joint Propulsion Conference and Exhibit, San Diego, CA, AIAA-95-2800, NASA TM-106997.
- Paxson, D. E. (1996). "Numerical Simulation of Dynamic Wave Rotor Performance." Journal of Propulsion and Power 12(5): 949-957.
- Paxson, D. E. (1997). "Numerical Investigation of the Startup Transient in a Wave Rotor." Journal of Engineering for Gas Turbines and Power-Transactions of the ASME 119(3): 676-682.
- Paxson, D. E. (1998). An Incidence Loss Model for Wave Rotors with Axially Aligned Passages, AIAA98-3251, NASA TM-207923.
- Paxson, D. E. (2001). A Performance Map for the Ideal Air Breathing Pulse Detonation Engine, AIAA 2001-3465.
- Paxson, D. E. and J. W. Lindau (1997). Numerical Assessment of Four-Port Through-Flow Wave Rotor Cycles with Passage Height Variation, AIAA97-3142, NASA TM-107490.
- Paxson, D. E. and M. R. Nalim (1999). "Modified Through-Flow Wave Rotor Cycle with Combustor Bypass Ducts." Journal of Propulsion and Power 15(3): 462-467.
- Paxson, D. E. and J. Wilson (1993). An Improved Numerical Model for Wave Rotor Design and Analysis. 31st Aerospace Sciences Meeting, Reno, NV, AIAA-93-0428, NASA TM-105915.
- Paxson, D. E. and J. Wilson (1995). Recent Improvements to and Validation of the One Dimensional NASA Wave Rotor Model, NASA.
- Peirs, J., D. Reynaers, et al. (2004). "A Microturbine for Electric Power Generation." Sensors and Actuators A 113: 86-93.



- Peirs, J., F. Verplaesten, et al. (2004). A Micro Gas Turbine Unit for Electric Power Generation: Design and Testing of Turbine and Compressor. 9th International Conference on New Actuators, Bremen, Germany, ACTUATOR2004-P115.
- Pekkan, K. and M. R. Nalim (2002). Control of Fuel and Hot-Gas Leakage in a Stratified Internal Combustion Wave Rotor, AIAA-2002-4067.
- Pfeifer, U. and S. Garlich (1990). Gasdynamische Druckwellenmaschine mit Nicht Konstantem Zellenquerschnitt. Germany Patent.
- Piechna, J. (1998). "Comparison of Different Methods of Solution of Euler Equations in Application to Simulation of the Unsteady Processes in Wave Supercharger." The Archive of Mechanical Engineering XLV(2): 87-106.
- Piechna, J. (1998). "Numerical Simulation of the Comprex Type of Supercharger: Comparison of Two Models of Boundary Conditions." The Archive of Mechanical Engineering XLV(3): 233-250.
- Piechna, J. (1998). "Numerical Simulation of the Pressure Wave Supercharger - Effect of Pockets on the Comprex Supercharger Characteristics." The Archive of Mechanical Engineering XLV(4): 305-323.
- Piechna, J. (1999). "A Two-Dimensional Model of the Pressure Wave Supercharger." The Archive of Mechanical Engineering XLVI(4): 331-348.
- Piechna, J. (2003). Autonomous Pressure Wave Compressor Device. 2003 International Gas Turbine Congress, Tokyo, Japan, IGTC03-FR-305.
- Piechna, J. (2005). Wave Machines, Models and Numerical Simulation. Warsaw, Poland, Oficyna Wydawnicza Politechniki Warszawskiej.
- Piechna, J., P. Akbari, et al. (2004). Radial-Flow Wave Rotor Concepts, Unconventional Designs and Applications, Anaheim, CA, ASME, IMECE2004-59022.
- Piechna, J. and P. Lisewski (1998). "Numerical Analysis of Unsteady Two-Dimensional Flow Effects in the Comprex Supercharger." The Archive of Mechanical Engineering XLV(4): 342-351.
- Podhorelsky, L., J. Macek, et al. (2004). Simulation of a Comprex Pressure Exchanger in 1-D Code, SAE 04P-241.
- Radulescu, M. I. and R. K. Hanson (2005). "Effect of Heat Loss on Pulse-Detonation-Engine Flow Fields and Performance." Journal of Propulsion and Power 21(2): 274-285.

- Resler, E. L. J., J. C. Mocsari, et al. (1993). Analytic Methods For Design of Wave Cycles For Wave Rotor Core Engines. AIAA/SAE/ASME/ASEE 29th Joint Propulsion Conference and Exhibit, Monterey, CA, AIAA-93-2523.
- Ribaud, Y. (2003). Internal Heat Mixing and External Heat Losses in an Ultra Micro Turbine. International Gas Turbine Congress, Tokyo, Japan, IGTC2003Tokyo OS-109.
- Roberts, J. W. (1990). Further Calculations of the Performance of Turbofan Engines Incorporating a Wave Rotor, MS Thesis, Naval Postgraduate School, Monterey, CA.
- Rudinger, G. (1969). Nonsteady Duct Flow: Wave Diagram Analysis. New York, NY, Dover.
- Sabersky, R. H., A. J. Acosta, et al. (1998). Fluid Flow: A First Course in Fluid Mechanics. Upper Saddle River, NJ, Prentice-Hall Inc.
- Salacka, T. F. (1985). Review, Implementation and Test of the QAZID Computational Method with a View to Wave Rotor Applications, MS Thesis, Naval Postgraduate School, Monterey, CA.
- Schauer, F., J. Stutrud, et al. (2001). Detonation Initiation Studies and Performance Results for Pulsed Detonation Engine Applications. 39th AIAA Aerospace Sciences Meeting & Exhibit, Reno, NV, AIAA 2001-1129.
- Seippel, C. (1940). Switzerland Patent.
- Seippel, C. (1942). Switzerland Patent.
- Seippel, C. (1946). Pressure Exchanger. US Patent.
- Seippel, C. (1949). Gas Turbine Installation. US Patent.
- Selerowicz, W. and J. Piechna (1999). "Comprex Type Supercharger As a Pressure-Wave Transformer Flow Characteristics." The Archive of Mechanical Engineering XLVI(1): 57-77.
- Shapiro, A. H. (1953). The Dynamics and Thermodynamics of Compressible Fluid Flow. New York, NY, The Ronald Press Company.
- Shimo, M., S. Meyer, et al. (2002). An Experimental and Computational Study of Pulsed Detonations in a Single Tube, AIAA Paper 2002-3716.
- Shreeve, R. P. and A. Mathur (1985). ONR/NAVAIR Wave Rotor Research and Technology Workshop.

- Shreeve, R. P., A. Mathur, et al. (1982). Wave Rotor Technology Status and Research Progress Report. Monterey, CA, Naval Post-Graduate School.
- Spadaccini, C. M., J. Lee, et al. (2002). High Power Density Silicon Combustion Systems for Micro Gas Turbine Engines. ASME TURBO EXPO 2002, Amsterdam, NL, GT-2002-30082.
- Spadaccini, C. M., A. Mehra, et al. (2003). "High Power Density Silicon Combustion Systems for Micro Gas Turbine Engines." Journal of Engineering for Gas Turbines and Power-Transactions of the Asme 125(3): 709-719.
- Spadaccini, C. M., X. Zhang, et al. (2003). "Preliminary Development of a Hydrocarbon-Fueled Catalytic Micro-Combustor." Sensors and Actuators a-Physical 103(1-2): 219-224.
- Stark, B. (1999). "MEMS Reliability Assurance Guidelines for Space Applications." Jet Propulsion Laboratory Publication.
- Stulen, R. Extreme Ultraviolet Lithography (EULV). Albuquerque, NM, Sandia National Laboratories.
- Sun, M., T. Ogawa, et al. (2001). Shock Propagation in Narrow Channels. ISSW23, Fort Worth, TX,
- Sutherland, W. (1893). "The Laws of Molecular Force." Philosophical Magazine 35(214).
- Taussig, R. T. (1984). "Wave Rotor Turbofan Engines for Aircraft." Mechanical Engineering 106(Nov. 1984): 60-66.
- Taussig, R. T. and A. Hertzberg (1984). Wave Rotors for Turbomachinery. Winter Annual Meeting of the ASME, Edited by J. F. Sladky, AD-07.
- Thayer, W. J. (1985). The MSNW Energy Exchanger Research Program. ONR/NAVAIR Wave Rotor Research and Technology Workshop, Naval Postgraduate School, Monterey, CA, NPS-67-85-008.
- Timoshenko, S. (1956). Strength of Materials, Part II - Advanced Theory and Problems. New Jersey, NJ, D. van Nostrand Company, Inc.
- Tuckerman, D. B. and R. F. W. Pease (1981). "High-Performance Heat Sinking for VLSI." IEEE Electron Device Letters EDL-2(5): 126-129.
- Ugural, A. C. and S. K. Fenster (1995). Advanced Strength and Applied Elasticity. New Jersey, NJ, Prentice Hall PTR.

- Waits, C. M., B. Morgan, et al. (2005). "Microfabrication of 3D Silicon MEMS Structures Using Gray-Scale Lithography and Deep Reactive Ion Etching." Sensors and Actuators A 119: 245-253.
- Walther, D. C. and A. P. Pisano (2003). MEMS Rotary Engine Power System: Project Overview and Recent Research Results. 4th International Symposium on MEMS and Nanotechnology, Charlotte, NC, PaperNo.335.
- Weber, F. (2001). Mean Value Modelling of Wave Pressure Supercharger Including Exhaust Gas Recirculation Effects. Zürich, Switzerland, Swiss Federal Institute of Technology.
- Weber, H. E. (1992). "Wave Engine Aerothermodynamic Design." Journal of Engineering for Gas Turbines and Power 114(October): 790-796.
- Weber, H. E. (1995). Shock Wave Engine Design. New York, NY, John Wiley and Sons.
- Welch, G. E. (1993). Two-Dimensional Numerical Study of Wave-Rotor Flow Dynamics, AIAA93-2525.
- Welch, G. E. (1996). Two-Dimensional Computational Model for Wave Rotor Flow Dynamics. International Gas Turbine and Aeroengine Congress & Exhibition, Birmingham, UK, 96-GT-550.
- Welch, G. E. (1997). "Macroscopic Balance Model for Wave Rotors." Journal of Propulsion and Power 12(4): 508-516.
- Welch, G. E. (1997). "Two-Dimensional Computational Model for Wave Rotors Flow Dynamics." Journal of Engineering for Gas Turbines and Power 119(4): 978-985.
- Welch, G. E. (2000). Overview of Wave-Rotor Technology for Gas Turbine Engine Topping Cycles. Novel Aero Propulsion Systems International Symposium, Edited by T. I. o. M. Engineers,
- Welch, G. E. and R. V. Chima (1993). Two-Dimensional CFD Modeling of Wave Rotor Flow Dynamics, NASA.
- Welch, G. E., S. M. Jones, et al. (1997). "Wave Rotor-Enhanced Gas Turbine Engines." Journal of Engineering for Gas Turbines and Power 119(2): 470-477.
- Welch, G. E., D. E. Paxson, et al. (1999). Wave Rotor-Enhanced Gas Turbine Engine Demonstrator, NASA.

- Wilson, J. (1997). Design of NASA Lewis 4-Port Wave Rotor Experiment, AIAA Paper 97-3139, NASA CR-202351.
- Wilson, J. (1997). An Experiment on Losses in a Three Port Wave-Rotor, NASA.
- Wilson, J. (1998). "An Experimental Determination of Losses in a Three-Port Wave Rotor." Journal of Engineering for Gas Turbines and Power 120: 833-842.
- Wilson, J. and D. Fronek (1993). "Initial Results from the NASA-Lewis Wave Rotor Experiment."
- Wilson, J. and D. E. Paxson (1993). Jet Engine Performance Enhancement Through Use of a Wave-Rotor Topping Cycle, NASA.
- Wilson, J. and D. E. Paxson (1996). "Wave Rotor Optimization for Gas Turbine Topping Cycles." Journal of Propulsion and Power 12(4): 778-785.
- Wilson, J. and D. E. Paxson (2002). On the Exit Boundary Condition for One-Dimensional Calculations of Pulse Detonation Engine Performance, NASA.
- www accuratus.com (2005). Accuratus Corporation.
- www.efunda.com (2005). Fundamentals Engineering.
- Ying-Tao, D., Y. Zhao-Hui, et al. (2002). "Gas Flow Characteristics in Straight Silicon Microchannels." Chinese Physics 11(9): 869-875.
- Zauner, E., Y. P. Chyou, et al. (1993). Gas Turbine Topping Stage Based on Energy Exchangers: Process and Performance, ASME 93-GT58.
- Zehnder, G. and A. Mayer (1984). Comprex (R) Pressure-Wave Supercharging for Automotive Diesels - State-of-the-Art. International Congress & Exposition, Detroit, MI, SAE 840132.
- Zehnder, G., A. Mayer, et al. (1989). The Free Running Comprex®, SAE Paper 890452.
- Zhang, X., A. Mehra, et al. (2003). "Igniters and Temperature Sensors for a Micro-Scale Combustion System." Sensors and Actuators a-Physical 103(1-2): 253-262.
- Zhang, X., A. Mehra, et al. (2002). "Development of Polysilicon Igniters and Temperature Sensors for a Micro Gas Turbine Engine." IEEE: 280-283.

